Alma Mater Studiorum - Università di Bologna

SCUOLA DI SCIENZE

Dipartimento di Chimica Industriale "Toso Montanari"

Corso di Laurea Magistrale in

Chimica Industriale

Classe LM-71 - Scienze e Tecnologie della Chimica Industriale

Physisorption of perylene dyes on graphite

Tesi di laurea sperimentale

CANDIDATO

Luca Ferraro

RELATORE

Chiar.mo Prof. Maria Cristina Cassani

CORRELATORE

Dr. Vincenzo Palermo

Dr. Andrea Liscio

Dr.ssa Vanesa Maria Quintano

_____

Anno Accademico 2017-2018
_____

ABSTRACT

This thesis work was carried out at CNR (Council of National Research) of Bologna. CNR- ISOF (Institute of Organic Synthesis and Photoreactivity) in the group of Dr. Vincenzo Palermo.

The aim of this thesis was to perform a comparative and quantitative study on the interaction of three different PDI (perylene diimide) dyes with graphene (G) sheets in solution, using a phenomena called "dye's capturing".

The only difference between the PDI dyes tested was the terminal atom in the side groups. In particular, we used a perylene core with side ethyl-phenyl group exposing in the para position a hydrogen (PDI-H), fluorine (PDI-F), or chlorine atom (PDI-Cl).

Although the relative simplicity of the process and the measurement itself, the preparation of a reliable experimental setup is not trivial and several issues had to be taken into account.

The main challenges to be overcame were related to the effective stability and reliability of the chemical systems, such as dyes, solution and graphite during the entire exposure time.

For this reasons the work addressed the following issues:

- Studying the interaction of small organic molecules and graphite flakes, using commercial products.

- Finding the best conditions for the dye capturing process (concentration, stabilization of the solution, solvent etc.).

- Understanding of the "dye's capturing" phenomena by UV-VIS and fluorescence techniques.

- Stabilizing a relationship between the chemical structure of PDI-X (with side chains symmetrically terminated with a different atom) and the interaction with graphite, taking into account adsorption speed, packing, etc.

- After testing the samples, the reported results were used to: Determinate the best suitable molecule for the dye capturing process and optimize a hypothetical industrial process by calculating the surface area for each molecule.

- Morphology and structural characterizations with different technique like: Atomic force microscopy (AFM), Scanning electron microscopy (SEM), Energy-dispersive X-ray spectroscopy (EDS/EDX), X-ray diffraction (XRD), fluorescence microscopy, Thermogravimetric analysis and differential scanning calorimetry (TGA/DSC), Infrared (IR)
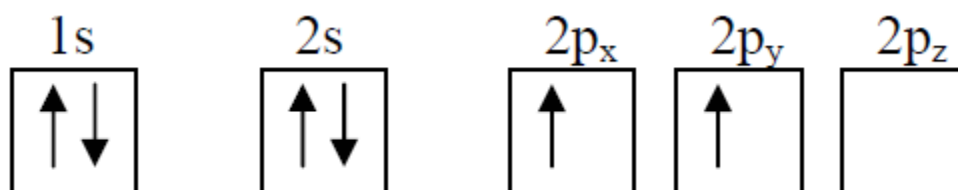
INDEX:

Chapter I - INTRODUCTION

1.0 Carbon materials retrospective

Carbon is one of the most important elements in our life, and it is the fourth most abundant chemical element in nature. Not only constitutes one of the basic elements for life (an average representation of carbon in the mass of living matter is 19.4%); it is also widely used in industry for materials manufacturing. The fundamental feature of carbon is its unique capability for combining with other elements. For example, the so-called hydrocarbons are formed by the grouping of carbon and hydrogen atoms either in chains or in rings. The addition of methyl radicals, nitrogen, oxygen and other new elements provides more complex molecules (acids, alcohols, etc.), whose periodical attachment leads to polymeric structures.

In order to understand why carbon achieves such an elevated coordination degree, we must study its electronic structure. Carbon occupies the 6th position within the periodic table, which provides an electron configuration at ground state of $1s^2\ 2s^2\ 2p^2$. figure 1 shows a scheme of the electron distribution in atomic orbitals, where the arrows indicate the spin polarization.[1]

Figure 1: Electron distribution in the carbon orbitals for a carbon atom with valence number 2. The subindex x, y and z indicate the orientation of p orbitals with respect to the corresponding axis. This differentiation is not required in s orbitals, since they are spherical.

Electronic orbitals of the carbon atom contain only two unpaired electrons, behaving thus as bivalent element. In order to justify the tetravalence of carbon, one of the two electrons from the 2s orbital must occupy an empty 2p orbital. As a result of the previous redistribution, carbon has four dangling bonds and all the electrons in the outer layer are unpaired. Then, the linear combination of s and p atomic orbitals generates the so-called hybrid orbitals. Hybridization comprises three cases: The s orbital together with one p gives rise to two sp orbitals, when two p orbitals are added to s we obtain three sp^2, and finally, the hybridization of all the orbitals from the second layer provides four sp^3. Figure 2 shows the possible geometric configuration in the carbon atom depending of the type of hybridization. Diametrically opposed orientation takes place in the case of sp orbitals. In this configuration, both sp orbitals make strong frontal σ bonds to an adjacent atom, whereas there are two weak lateral π bonds with neighboring p orbitals.

On the other hand, trigonal planar configuration is typical of sp^2, which form σ bonds. The pure p orbital forms a π bond. Finally, sp^3 lobes are oriented towards the vertexes of a regular tetrahedron. In this case, all the four orbitals are hybridized and form σ bonds.
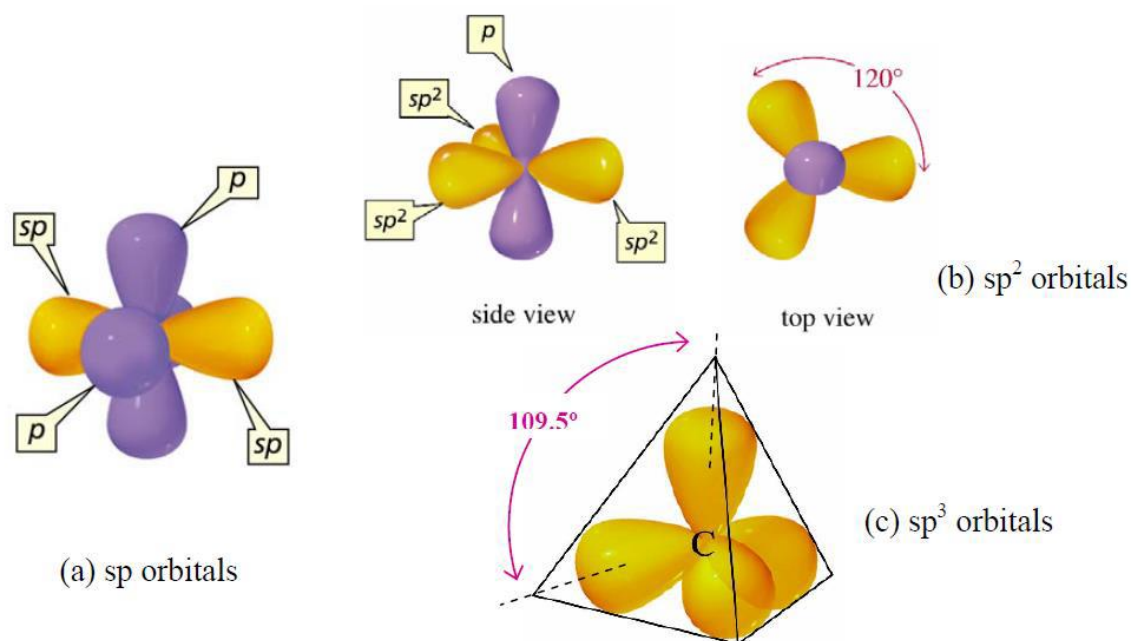
Figure 2: Spatial arrangement of orbitals in the carbon atom in the case of (a) sp, (b) sp2 and (c) sp3 hybridizations. [1]

Carbon presents allotropy, i.e. three main different phases have been found in solid state: graphite, diamond, and amorphous carbon. They are constituted by carbon atoms bonded by sp^2, sp^3 and combinations of both hybridizations, respectively. There exists another configuration of carbon: the polymer-like form. It is found when carbon is diluted with hydrogen, and it presents low hardness, high transparency, and electrically it behaves as an insulator. The spatial distribution of polymeric carbon comprises a rich variety of shapes and lengths, which gives rise to compounds with different chain types. They are divided into aliphatic (lineal, branched, or alicyclic) and aromatic (benzene, etc.) Below, we find summarized some of the most important carbon allotropes.

1.1 Graphite

Graphite shows a stable trigonally bonded crystal structure (figure 3). Carbon atoms become bonded by σ bonds due to three superposed sp^2 orbitals, adding a π bond that results from the interaction of pure p orbitals. This material is soft, optically opaque, chemically active, and is a good electric conductor. The atoms are organized in parallel and single-atom planes, which are called graphene layers and are the center of this thesis. Carbon atoms from adjacent planes are bonded by weak dispersion van der Waals forces, which allow two layers of graphene to slip one on

each other and confers softness and special lubricating properties to graphite. The in-plane bond length is 0.142 nm, whereas the inter-plane distance is 0.335 nm. Graphite crystallizes in hexagonal closepacked (h.c.p.) network, and its most important applications are pencil tips, electrodes, and solid lubricants.[1]

1.2 Diamond

Diamond structure results from the metastable tetragonal σ bonding of carbon atoms, and is only stable at high pressure and high temperature. It is considered to be a material with various extreme physical properties. First of all, it exhibits the highest elasticity module known to date. In fact, diamond establishes the ultimate hardness limit basically due to the superior strength of its chemical bonds. Complete sp^3 hybridization occurs and, therefore, all atoms become bonded via strong frontal σ bonds. The C-C bond (sp^3) is 0.154 nm long, a bit longer and weaker than that in graphite (sp^2), and its crystallographic structure consists of two superimposed face-centered cubic (f.c.c.) lattices shifted by one-quarter of the cube diagonal (figure 1.3). Such bonds confer the extreme hardness of diamond, and the highest atom density among all solids. Diamond is mostly employed in cutting tools (edges), abrasive coatings (dust), and jewelry. A prominent use of diamond in electronic applications has taken place due to the interesting properties when the material is chemically doped, especially in superconductivity applications.[2] Diamond conventional preparation requires high-pressure and high temperature processes (HPHT). Thin films of single crystal diamonds in thin film form are usually prepared by CVD method at high deposition rates. Furthermore, there is also a hexagonal diamond called Lonsdaleite (named in honor of Kathleen Lonsdale). In nature, it forms when meteorites containing graphite strike the Earth. The great heat and stress of the impact transforms the graphite into diamond, but retains graphite's hexagonal crystal lattice. It is theoretically harder (58% more) than conventional diamond but it is not demonstrated in practice, where impurities and lattice defects play a fundamental role.[3]

1.3 Diamond-like carbon (DLC) and amorphous carbon

Besides diamond and graphite, carbon can form an amorphous phase. Amorphous carbon (a-C) is obtained under controlled deposition of the amount of diamond, graphite, and polymeric phases.[4] Its close relationship with DLC is currently defined by the IUPAC as:

- Diamond-like carbon (DLC) films are hard, amorphous films with a significant fraction of sp^3-hybridized carbon atoms and which can contain a significant amount of hydrogen.

Depending on the deposition conditions, these hard films can be fully amorphous or contain diamond crystallites.[5]

- Amorphous carbon is a carbon material without long-range crystalline order. Short range order exists, but with deviations of the interatomic distances and/or interbonding angles with respect to the graphite lattice as well as to the diamond lattice.[6]

The DLC matrix does not contain only one determined hybridization, but contains all three in different proportions. Preparation of a-C containing large sp^3/sp^2 ratio is desirable to obtain "diamond-like" properties. In this way, plasma deposition techniques like sputtering and Plasma Enhanced Chemical Vapor Deposition (PECVD) increase sp^3 bonding, although the latter technique provides H-rich samples. High plasma density PECVD reactors are necessary to maximize sp^3 bonding and simultaneously diminish hydrogen content. When the sp^3 fraction reaches a high degree (80-88%), a-C is denoted as tetrahedral a-C (ta-C) because tetrahedral bonding due to this hybridization is predominant.[7] We can imagine the microstructure as a system of covalently bonded carbon atoms organized in a 3D network, containing a random distribution of sp^2 and sp^3 bonds (figure 1.3). Polymeric carbon can also host a great fraction of sp^3 bonds, although the majority of them come from C-H groups and therefore the material is soft. This ensures a rich variety of a-C microstructures and properties.

1.4 Fullerenes and nanotubes

Although there already were a very well-known variety of carbon based materials (graphite, diamond, and a-C), a more exotic forms of carbon were about to appear. Buckminster fullerenes were introduced in 1980s as an additional form of carbon. They were formulated as C_{60}, and consisted on spherical lattices formed by 60 *sp2*-bonded carbons (figure 1.3). Extensive research on fullerenes has been undertaken for medical applications using fullerenes as substitutive ligands or in biosensor devices. In the early 1990s, even a subset of fullerene science appeared. C_{70}, C_{76}, C_{82}, and C_{84} are other common members of the fullerene family. They are present in soot and produced in nature by lightning discharges in the atmosphere. Even a giant icosahedral molecule C_{540} can be seen within interstellar gas clouds. However, the expectations of these "carbon balls" quickly decreased.[8] Right after, in 1991, Ijima reported the preparation of new cylindrical structures called carbon nanotubes. They were called multiwalled nanotubes (MWCNT), since they consisted on multiple graphene layers that formed a cylinder surface (figure 1.3).[9] Further refinements permitted the deposition of single-wall nanotubes (SWCNT), whose chirality determines their electric properties. Both fullerenes and nanotubes were initially grown by arc discharge and laser

ablation techniques, and recently they have been produced by CVD method. Most carbon nanotubes applications include field emission devices, fuel cells, cold cathodes, and ultrahigh-strength structural materials. Few people in the world had any idea that another, and probably the definitive "son" of the carbon was about to get into the stage:
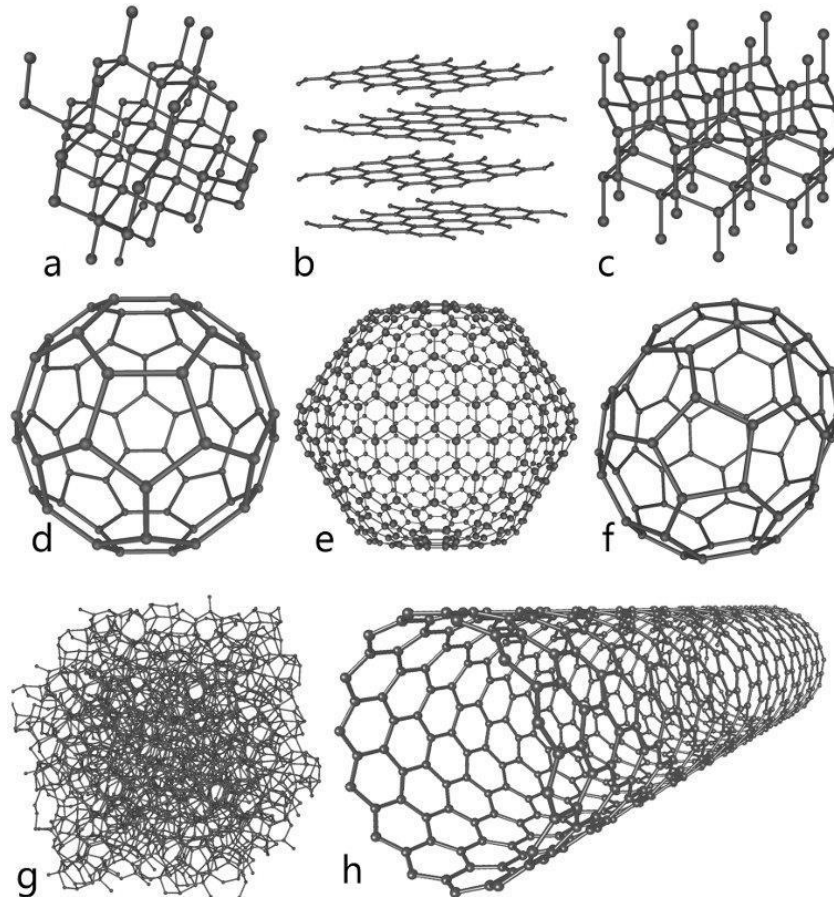
Figure 3:The structures of eight allotropes of carbon: (a) Diamond, (b) Graphite, (c) Lonsdaleite, (d) C60 (Buckminsterfullerene), (e) C_{540} Fullerene, (f) C70 Fullerene, (g) Amorphous carbon, and (h) Single-walled carbon nanotube.[10]

1.5 Graphene and 2D materials

The discovery and research of carbon materials has considerably contributed to the advancement of modern day science and technology. After the discovery of fullerene and single walled carbon nanotube (CNT), which are zero-dimensional and one-dimensional carbon nanomaterials respectively, the researchers have tried to isolate 2D graphitic material or to make 1D nano-ribbons from 2D crystals.

Progress in graphene research had a spillover effect by way of leading to an interest in other 2D materials like for example metal nitrides and carbides. 2D nanostructures are one of the greatest

widely studied materials because of the unique physical singularities that happen when heat transport and charge is confirmed to a plane. Due to the unique properties, 2D nanostructures are anticipated to have an important influence on a huge diversity of applications, extending from high performance sensors, electronics to gas separation or storage, catalysis, inert coatings and support membranes, etc. Right now, the 2D materials family includes not just carbon material but also transition metal dichalcogenides (TMDs), and layered metal oxides. One of the most promising applications of 2D materials is in electronic devices. [11] With respect to the electrical properties, one can fabricate a new generation of superconductors, metallic materials, semimetals, semiconductors, insulators from the 2D materials. Despite the similarity in the chemical formula, MX_2, where typically M is transition metal of groups 4–10 (typically Mo, Nb, W, Ni, V, or Re),[12,13] and X is a chalcogen (typically Se, Te, or S)[14,15]. While the bonding of the tri-layers are covalent, neighboring sheets are bonded via Van der Waals interactions to grow 3D crystals. There are currently 40 different types of combination of TMDs with different chalcogen atoms. Based on the co-ordination and oxidation state of the metal atoms, TMDs ranging from insulators such as HfS_2, semiconductors such as MoS_2, semimetal such as $TiSe_2$, to true metals such as$NbSe_2$, which can even exhibit superconductivity at low temperature.[16,17] Table 1 lists all the current members in the 2D layered materials family.[18] However, stability is a critical issue. The blue shaded materials are constant under ambient environments (room temperature in air) for monolayers. Perhaps green shaded materials are stable in air, but those may be steady only in inert atmosphere are shaded pink. Gray shading means monolayer has been exfoliated, but no further information has yet been provided other than atomic force microscope (AFM). Furthermore, this layered 2D materials exhibits a combination of excellent electronic,[19] mechanical,[20] optical,[21] and thermal properties,[22] which may substitute silicon in electronics, photonics, and nano electromechanical system.

|					
Graphene family	Graphene		*h*BN "white graphene"	BCN	Fluorographene	Graphene oxide
2D chalcogenides	MoS_2, WS_2, $MoSe_2$, WSe_2		Semiconducting dichalcogenides: $MoTe_2$, WTe_2, ZrS_2, $ZrSe_2$, and so on		Metallic dichalcogenides: $NbSe_2$, NbS_2, TaS_2, TiS_2, $NiSe_2$ and so on Layered Semiconductors: GaSe, GaTe, InSe, Bi_2Se_3 and so on
2D oxides	Micas, BSCCO	MoO_3, WO_3	Perovskite–type: $LaNb_2O_7$, $(Ca,Sr)_2Nb_3O_{10}$, $Bi_4Ti_3O_{12}$, $Ca_2Ta_2TiO_{10}$ and so on		Hydroxides: $Ni(OH)_2$, $Eu(OH)_2$ and so on
	Layered Cu oxides	TiO_2, MnO_2, V_2O_5, TaO_3, RuO_2 and so on			others

Table 1:2D materials family[16]

There are many layered materials with strong in-plane chemical bonds and weak coupling between layers. These layered structures provide the opportunity to be cleaved into individual freestanding atomic layers. When the thickness of layered material is reduced to single or only few layers, some extraordinary variations occur in their electronic properties. Due to their symmetry, and high porosity, nanofilms coated with thin layers of inorganic graphene like materials have potential applications from ultralight anti-corrosive materials to electron field emitters. [23,24]

1.5.1: Classification of materials based on dimension

Nanostructured materials (NSMs) are defined as solid materials characterized by at least one dimension in the nanometer range. A crystalline material having at least one dimension smaller than 100 nm is said to be a nanomaterials.

1.5.2 Zero dimensional (0D)

The density of states of quantum-confined nanocrystals has characteristic shapes for different dimension nanomaterials and the differences are due to the degree of confinement of the electrons. For 0D NSMs, the excited electrons are completely confined in all the three dimensions and they behave analogous to atomic/molecular clusters with discreet states that are well separated in energy. Different types of 0D NSMs images are shown in figure 4. Furthermore, 0D quantum dots has been widely considered in solar cells,[25] light emitting diodes (LEDs),[26] lasers,[27] and single-electron transistors.[28]
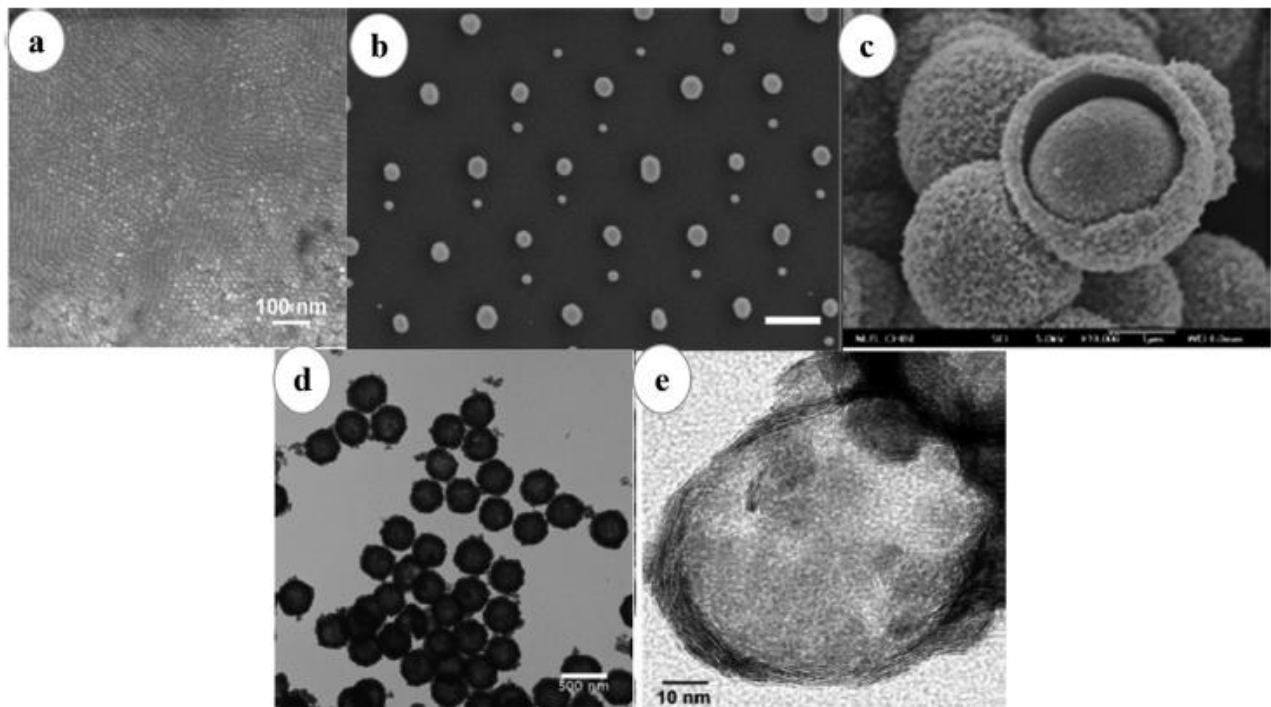
Figure 4: Electron microscope image of various 0D NSMs synthesized by several research groups. (a) Quantum dots,[25] (b) nanoparticles binary arrays, [26] (c) hollow core –shell nanoparticles, [27] (d) hollow sphere, [28] and (e) hollow MoS2 nanospheres.[29] Reprinted by permission of ACS Publishers

1.5.3 One dimensional (1D)

1D nanomaterial has nano-scale sizes along two dimensions and having a rod or wire-like appearance. In such nanomaterials, quantum confinement and surface area related nanoscale effects are more pronounced compared to 2D nanomaterials, while at the same time they can be integrated and/or connected into device architectures due to single bulk-like dimension that is absent in 0D nanomaterials. In the previous decade, interest in 1D materials have increased because of their importance in an extensive range of potential applications such as optoelectronic, and electronic in nanoscale dimensions. Due the differences in quantum mechanical parameter of electron and phonon transport[29], it has been theoretically shown that nanowires of certain alloys can be made to have good electronic conduction with decreased thermal conduction, [30] showing good potential for high performance thermoelectric materials.[31] In figure 5 has been shown some images of various 1D NSMs.
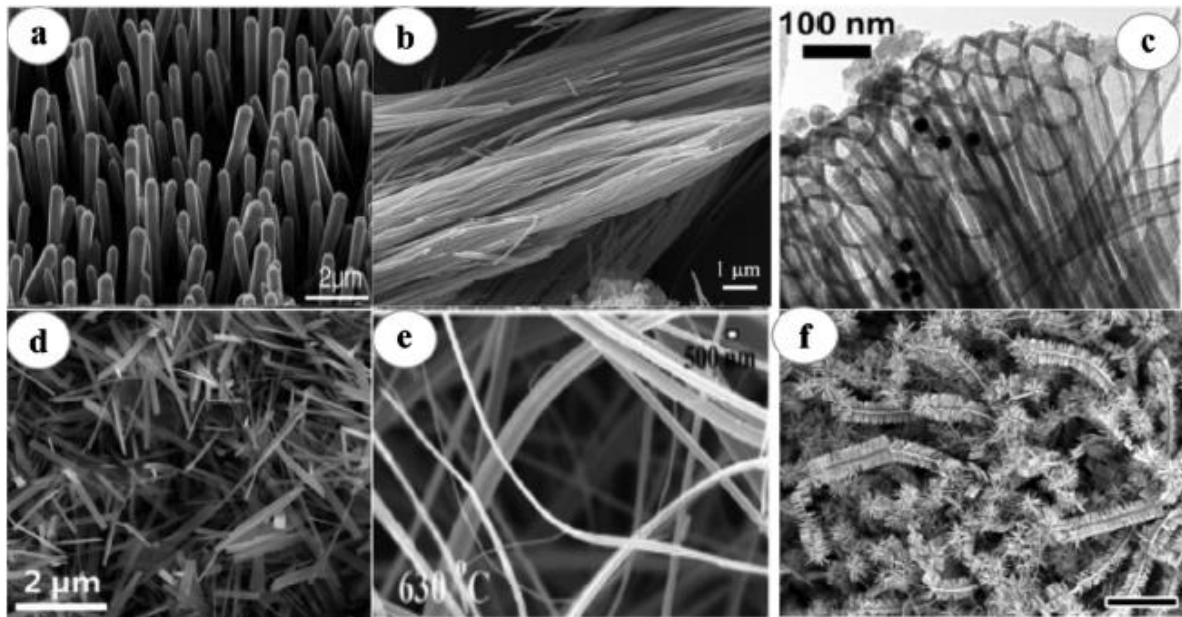
Figure 5: Electron microscope image of various 1D NSMs. (a) Nanowires[29], (b) nanorods[30], (c) nanotubes[31], (d) nanobelts[32], (e) nanoribbons[33], and (f) hierarchrial nanostructures[34]. Reprinted by permission of ACS Publisher

1.5.4 Three dimensional (3D)

3D nanostructures have concerned significant attention in the recent years due to high surface area and physicochemical properties when compared to their bulk materials due to quantum size effects.[30,33] It is long-familiar that the performances of these materials, mainly depend on the shape, size, morphologies, and dimensionality, which are considered to be an important role in their quality execution and applications. Additionally, these well-ordered and innovative 3D NSMs are used in many different applications such as electrode materials for batteries, catalysis, and magnetic material.[31] Then again, 3D NSMs are highly porous materials with 3D could extend to a superior conveyance of the molecules for the catalytic application.

1.5.5 Two dimension (2D)

There are many layered materials with strong in-plane chemical bonds and weak coupling between the layers. These layered structures provide the opportunity to be cleaved into individual freestanding atomic layers. These layers with one dimension strictly restricted to a single layer are called two-dimensional (2D) material. 2D inorganic materials have received great interest recently, because of their particular physical properties due to the quantum size effect, which is related to their nanosized thickness. In addition, at a particular point both the valence band and conduction band touch each other in 2D materials,[35] offering only certain electronic state near the Fermi level thus these materials called zero gap semiconductor or semimetal. The band structure of 2D NSMs is highly sensitive to any change because of their brittleness in single point contact such as mechanical

deformations, external electric fields, doping and adsorbents; which is necessary for sensor applications. This is similarly discussed an ambipolar part onto 2D NSMs, i.e. charge carrier contains either electrons or holes depending on dopant material.[36] However, doping is not continually necessary to alter the charge carrier, local electric fields can also modify the charge carrier sign. This peculiar property of 2D material plays an important role in creating p–n junction transistors with high mobility and this is the base of existing complementary metal oxide semiconductor (CMOS) technology. The 2D material's electronic band structures are equally interesting.

The zero band gap of these materials allows the large range of light absorption in the possible electromagnetic spectrum, extending from the infrared (IR) to the ultraviolet (UV).[37] This opens up a huge number of options of electronic transition resulting in high performance optoelectronic devices and other basic essential studies related to optics and photonics.[38] Simultaneously, a few layers of 2D material present absorbance of less than 10% and in single layered material, it is 2.3%, which may be due to their thickness and transparency.[39] This extraordinary opaque property joined together with their excellent conductivity makes them highly applicable as transparent electrodes in many electronic devices, including solar cell and liquid crystal devices. 2D materials are extremely very strong as graphene ever tested. It gives an extraordinary breaking strength, compare to steel it is 200 times higher and also these materials are unpredictably flexible.

This makes the 2D material a desirable addition to lightweight polymer, and the enforcer of their mechanical properties.

1.6 Synthesis of graphene

1.6.1 Exfoliation

Recently, much attention has turned to the structural and electronic properties of carbonbased materials. At present, especially, graphene is the hottest topics in condensed-matter physics and materials science. This is because graphene has not only unusual properties regarding extreme mechanical strength, thermal conductivity and 2-diemensional films, but also peculiar electronic characteristics such as Dirac-particles with a linear dispersion, transport energy gap and simply absorption coefficient of lights. It is obvious that these excellent properties are relevant at the nanoscale and the manufacture of the conducting nanocomposites is highly dependent on the exfoliation of the graphite down to single graphene sheet in the matrices. However, the challenge remained to achieve complete and homogeneous dispersion of individual graphene sheets in various

solvents.[40] Like CNT and other nanomaterials, the key challenge in synthesis and processing of bulk-quantity graphene sheets is aggregation. Graphene, a one-atom-thick planar sheet of sp^2-bonded carbon atoms densely packed in a honeycomb crystal lattice has very large specific surface area. Unless well separated from each other, graphene tends to form irreversible agglomerates or even restack to form graphite through Van der Waals interactions. The prevention of aggregation is essential for graphene sheets because most of their unique properties are only associated with individual sheets.[40]

There are different synthesis methods lead to "different qualities and characteristics" of the graphene produced. Ones may be close to "perfect", mainly for research purposes but extremely expensive. Others may not be that "perfect" but cheap enough to make it real and carry it to the industry. Among them, Chemical Vapor Deposition (CVD) process (e.g. on copper, nickel, ruthenium…) seems to meet both requirements in quality and cost, as shown in figure 6.
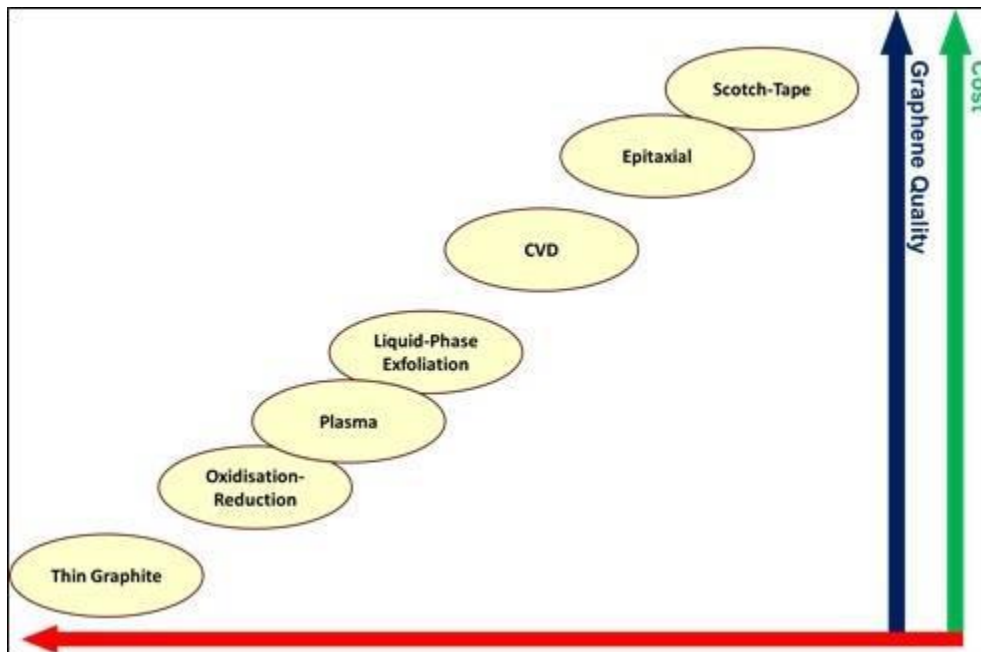
Figure 6: Plot of the main graphene synthesis methods regarding quality and cost (Y-axis) and scalability (X-axis)

1.6.2 Mechanical exfoliation

Also mentioned as micromechanical cleavage, mechanical exfoliation was the first technique used to isolate one monolayer of graphite in 2004. It is possible due to the weak bonds between the atomic planes of graphite. The Van Der Waals interactions between planes are of the order of 2 eV/nm^2. Then, the required normal force to cleave off a 1 μm^2 graphite sheet from the top of the crystallite is about 300 nN, considering 1 μm as path and assuming as unity the graphene-substrate friction coefficient (adhesion is an important friction mechanism at low normal loads).[1] The force

can be exerted using an adapted AFM tip or, more simply, by the resistance to the release of a conventional scotch tape. The last method was the one used to obtain the first isolated graphene sheets based on repeating peeling of highly oriented pyrolytic graphite (HOPG),[1] as seen in figure 7. This process statistically results in some graphene monolayer flakes (among bi, tri and few-layer graphene) which can be transferred to different substrates, usually silicon/silicon dioxide for subsequent characterization purposes.
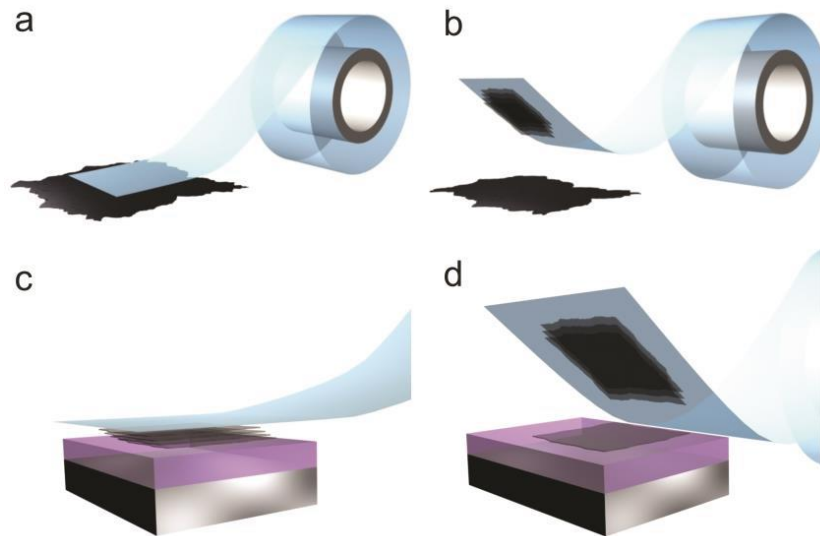

Figure 7: Step by step of a mechanical exfoliation process: (a) adhesive tape is pressed against a HOPG surface so that the top few layers are attached to the tape (b),(c)the tape with crystals of layered material is pressed against a surface of choice , and (d) upon peeling off, the bottom layers is left on the substrate

Nowdays, graphene obtained by mechanical exfoliation is the one which presents the best electronic properties and less crystalline defects, but the difficulties for scaling up the process and to make it compatible with the existent technologies have triggered the investigations to other fabrication techniques. Another drawback of this method is the size of the flakes. In the best of cases, one can obtain flakes of 20x20 μm^2, which can be enough for several fields of research but not suitable for industrial purposes. This method is also useful to obtain monolayers of MoS_2 and h-BN(hexagonal boron nitride).[1]

1.6.3 Chemical exfoliation:

Another possibility is to obtain graphene via wet chemical routes like chemical exfoliation, which consists in the intercalation of a reactant among the graphene sheets (of graphite) that softens the van der Waals interactions. This is achieved immersing graphite in an acid solution (sulfuric and/or nitric acid). The soften interlayer interactions will be broken then, by means of two steps: first, a thermal process (solvothermal), and finally ultra-sonication to disperse them. The result consists in

graphene oxide sheets suspended in a colloidal solution, which are deposited on a substrate (figure 8). For the final objective of obtaining pure graphene flakes, the oxide has to be removed in a reducing atmosphere using alkaline solutions, or applying hydrogen plasma, or hydrazine vapours, figure 8, or through heat treatments. Graphene flakes partially oxidized are obtained because, unfortunately, the reduction processes are not very efficient.[41]
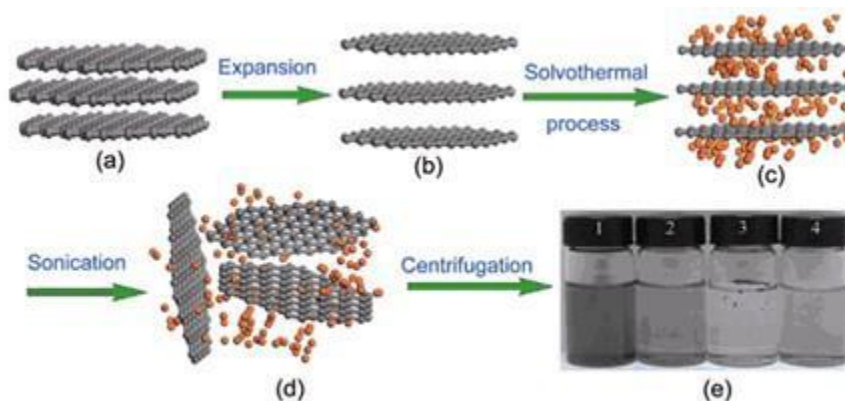

Figure 8: Solvothermal-assisted exfoliation and dispersion of graphene sheets: (a) pristine expandable graphite, (b) expanded graphite, (c) insertion of acid into the interlayers of the expanded graphite, (d) exfoliated graphene sheets dispersed, and (e) optical images of four samples obtain under different conditions.[42]

Another drawback is that in the chemical exfoliation process, the sp^2 like graphene bounds are partially degraded to sp^2-sp^3 structures. Nonetheless, the process involving chemical exfoliation permits an accurate control of the size of the graphene sheets. For example, the longer the sonication process, the smaller the graphene sheets because fragmentation progressively occurs, being possible to obtain solutions with graphene flakes smaller than 10 nm. The graphene size range can be completed with the molecular approach, where the production of polycyclic aromatic molecules (hexabenzocoronene, HBC) reaches the size comparable to the smaller graphene sheets obtained by other approaches, while offering a continuous path to mesoscopic and even macroscopic dimensions.[42] The main advantage of the chemical exfoliation is the high output, which makes it economically competitive and also convenient to manipulate; but due to the chemical steps, the purity and quality is not of a high-performance graphene. Chemical exfoliation is a very popular method used for the production of inks, powder coatings, composite materials, and biological applications.

1.6.4 Epitaxial growth

Producing graphite through ultrahigh vacuum (UHV) annealing of SiC surface has been an attractive approach especially for semiconductor industry because the products are obtained on SiC substrates and requires no transfer before processing devices. When SiC substrate is heated under UHV, silicon atoms sublimate from the substrate. The removal of Si leaves surface carbon atoms to rearrange into graphene layers. The thickness of graphene layers depends on the annealing time and temperature. The formation of ''few-layer graphene'' (FLG) typically requires few minutes annealing of the SiC surface at temperature around 1200 °C. More recently, vapor phase annealing has been used to produce FLG on SiC. At the expense of a higher temperature (typically 400 °C above UHV temperature), this method leads to the formation of FLG on SiC with an improved thickness homogeneity.[43] The similar approach was applied to other metallic substrates to grow graphene layers. The (0001) faces of ruthenium (Ru) crystals were used under UHV to produce epitaxial graphene layers where a very sparse graphene nucleation at high temperatures allowed a linear dimensions growth of macroscopic single-crystalline domains. It was found that the first graphene layer coupled strongly to the Ru substrate, while the second layer was free of the substrate interaction and had the similar electronic structure to free-standing graphene. Other metal substrates including Ir, Ni, Co, and Pt have been employed to produce graphene layers.[44] In figure 9 is shown the epitaxial growth's scheme:
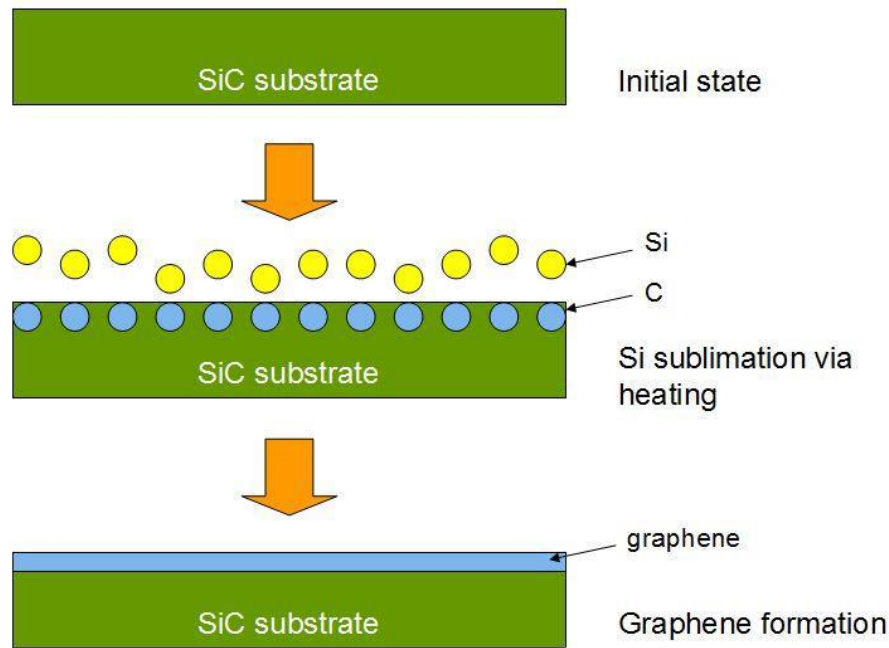
Figure 9: Illustration of an epitaxial growth on a SiC substrate. After the sublimation of silicon, carbon remains on the surface where it would became graphene subsequently[44]

Epitaxial growth is promising because it is easily deployable to the semiconductor industry, transistors, and other electronic devices. On the other hand, the quality of graphene under low-temperature processes still have to be improved in comparison to other technologies like mechanical exfoliation or chemical vapor deposition processes on transition metals. However, the final extension of graphene is only limited by the substrate (SiC wafer) area.

1.6.5 Chemical Vapor Deposition (CVD)

In a CVD process, the graphene growth on a surface is due to thermal decomposition of molecules of a hydrocarbon gas (methane, acetylene, propane...) catalyzed by a metal surface or because of the segregation/precipitation of carbon atoms from the bulk metal.[45] Presently, transition metals are widely used as catalysts in production process of other carbon allotropes like nanotubes. Therefore, it is not surprising that the transition metals (Ru, Ir, Co, Cu, Ni, Re, Pt, Pd) are the main focus of research for the production of graphene. Transition metals are particularly appealing for obtaining large-area high quality graphene and for developing a process ready to be integrated to the existent semiconductor industry.

CVD is a synthesis process in which the chemical constituents react in the vapor phase near or on a heated substrate to form a solid deposit. The number of chemical reactions used in CVD is considerable and include thermal decomposition (pyrolysis), reduction, hydrolysis,

disproportionation, oxidation, carburization, and nitridation. They can be used either singly or in combination.

The growth mechanism of graphene on substrates with mediate-high carbon solubility (> 0.1 atomic %) such as Co and Ni is through the diffusion of the carbon into the metal thin film at the growth temperature and the subsequent precipitation of carbon out of the bulk metal to metal surface upon the cooling.[45] A typical CVD process (i.e. using Ni as a substrate) involves dissolving carbon into the nickel substrate followed by a precipitation of carbon on the substrate by cooling the nickel. The Ni substrate is placed in a CVD chamber at a vacuum of 10^{-3} Torr and temperature below 1000 °C with a diluted hydrocarbon gas. The deposition process starts with the incorporation of a limited quantity of carbon atoms into the Ni substrate at relatively low temperature, similar to the carburization process.

The subsequent rapid quenching of the substrate caused the incorporated carbon atoms to out-diffuse onto the surface of the Ni substrate and form graphene layers. Therefore, the thickness and crystalline ordering of the precipitated carbon (graphene layers) is controlled by the cooling rate and the concentration.

In a CVD process, the graphene growth on a surface is due to thermal decomposition of molecules of a hydrocarbon gas (methane, acetylene, propane...) catalyzed by a metal surface or because of the segregation/precipitation of carbon atoms from the bulk metal.[45] Presently, transition metals are widely used as catalysts in production process of other carbon allotropes like nanotubes. Therefore, it is not surprising that the transition metals (Ru, Ir, Co, Cu, Ni, Re, Pt, Pd) are the main focus of research for the production of graphene. Transition metals are particularly appealing for obtaining large-area high quality graphene and for developing a process ready to be integrated to the existent semiconductor industry.

CVD is a synthesis process in which the chemical constituents react in the vapor phase near or on a heated substrate to form a solid deposit. The number of chemical reactions used in CVD is considerable and include thermal decomposition (pyrolysis), reduction, hydrolysis, disproportionation, oxidation, carburization, and nitridation. They can be used either singly or in combination.

The growth mechanism of graphene on substrates with mediate-high carbon solubility (> 0.1 atomic %) such as Co and Ni is through the diffusion of the carbon into the metal thin film at the growth temperature and the subsequent precipitation of carbon out of the bulk metal to metal surface upon the cooling.[45] A typical CVD process (i.e. using Ni as a substrate) involves dissolving carbon into the nickel substrate followed by a precipitation of carbon on the substrate by cooling the nickel. The Ni substrate is placed in a CVD chamber at a vacuum of 10^{-3} Torr and temperature below 1000 °C

with a diluted hydrocarbon gas. The deposition process starts with the incorporation of a limited quantity of carbon atoms into the Ni substrate at relatively low temperature, similar to the carburization process. The subsequent rapid quenching of the substrate caused the incorporated carbon atoms to out-diffuse onto the surface of the Ni substrate and form graphene layers. Therefore, the thickness and crystalline ordering of the precipitated carbon (graphene layers) is controlled by the cooling rate and the concentration of carbon dissolved in the nickel, which is determined by the type and concentration of the carbonaceous gas in the CVD, and the thickness of the nickel layer.

In contrast, the graphene growth on low carbon solubility (< 0.001 atomic %) substrate like Cu mainly happens on the surface through the four-step process [46]:

1) Catalytic decomposition of methane on Cu to form C_xH_y upon the exposure of Cu to methane and hydrogen. In this process, the Cu surface is either under saturated, saturated, or supersaturated with C_xH_y species, depending on the temperature, methane pressure, methane flow, and hydrogen partial pressure.

2) Formation of nuclei as a result of local supersaturation of C_xH_y where under saturated Cu surface does not form nuclear.

3) Nuclei grow to form graphene islands on Cu surface saturated, or supersaturated with C_xH_y species.

4) Full Cu surface coverage by graphene under certain temperature.

If the amount of available C_xH_y on the exposed Cu surface is insufficient to expand the C to the island edges, the Cu surface is only partially covered with graphene islands. Otherwise, if there is always enough methane to form sufficient C_xH_y to drive the reaction between the C_xH_y at the surface and the edges of graphene islands, graphene islands would grow until to connect neighboring islands and fully cover the Cu surface.

Until recently, most CVD operations were relatively simple and could be readily optimized experimentally by changing the reaction chemistry, the activation method, or the deposition variables until a satisfactory deposit was achieved. However, many of the CVD processes are becoming increasingly complicated with much more exacting requirements, which would make the empirical approach too inconvenient. A theoretical analysis is, in most cases, an essential step which should predict any of the following: chemistry of the reaction (intermediate steps, by-products), reaction mechanism, composition of the deposit (i.e., stoichiometry), and the structure of the deposit (i.e., the geometric arrangement of its atoms). This analysis may then provide a

guideline for an experimental program and considerably reduce its scope and save a great deal of time and effort.[46]

1.6.6 Liquid phase exfoliation (LPE)

Graphite can be successfully exfoliated in liquid environments by exploiting ultrasound to extract individual layers. The liquid-phase exfoliation (LPE) (figure 10) process typically involves three steps: (1) dispersion of graphite in a solvent, (2) exfoliation, and (3) purification.
Graphene flakes can be produced by surfactant free exfoliation of graphite via chemical wet dispersion, followed by ultrasonication in organic solvents. During ultrasonication, shear forces and cavitation, i.e. the growth and collapse of the micrometer-sized bubbles or voids in liquids due to pressure fluctuations, act on the bulk material and induce exfoliation. After exfoliation, the solvent–graphene interaction needs to balance the inter-sheet attractive forces. Solvents ideal to disperse graphene are those that minimize the interfacial tension [mN m^{-1}] between the liquid and graphene flakes, i.e. the force that minimizes the area of the surfaces in contact. In an LPE recipe, solvent is the most important factor dominating the overall productivity of exfoliation.[47] An ideal solvent should be able to effectively overcome the van der Waals interaction between the graphene layers held within a π-π stacking distance of 3.35-3.4 Å. In the presence of a solvent, the potential energy between the adjacent layers given by the dispersive London forces becomes significantly reduced. Coleman et al. proposed that when the refractive index of solvent matches with that of graphene, this potential energy can even approach zero. They demonstrated that solvents with interfacial tension (γ) around ~41 mJ m^{-2} is desired to minimize the energy input in attaining effective separation of sheets beyond the range of the strong van der Waals forces.[48] An approximate expression from a thermodynamic perspective was also provided to account for their experimental results as given below:

$$\frac{H_{mix}}{V_{mix}} = \frac{2}{T_{NS}}\left(\sqrt{E_{SS}} - \sqrt{E_{SG}}\right)^2 \Phi_G$$

where ΔH_{mix} is the enthalpy of mixing, V_{mix} is the volume of the mixture, T_{NS} the thickness of graphene nanosheet, E_{SS} and E_{SG} are the surface energies of solvent and graphene, respectively, ϕ_G is the volume fraction of graphene dispersed. For that reason, solvents belonging to this category, including N-methylpyrrolidone (NMP) (γ =40 mJ m^{-2}), N,N'-dimethylformamide (DMF) (γ=37.1 mJ m^{-2}) and ortho-dichlorobenzene (o-DCB) (γ =37 mJ m^{-2}) have been widely employed for LPE of graphene. Figure 10(a) displays a few commonly utilized solvents for graphene exfoliation along

with their surface tensions as well as boiling points. Among the large variety of solvents explored, the most successful results have been achieved with an organic solvent, NMP This solvent was reported to produce minimal oxidized exfoliated sheets with approximately 28 % monolayer flakes and above 75 % sheets with less than 6 layer thickness. Unfortunately, the yield was low at ~1 wt % and the maximum lateral dimension of graphene was on the order of a few microns (figure 10(b)-(e)). A serial re-sonication/re-centrifugation strategy of the un-exfoliated sediment was recommended to increase the yield.[48]
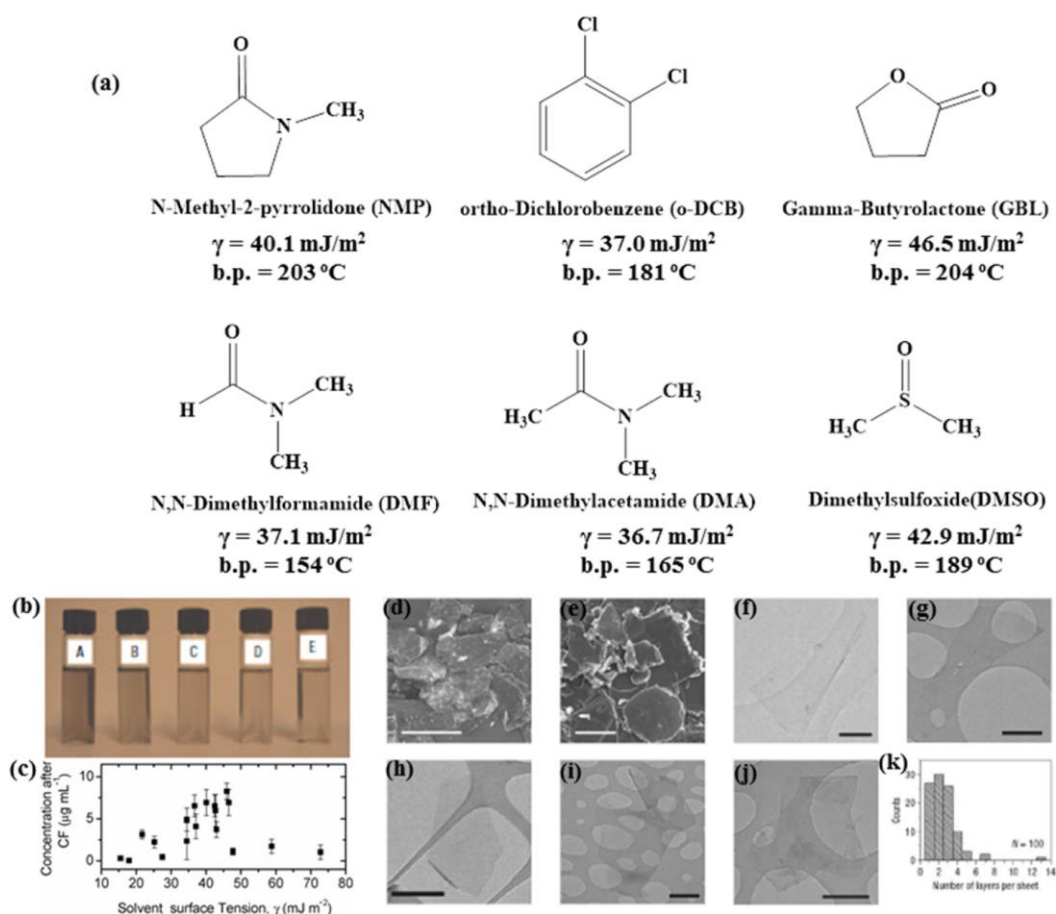
Figure 10: Solvents for LPE of graphene. A) Chemical structures of common organic solvents used in LPE, along with their surface tension and boiling points. b) Graphene dispersion in NMP after centrifugation at 6–4 μg/mL concentrations (a) to (e). c) Dispersed graphene concentration as a function of solvent surface tension/energy. d) SEM imagine of pristine graphite (scale bar: 500 um). e) SEM image of sediment after centrifugation (scale bar: 25 um). (f-h) Bright field TEM images of monolayer graphene sheets respectively from GBL (f), DMEU (g) and NMP (h) (scale bar: 500 nm). (i,j) Bright field TEM images of a folded and multilayer graphene sheets respectively, deposited from NMP (scale bar: 500 nm). k) Histogram of the number of graphene layers per flakes for NMP dispersion. b-k reproduced from [48]

The yield by single-layered graphene (SLG) percentage is defined as the ratio between the number of SLG and the total number of graphitic flakes in the dispersion. The yield by SLG weight is expressed as the ratio between the total mass of dispersed SLG and the total mass of all dispersed flakes. The yield by weight does not give information on the amount of SLG, but only on the total

amount of graphitic material. Yields by SLG percentage and weight are more suitable to quantify the amount of dispersed SLGs.

In order to determine exfoliation yields it is necessary to characterize exfoliated graphitic material providing both qualitative and quantitative information. An ideal graphene characterization is to estimate the concentration c by absorption spectroscopy followed the beer's law: $A=\varepsilon*b*c$.

The number of graphene layers (N), i.e. the thickness of exfoliated graphitic material, is usually determined via transmission electron microscopy (TEM) and atomic force microscopy (AFM).[47]

1.6.7 Liquid phase extraction with organic dye

A natural approach to exfoliate graphene is to use surfactants based on nano-graphenes (NGs), i.e., small polyaromatic hydrocarbons such as pyrenes, perylenes, coronenes, tetracenes, etc. These conjugated moieties exhibit a polyaromatic structure similar, yet smaller, to that of graphene, and are able to self-assemble on its surface forming ordered layers. At least in ultra-high vacuum conditions, these molecules can promote the exfoliation of graphite into graphene, in particular when such a molecule has a high energy of adsorption on the basal plane of graphene, and in particular being higher than the one of the solvent molecule interacting with the graphene. The optical and electronic properties of these NGs can be tuned by functionalizing their peripheries with electron accepting or electron withdrawing groups. The side-groups can also improve their solubility not only in organic solvents but also in water, being the best solvent possible for large scale, environmentally friendly and cheap technological applications. The single or multiple functional moieties attached to the pyrene's periphery include negatively charged sulfonic groups, amines, carboxylic groups.

By using a rather simplistic description of the exfoliation process, organic molecules such as these are often described as aromatic surfactants, "molecular wedges" with the apolar, aromatic part interacting with graphene through π– π stacking and the negatively charged part favoring sheet stabilization in solvents and hindering re-aggregation. The efficiency of amphiphilic pyrenes to interact with graphene has been attributed to their aromatic nature and to their electron donating/withdrawing character due to the difference in the dyes' electronegativity with respect to graphene. The final efficiency of graphite exfoliation with small aromatic dyes ultimately depends not only on the thermodynamics of exfoliation, but also on the presence of local energy minima, which will influence kinetics, and on the solvent– molecule, graphene–molecule and graphene– solvent competitive interactions. To gain a thorough molecular scale understanding on the interaction process between graphene and the dye it is key to perform and compare nano-scale and

multiscale experimental studies. In our laboratory we exfoliate graphene using a series of pyrene molecules functionalized in the peripheral positions with an increasing number of sulfonic groups.[49]
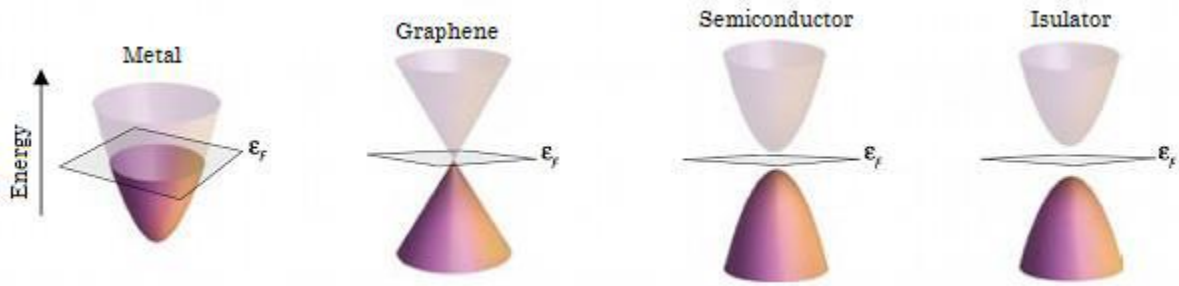
1.7 Graphene properties

From the main characteristics of graphene, several important properties can be derived; and some of them are, in addition, unique and extreme. Two molecular and delocalized π orbitals perpendicular to the σ ones, have the electrons weakly attached and are responsible for the electronic properties of the system. Most of the properties of graphene are then, related to the electronic band structure,[50] plotted in figure 11. The main characteristic of the electronic band occurs at the Fermi energy (EF), where the π orbitals intersect in six points of two different equivalences, named K and K', the so-called Dirac points. The energy dispersion close to the Dirac points is linear with the momentum, being described by $E=\hbar v_F$. The parameter v_F is the Fermi velocity with its value of $v_F \approx c/300$ (where c is the velocity of light in vacuum), and k is the wave vector.
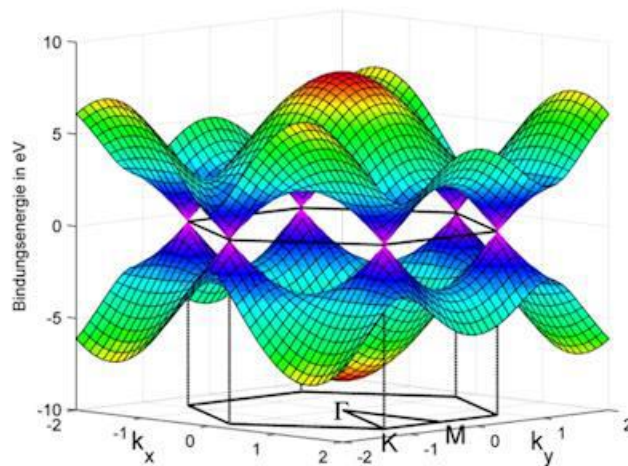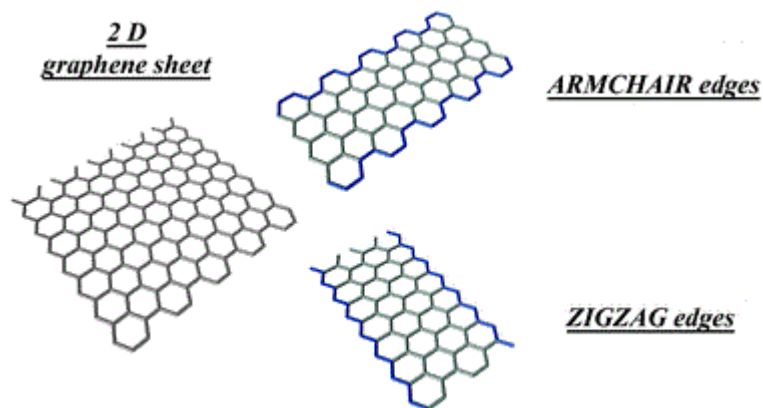

Figure 11:Electronic band structure of graphene. Dirac cones are plotted where the linear relation between k and E [51]

Close to the Dirac points, electrons (and also holes) behave as massless charge carriers with a speed of 106 m/s (faster than any other material) and a carrier charge density in the order of 1013 cm^{-2}. [52] This explains the very high mobilities predicted and detected in graphene and implies that graphene acts as if it was a semiconductor of zero-gap and like a semimetal, a metal with a negligible density of states at the Fermi level (figure 12).

Figure 12: Dirac cones regarding the electronic properties. The cone below is the valence band (electrons), and the above cone is the conduction band (holes)[20]

The electronic band structure of a graphene monolayer, described above, can be modified breaking the symmetry of the crystallographic structure of the graphene sheet.[52] It can be done by stacking more layers, so the energy band in multilayer graphene is different. In addition, as pointed out above, in graphene nanoribbons the band structure depends on the edge geometry and type of termination: armchair or zigzag. (Figure 13)

Figure 13: Armchair and zigzag edges configuration

Coming from its electronic band structure, the most relevant property of graphene is its very high carrier mobility. In graphene, on top of substrates, it is believed that the optical phonon scattering limits the mobility to 120000 cm^2/V*s at room temperature. In suspended graphene, the mobility has been shown to theoretically exceed 200000 cm^2/V*s at Room Temperature (RT), higher than any known semiconductor.[53] Because of the ballistic behavior of graphene, RT Quantum Hall Effect (QHE) and Integer Quantum Hall Effect (IQHE) have been observed in graphene flakes. Interestingly, due to the peculiarities of graphene, we find what is called anomalous QHE, in which the standard sequence of the conductivity with the magnetic field observed in conventional QHE appears shifted in graphene.[54] Another important point about charge transport in graphene is ambipolarity. In the field-effect configuration, this implies that carriers can be tuned continuously

between holes and electrons by supplying the requisite gate bias. Under negative gate bias, the Fermi level drops below the Dirac point, introducing a significant population of holes into the valence band. Under positive gate bias, the Fermi level rises above the Dirac point, promoting a significant population of electrons into the conduction band. The access to a truly ambipolar semiconductor enables a number of novel device structures. These are fundamentally different from silicon-based logic because doping levels can be dynamically controlled entirely by gating. Momentarily providing local gate biases to different parts of the same flake can form junctions or even more complicated logic.[55]

Three molecular and strong σ orbitals in trigonal shape are responsible for maximizing the links among the carbon atoms where the hexagonal structure is built (figure 14). The orbitals also provide this structure a great stability. This fact implies a wide range of mechanical, optical and thermal attributes, which are also relevant.[55] Regarding mechanical properties, graphene presents record values like other allotropes of carbon. Harder than diamond, its tensile strength is about 130 GPa (200 times higher than those of the steel) and the Young modulus has been estimated to be in the range of 0.5-1.0 TPa.

Elastic and super flexible, graphene is even very light, weighing only about 0.77 mg/m^2.[56] Some works also indicated that graphene has promise as a solid lubricant with thickness on the order of nanometers due to its atomically-thin configuration and high load carrying capacity. When tri-layer graphene is benchmarked with a 2 nm repulsive asperity against an 86% sp^3 content diamond-like-carbon (DLC) coating of the same thickness (1.0 nm), the graphene supports up to 8.5 times the normal load of DLC during indentation, and up to twice the normal load of DLC during sliding even after failure of one or more layers. In optics, the main characteristic is the strong light absorption for one monoatomic layer (around 2.3% for visible) but that, in global terms, makes it almost transparent. It can be demonstrated that the absorbance is the result of multiplying πα for the number of graphene layers, where $α=e^2 / \hbar c$ is the fine-structure constant. This linearity has been demonstrated for up to 5 layers,[39] and it is further confirmed that such unique absorption could become saturated when the input optical intensity is above a threshold value, which makes graphene an ideal transparent conductor where optical transparency and low electric resistance are required. Also the thermal properties are relevant. Thermal conductivities in the basal plane of the order of $5*10^3$ Wm^{-1}K^{-1} have been reported, exceeding the record values of diamond and carbon nanotubes. This superb thermal conduction property of graphene is beneficial for electronic applications and establishes graphene as an excellent material for thermal management.
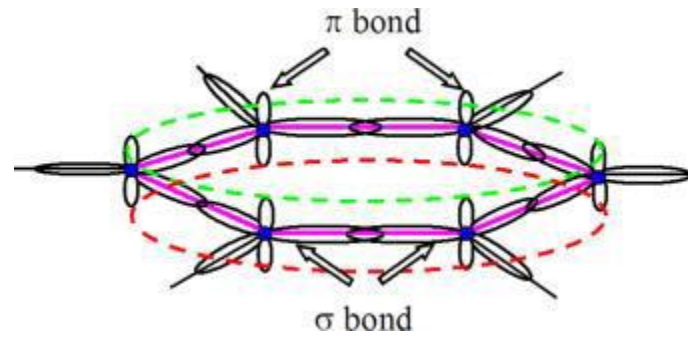
Figure 14: Scheme of the graphene hexagonal structure and σ and π bonds.[39]

As a visual and summarized example of some of the properties, we have the "invisible cat hammocks" of figure 15. It claims that an invisible graphene monolayer of 1 m^2 would only have a weight of 0.77 mg, and tied between two trees could hold a 4 kg body (e.g. a cat).[53]
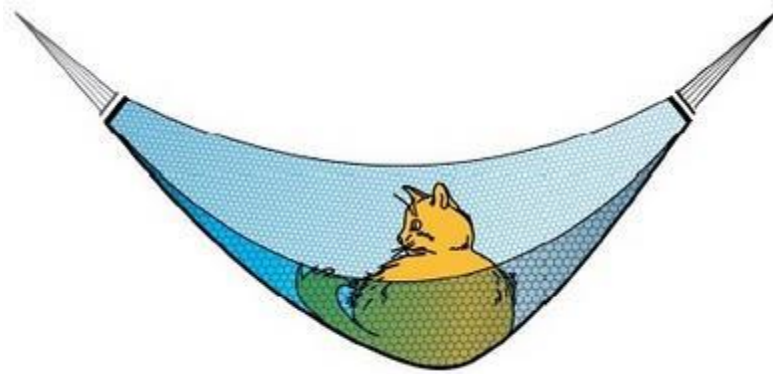

Figure 15: A monolayer graphene hammocks placing a cat before breaking.[53]

1.8 Potential applications

The high mobility of graphene makes this material promising for future electronics. The first and main drawback that we have to tackle is the lack of a band gap. In addition, because of the linear dispersion relation, the density of the states in the Fermi energy level does not allow the non-linear response required in electronic applications. It is necessary to substantially modify the conductance when an electric field is applied. Engineering a band gap in graphene samples may be the solution. As it has been explained above, the electronic band structure of graphene can be modified changing the particular structure that has originated it. One of the methods can be functionalizing the graphene surface with other species. Another way is producing graphene nanoribbons. The finite size effects are present in this kind of structures. Also the edges are important. The type of the nanoribbon edge (zig-zag or arm chair) plays a similar role as the chirality does in carbon nanotubes. Moreover, the spin coherence length is also high in graphene which makes it a suitable

material for applications in spintronics. If the production methods acquire the sophistication that nowadays semiconducting technology demands, graphene is postulated as one of the main candidates to replace silicon in a hypothetical post-Si era.[55]

The high conductivity combined with the low absorbance of graphene warrants properties required for transparent electrodes. Nowadays the standard material for this purpose, indium tin oxide (ITO), can find a competitor in graphene. Once the growth techniques have been developed, graphene can offer a high quality low cost alternative to ITO in applications such as solar cells, liquid crystal displays and touchscreens. New generation of touchscreens would be in principle possible through very high quality and extremely thin and flexible displays. Due to the high thermal conductivity, graphene-based devices would show less degradation in front of heat and, therefore, have longer lifetimes.

Sensing is another possible field of application due to the extraordinary electronic properties, mechanical resistance and large specific surface area of graphene. The adsorption of molecules in the surface can modify the local charge carrier concentration and this can be detected in a Field Effect Transistor (FET) configuration. A single molecule detection has been achieved, which demonstrates the potential high sensitivity of graphene-based sensors.[57] Sensing is not limited only to chemical species; it can be applied to any phenomena that modify the carrier concentration such as magnetic field and mechanical deformation.

Further application fields that, likely, will be a reality in the near future are:

- **Ultracapacitors and microbatteries**: able to store big quantities of energy, 20 times more powerful than the current ones; and with a charging time 1000 times faster.

- **Bio-related material**: Graphene derivatives, including pristine graphene, GO, chemically reduced GO (rGO) and doped graphene have been intensively studied for their widespread applications in biosensing and detection of biomolecules. Many drugs with beneficial therapeutic properties can also present detrimental side effects, limiting their clinical application. The use of nanomaterials to immobilize and deliver these drugs can assist with preventing undesirable effects. Also, complementary studies are exploring strategies to controllably release the immobilized drugs when the appropriate biological target is identified. The ease by which graphene can be chemically modified seemingly lends itself well to such immobilization and delivery applications.

- **Thermal management material**: high thermal conductivity, and consequently fast cooling.

- **Structural materials** (paper, powder): much harder, stronger, and more flexible than current ones.

- **High performance computation**: terahertz oscillators and high-speed field-effect transistors with switching speeds between 100 GHz and a few THz, and a performance 30 times higher than current

- **Junction diodes**: p–n and Schottky diodes are used in a wide variety of electronic/photonic systems as building blocks.

- **Photovoltaics**: more efficient solar cells by using graphene as a charge collector. Electrons in graphene which have been excited to a higher energy state by absorbing incoming light, transfer their energy to neighbouring electrons, rather than radiating it as photons.

- **Conductive ink**: graphene-based coatings for printed electronics (circuits can be printed almost on any substrate) and smart packaging

- **Graphene based quantum dots**: nanolight with extraordinary properties due to their remarkable quantum confinement and edge effects: systematic photoluminescent mechanisms, bandgap engineering, in addition to the potential applications in bioimaging, sensors, etc.

- **Graphene aerogel**: is seven times lighter than air, and 12% lighter than the previous record holder (aerographite). Its density is just 0.16 mg/cm3, and has a superb elasticity and absorption. It can recover completely after more than 90% compression, and absorbs up to 900 times its own weight in oil, at a rate of 68.8 g/s.

- **Optical modulators**: are commonly used in communication and information technology to control intensity, phase, or polarization of light. Graphene allows broadband light-matter interactions with ultrafast responses and can be readily pasted to surfaces of functional structures for photonic and optoelectronic applications.[55]

- **Contaminant removal**: Graphene oxide is non-toxic and biodegradable. Its surface is covered with epoxy, hydroxyl, and carboxyl groups that interact with cations and anions. It is soluble in water and forms stable colloid suspensions in other liquids because it is amphiphilic (able to mix with water or oil). Dispersed in liquids it shows excellent sorption capacities. It can remove copper, cobalt, cadmium, arsenate, and organic solvents. Recently, graphene shown to be able to remove radioactive nuclides, and heavy metals from water, including radioactive isotopes of actinides and lanthanides. Even at concentrations <0.1 g/L, radionuclide sorption proceeds rapidly.

- **Pressure sensor**: The electronic properties of graphene/h-BN (hexagon boron nitride) heterostructures can be modulated by changing the interlayer distances via applying external pressure, leading to potential realization of atomic thin pressure sensors
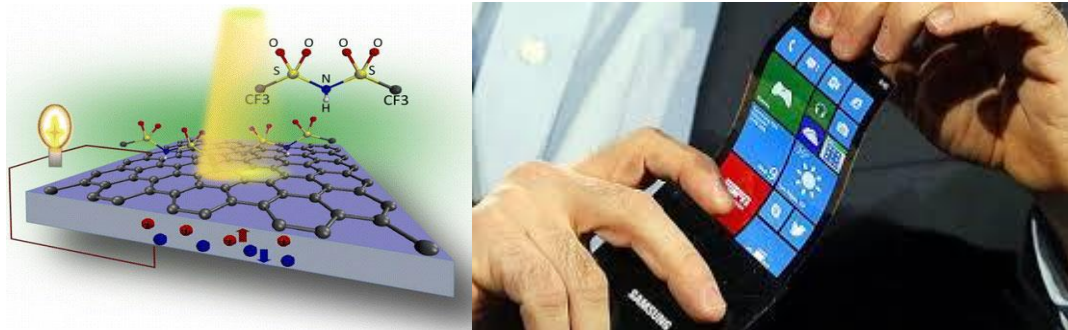

Figure 16: (left) Graphene solar cell; (right) a flexible cell phone made of graphene (Samsung) [58]

1.9 Chemically derived graphene

1.9.1 Graphene oxide(GO)

Nowadays, graphene can be produced by micro-mechanical exfoliation of highly ordered pyrolytic graphite (HOPG), epitaxial growth, and chemical vapor deposition (CVD).These three methods can produce graphene with a relatively perfect structure and excellent properties. However in comparison, graphene produced by reduction of graphene oxide (GO) has some important characteristics as it is produced using graphite material by cost-effective chemical methods in large scale. GO consists of a 1D single-layer of graphite oxide and is usually produced by the chemical treatment of graphite through oxidation. It is also highly hydrophilic and forms stable aqueous colloids to facilitate the assembly of macroscopic structures by simple and cheap solution processes. The well-known methods used for the synthesis of graphite oxide are Brodie method,[59] Hofmann method,[60] and Hummers method,[61] and also their modified and improved forms. In these methods, initially graphite powder is chemically reacted with acids (HCl, H_2SO_4 and HNO_3 etc.) followed by the intercalation of alkali metals (alkali metal compounds $KClO_3$, $KMnO_4$, $NaNO_3$ etc.) into the graphitic layers which further helps in the breaking of graphitic layers into small pieces. In figure 17 as shown summary of different method's
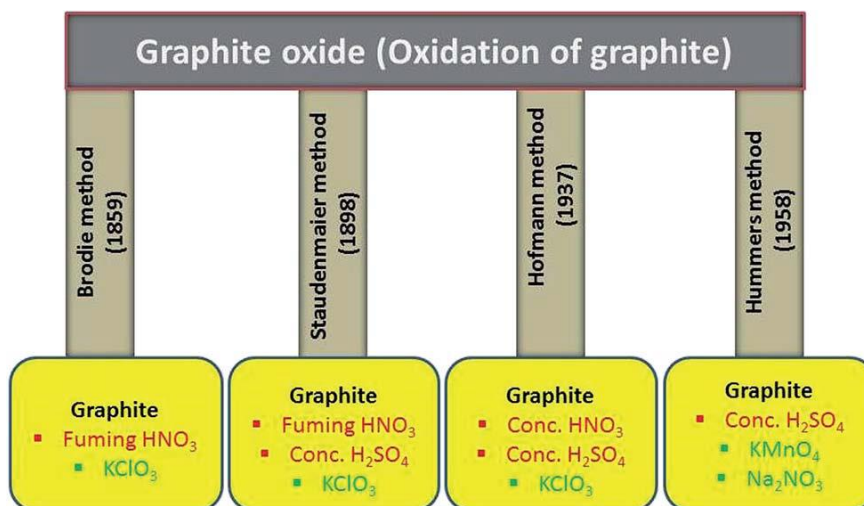
Figure 17: Methods for synthesis of graphite oxide using graphite, acids and oxidizing chemicals [62]

Compared to pristine graphite, GO is heavily oxygenated bearing hydroxyl and epoxy groups on sp^3 hybridized carbon on the basal plane, in addition to carbonyl and carboxyl groups located at the sheet edges on sp^2 hybridized carbon (figure 18). Hence, GO is highly hydrophilic and readily exfoliated in water, yielding stable dispersion consisting mostly of single layered sheets (graphene oxide). It is important to note that although graphite oxide and graphene oxide share similar chemical properties (i.e. surface functional group), their structures are different. Graphene oxide is a monolayer material produced by the exfoliation of GO. Sufficiently dilute colloidal suspension of graphene oxide prepared by sonication are clear, homogeneous and stable indefinitely. Therefore, the formation of stable graphene oxide colloids in water was attributed to not only its hydrophilicity but also the electrostatic repulsion.

Also, the structure of GO depends significantly on the purification procedures, rather than, as is commonly thought, on the type of graphite used or oxidation protocol.[62] The exact identity and distribution of oxide functional groups depend strongly on the extent of oxidation. The appearance of chemical composition inside GO and the oxygen containing functional groups in GO can be identified using principally, X-ray photoelectron spectroscopy (XPS) and Raman spectroscopy.
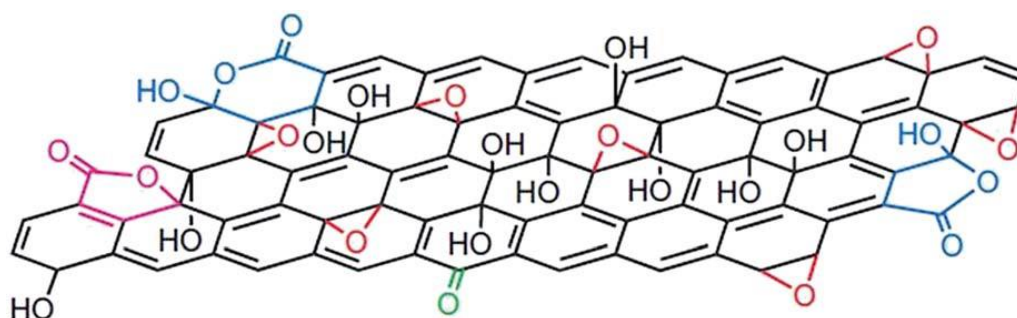

Figure 18: Structure of GO [63]

1.9.2 Reduced graphene oxide (rGO)

Chemical reduction of graphite oxide is one of the excellent procedures to synthesized rGO and graphene in large quantities. It includes ultrasonication of graphite oxide in water forming a homogeneous dispersion of predominantly soluble GO in water. The GO is reduced by a suitable chemical process; the reduced GO formed resembles graphene but contains residual oxygen and other hetero atoms, as well as structural defects. During the reduction processes, most oxygen containing functional groups of GO are eliminated and the π-electron conjugation within the aromatic system of graphite is partially restored. Finally the rGO gets precipitated from the reaction medium because of the recovered graphite domains of chemically converted graphene sheets with increased hydrophobicity and p-stacking interaction.[64] The properties of rGO are nearly similar to that of graphene prepared through different chemical, thermal, photo, electrochemical or microwave reduction pathways.[65] The most widely applied technique used for preparing chemically converted reduced GO is the chemical reduction of GO as shown in figure 19.[66]
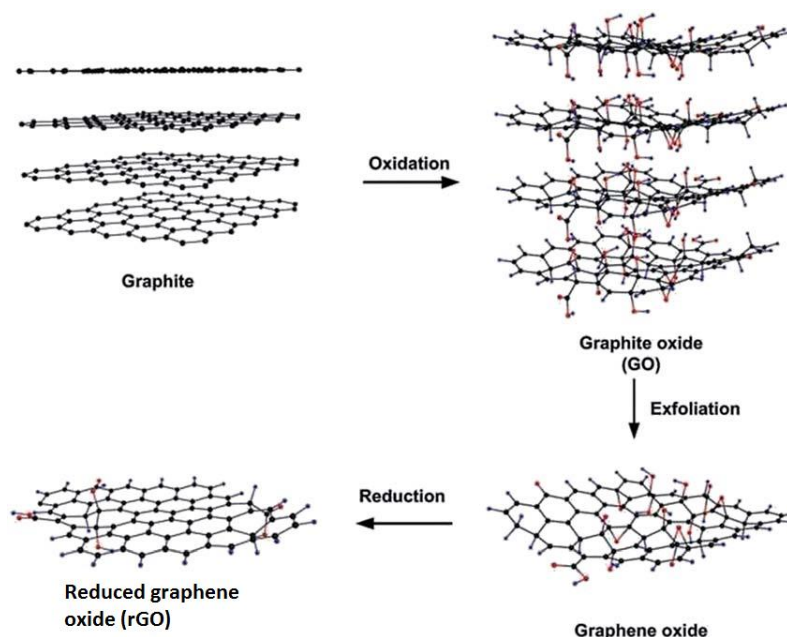

Figure 19: Preparation of rGO by graphite [66]

Fan et al.[67] reported that the exfoliated graphite oxide can undergo quick deoxygenation in strong alkali solutions like NaOH and KOH at moderate temperatures (50–90 °C) resulting in stable aqueous graphene suspensions. Figure 20 shows that the addition of NaOH to the graphite oxide suspension led to the change in color (yellow-brown to dark black). Various inorganic and organic reducing agents such as phenyl hydrazine,[67] hydrazine hydrate,[64] sodium borohydride,[66] ascorbic acid,[68] glucose,[69] etc, have been explored for the chemical reduction of GO.
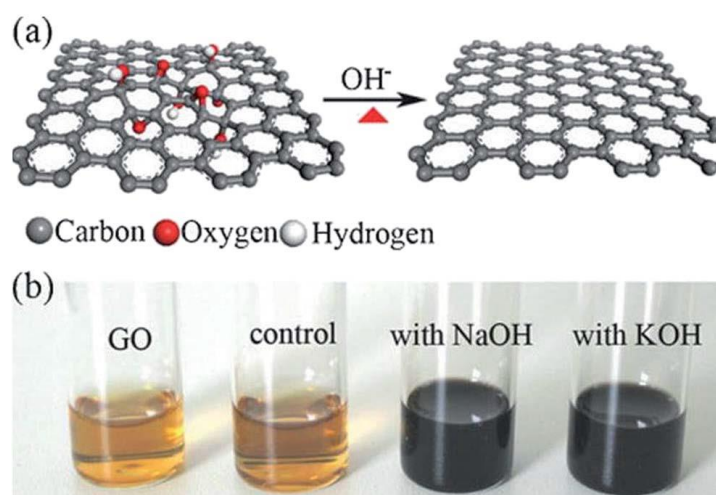
Figure 20: a) Illustration for the deoxygenation of exfoliated graphite oxide under alkaline conditions and (b) images of the exfoliated graphite oxide suspension (≈0.5 mg mL^{-1}) before and after reaction. The control experiment in (b) carried out by heating the pristine exfoliated GO suspension without NaOH and KOH at 90°C for 5 h with aid of sonication [67]

The GO reduced by heating is known as thermal reduction by annealing. Annealing atmosphere is also important for the reduction of GO. Annealing reduction is usually carried out in vacuum, or in inert or reducing atmosphere. Thermal reduction of GO comprised of the thermal-energy-induced multistep removal of intercalated H_2O molecules and oxide groups of carboxyl, hydroxyl, and epoxy. It should be noted that in chemical reduction, individual GO sheets in the solution phase are chemically reduced by the strong chemical base.[70] The rapid heating of graphite oxide at high temperature, exfoliates in the form of porous carbon materials and get converted into graphene with fewer amounts of oxygen functionalities. The exfoliation occurs by the sudden expansion of CO or CO_2 gases evolved from the spaces between graphene sheets during rapid heating of the graphite oxide. The rapid heating makes the oxygen containing functional groups attached on carbon plane to decompose into gases that create huge pressure between the stacked carbon layers.

1.9.3 Electrochemical exfoliation

One of the most efficient ways of exfoliating graphite is by using strong chemical oxidation, yielding highly soluble, 100% monolayer sheets of graphene oxide (GO). A more tunable, versatile, attractive and principally green approach to drive the intercalation and exfoliation of graphite in solution recently explored is the use of electric fields. Upon using bulk graphite as a working electrode in an electrochemical cell, complete dissolution of graphite can be achieved within a few minutes or seconds, either in water or in organic solvents. By regulating the driving potential in appropriate liquid electrolytes, graphite electrodes can be intercalated with various molecules and

dispersed in solution. The most commonly used electrolytes are aqueous solutions of mineral acids (e.g., H_2SO_4 or $HClO_4$) with graphite as an anode. However, applying high electric potential leads to oxidation damage; even if this damage is less extensive than that observed in the "chemical" production of GO (Hummers, etc methods), it is nonetheless relevant. Other less oxidative electrochemical approaches, such as using graphite as a cathode can avoid oxidative damage and give high-quality graphene sheets, but require protracted sonication-assisted treatment.[11] The possibility of intercalating different atoms or molecules between graphene layers offers a highly tunable way to expand graphite into graphene, and to obtain new materials with it. The most efficient processes are based on chemical or electrochemical treatments and involve intercalation, gas production and disruptive fragmentation. In our laboratory, we first used electrochemistry approach to intercalate appropriate molecules into graphite that were able to decompose with temperature. Degradation of these molecules in the graphite-intercalated compound (GIC) was then generated by microwave irradiation and created a gas pressure surge in graphite.

After this microwave-induced expansion, the material was further processed and reduced electrochemically to give highly conductive layers. The use of independent steps for 1) intercalation, 2) expansion, 3) exfoliation and 4) reduction more effective exfoliation of graphene compared with similar approaches, and a better understanding of the chemical processes that lead to expansion/exfoliation (figure 21).
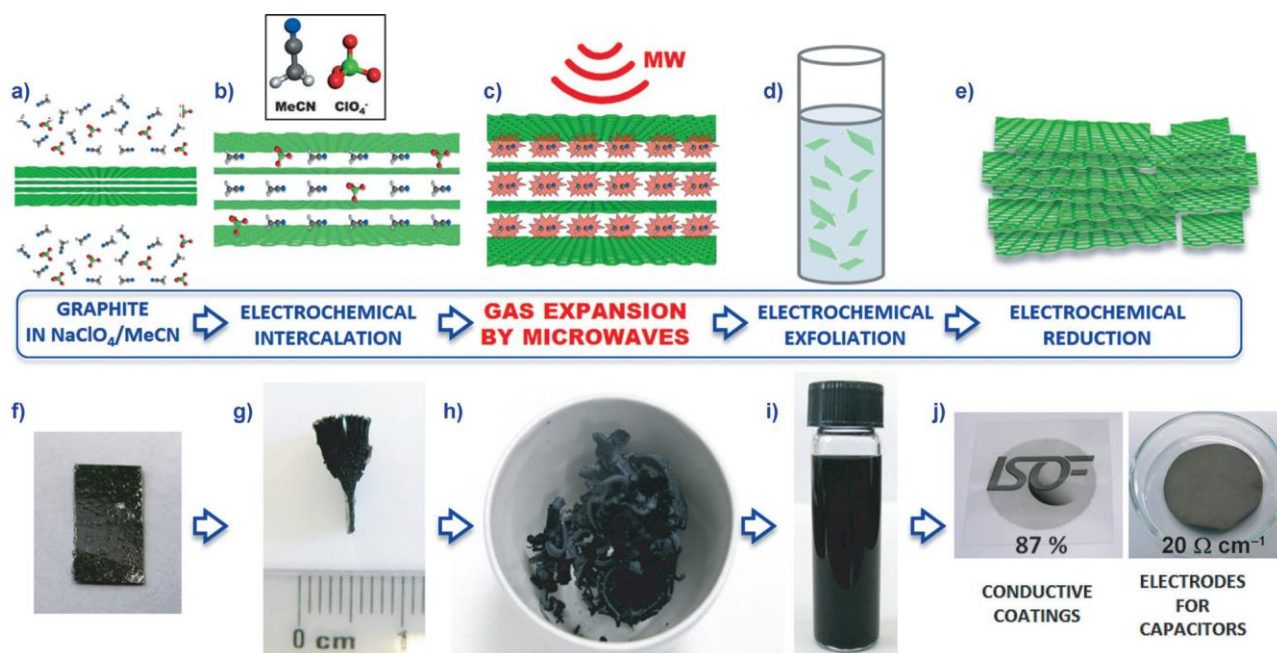

Figure 21: Schematic illustration and photographs of graphite after intercalation, expansion, electrochemical exfoliation and reduction steps (from left to right).[71]

The obtained nano- sheets are mostly highly soluble monolayers that show good electrical properties after electrochemical reduction and can be easily processed into conductive coatings or high-capacitance electrodes on flexible plastic sheets.

1.9.4 Total organic synthesis

Total synthesis of graphene-like polyacyclic hydrocarbons (PAHs), explored decades ago, has caught much attention as a possible alternative route to synthesize graphene. Although PAHs have some advantages including synthesis versatility and the capability of grafting aliphatic chains at the edge to modify solubility, the major challenge lies in preserving dispersibility and a planar geometry for large PAHs. The same group recently reported a bottom-up method to fabricate graphene nanoribbons (GNR) on gold surfaces from 10,10'-dibromo-9,9'-bianthryl precursor monomers. In the fabrication process, thermal deposition of the monomers onto a gold surface removes the halogen substituents from the precursors, and provides the molecular building blocks for the targeted graphene ribbons (with a width of seven benzene molecules) in the form of surface-stabilized biradical species. During a first thermal activation step, the biradical species diffuse across the surface and undergo radical addition reactions to form linear polymer chains as imprinted by the specific chemical functionality pattern of the monomers. In a second thermal activation step, a surface-assisted cyclodehydrogenation establishes an extended fully aromatic system (figure 22).[72]
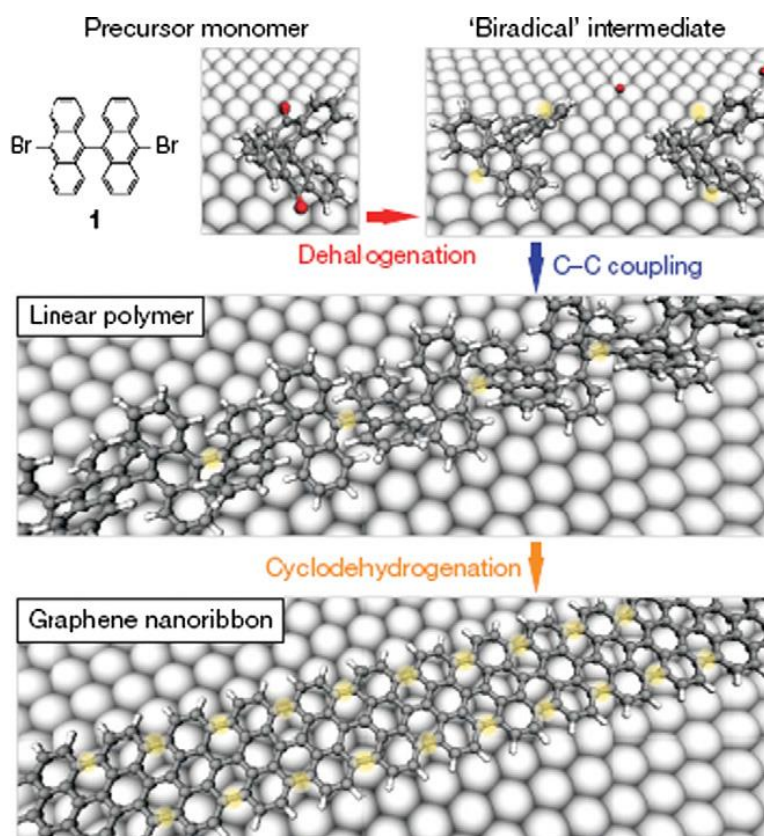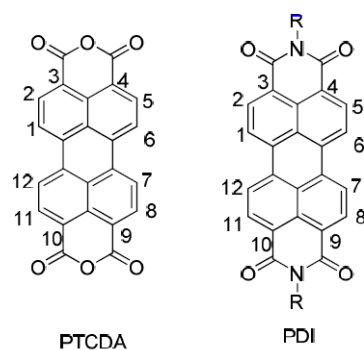
Figure 22: Bottom-up fabrication of atomically precise GNRs. Basic steps for surface-supported GNR synthesis, illustrated with a ball-and-stick model of the example of 10,100-dibromo-9,90-bianthryl monomers (1). Grey, carbon; white, hydrogen; red, halogens; underlying surface atoms shown by large sphere. Top dehalogenation during adsorption of the di-halogen functionalized precursor monomers. Middle, formation of linear polymers by covalent interlinking of the dehalogenated intermediates. Bottom, formation of fully aromatic GNRs by cyclodehydedrogenation [72]

These achievements suggest that total synthesis is a versatile approach to make GNR with precise control of the composition and structure. Studies on the electrical, optical and mechanical properties of these GNR are expected to direct interesting applications.

1.10 Perylene-diimide family

1.10.1 the use of PDI's as pigment in industry

Perylene-3,4,9,10-tetracarboxylic acid diimide derivatives, also known as perylene diimides, or PDIs, are colorants that have been extensively studied as industrial dyes and pigments. Perylene-3,4,9,10- tetracarboxylic dianhydride (PTCDA), which is commonly considered as the parent compound of this class of dye. As shown in figure 23, various perylene diimide dyes with different chemical and physical properties could be obtained via modification of the substituents on the imide (the R groups) or bay (the 1, 6, 7, 12 position on the core aromatic scaffold) positions.

As a group of high performance pigments, perylene diimides exist in a wide range of colors from red to violet, and even shades of black. [73] In addition, these molecules exhibit excellent migration stability in plastics, easy over-coating when used as paints, chemically inert, superior thermal stability, and excellent light and weather stability.[74,75] From an economic point of view, the use of PDI-based pigments is limited, due to the relatively high cost of these materials as pigments.[74] Today, PDI-based pigments are found predominately in fiber applications or in other high-grade industrial paints, where their cost is outweighed by the high quality and/or durability of the colors, particularly in carpet fibers and automobile industry.[75] Yet, while perylene diimides are important industrial pigments, they also combine a strong absorption in the visible region with almost unity fluorescence quantum yields, high photochemical stability, and many other interesting chemical and physical properties.

These properties allow perylene diimides to be used as outstanding materials for many other new applications for example:

- Redox couple : perylene diimides feature a relatively low reduction potential (ca. -1.0 V and -1.2 V vs the ferrocene/ferrocenium ($FeCp_2^{0/+}$)) which enables their use as electron acceptors for organic electronics.
- Optical application and OFETs
- Fluorescent solar collector
- Electrophotographic device
- Dye laser
- Organic photovoltaic cell (OPVs)
- Optical power limiters(OPLs)
- Semiconductor materials

Perylene diimides are still one of the most promising electron-transport materials available to date with a low electron affinity (EA ≈ -3.9 eV for unmodified PDIs, closed to C_{60} and its derivatives),

the potential for good molecular ordering in the solid state, and facile chemical functionalization as compared to fullerene-based acceptors.[75] These features make PDI-type materials promising candidates for applications in n-channel OFETs.[76]

The perylene diimides obtained from the above synthetic approaches by incorporation of different substituents on each imide position usually exhibit indistinguishable absorption and emission properties from the respective symmetrical perylene diimides, particularly in solution at low concentrations when the molecular aggregation is limited. This is because the nodes in the highest occupied molecular orbital (HOMO) and lowest unoccupied molecular orbital (LUMO) at the imide positions of perylene diimides reduce the electronic coupling between PDI aromatic cores and imide substituents to a minimum, as shown in figure 26. It should be noted that the major electronic effect from the imide group will be only inductive in nature. As a result there is little change in the electronic properties of perylene diimides with various imide substituents. It is beneficial to be able to control the solubility as well as the molecular packing in the solid state of the materials by incorporating different side-chains at the PDI imide positions without significantly changing their optical and electronic properties.[75,77]
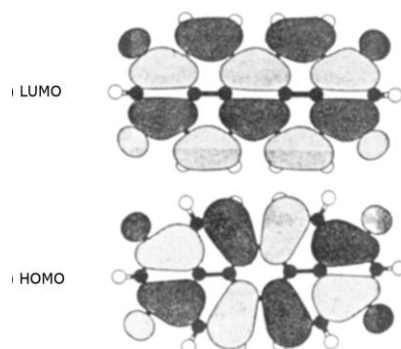
Figure 24: The frontier orbitals (HOMO and LUMO) of perylene diimides

The solubility of PDI derivatives strongly depends on the substituents on the imide positions and/or in the bay positions. The usual explanation for this observation is that the bulky substituents are forced out of the molecular plane of the chromophore, thereby hampering the face-to-face π-π stacking of the PDI molecules, thereby increasing the solubility of these molecules.[75] Similarly, substituents on the aromatic bay-region could lead to a propeller-like twisting of the two naphthalene half units in PDI-based materials. This has also been found to be an efficient way to prevent the face-to-face π-π stacking and improve the solubility of PDI materials. In general, the incorporation of bulky groups on the bay positions could result in an increase of several orders-of-magnitude in the solubility of the perylene diimides.

It is worth noting that halogenated solvents such as chloroform, chlorobenzene, and dichloromethane seem to be good organic solvents for common PDI derivatives at room temperature.[75]

1.10.2 Physical proprieties of PDI's

PDI derivatives exhibit a combination of interesting absorption, emission, redox, and other physical properties, which has results in significant research on these materials for various applications, including OPVs and OFETs.

1.10.3 Optical properties of PDI's

Most PDI-based chromophores are red solids with high melting points and excellent photo- and thermal-stability. In general, perylene diimides are considered as a group of excellent organic dyes with large absorption extinction coefficients at visible wavelengths (400 – 600 nm), almost unity fluorescence quantum yields, and long singlet-excited-state life-times (approximately 4 ns in common organic solvents).[75] Typical perylene diimide type absorption and emission spectra are shown in figure 29, Generally, perylene diimides are characterized by a vibronically structured band with strong absorption in the visible region between 400 to 550 nm, and they exhibit a strong yellow-green fluorescence as a mirror image of the absorption in common organic solvents. It has been reported that the electronic transitions for unsubstituted perylene diimides are predominantly HOMO to LUMO transitions.[75] The absorbance of the (0,0) vibronic transition at ~ 527 nm and the (0,1) vibronic band at ~ 490 nm for free PDI molecules in solution shows the relationship as (0,0)/(0,1) > 1.6, though molecular aggregation of PDI dyes causes a significant decrease in this value.[78] Similar phenomena are also observed in the emission spectra for perylene diimides in solution. Generally, a change of less than 5 nm in the absorption and emission maximum can be observed by changing the N-terminal. In contrast, substituents on the aromatic core bay-positions show a much more obvious effect on the absorption and emission spectra of perylene diimides as expected, due to the stronger electronic coupling between the PDIs π-orbital and the substituents on the aromatic bay region. For example, two phenoxy substituents on the PDIs bay positions result in ~ 20 nm and 40 nm bathochromic shifts in the absorption and emission maximum (λ_{absm} and λ_{emm}), respectively, compared to that of the unsubstituted PDI dyes and the color of the fluorescence changes to orange. More pronounced spectral changes occur upon substitution of the aromatic cores with electron donors such as pyrrolidino groups, which affords PDI derivatives with a dark-

green colour both in the solid state and solution, due to the bathochromic shift over 150 nm. In contrast, limited spectral changes and solvatochromism effect are observed if electron-withdrawing substituents (like F, Cl, Br, and CN) are incorporated into perylene diimides in the bay position because inductive effect of such σ-acceptors in general will lower both the LUMO and HOMO levels in similar manner and there is no obvious ICT (internal charge-transfer) present in these systems.[79] Usually, there are several nanometer red-shifts of the λ_{absm} and λ_{emm} for these compounds because the σ-acceptors stabilized the LUMO slightly more than the HOMO, consequently narrowing the energy gap, probably due to be more pronounced electron coupling between the PDI LUMO to the attached acceptors.
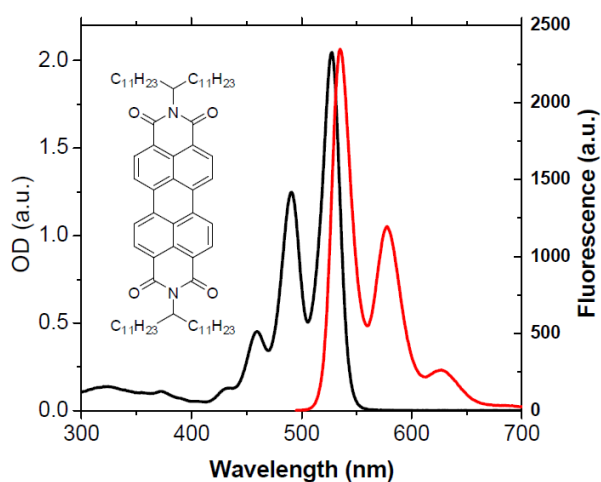
Figure 25: The UV-VID absorption and emission spectra of a perylene diimide in toluene

In addition, optical properties of PDI-based dyes are highly dependent upon concentration and environmental conditions, such as solvent polarity and temperature.[75] For example, aggregation between the aromatic scaffolds in higher concentration ($> 10^{-4}$ mol/L) solutions results in a large bathochromic shift and broader absorption, with a tail absorption that extends into the NIR for PDI derivatives.

The strong aggregation caused by π-π interactions led to an almost complete loss of fine structure in the absorption spectra.[80] For better solvents, such as $CHCl_3$, the dependence of PDIs aggregation on concentration was not as pronounced; no obvious PDI aggregation is observed, as indicated by absorption spectroscopy, with concentrations up to 10^{-5} mol/L for most cases, as shown in figure 30
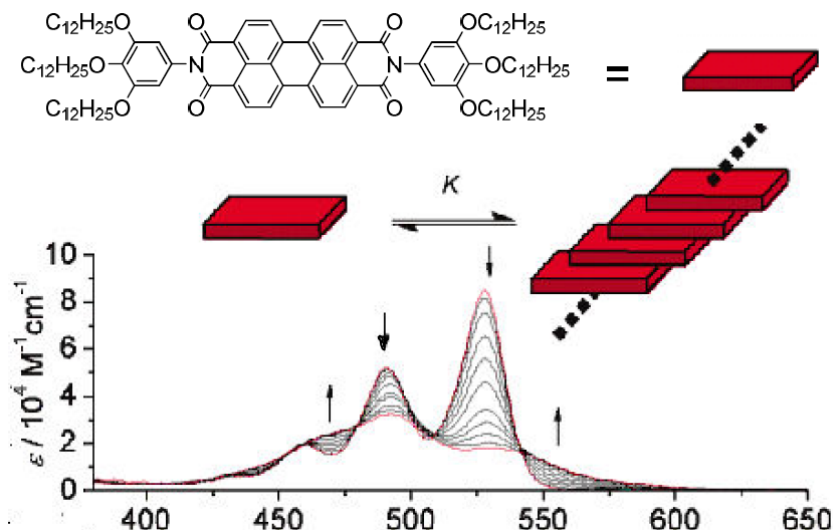
Figure 26: The concentration-dependent UV-Vis absorption of the perylene diimide in methylcyclohexane[80]

Similar observations were found for PDIs emission spectra as a function of increasing concentration. The behavior of a perylene diimide in toluene is shown in figure 31. More aggregate-type emission and decreased fluorescence quantum yields were observed with increasing dye concentration in toluene (concentration range 10^{-6} to 10^{-2} mol/L).[80]
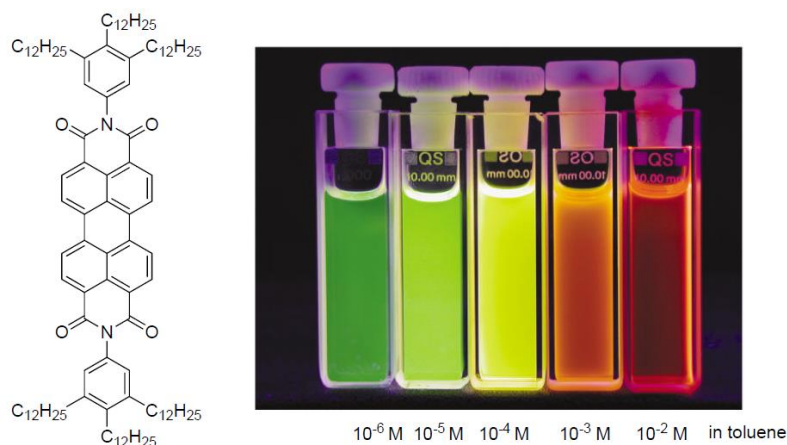

Figure 27: The concentration-dependent emission of the perylene diimide in toluene.[80]

1.10.4 Molecular packing of PDIs in the solid state

Perylene diimide crystal structures often reveal flat π-systems with parallel orientation of the chromophores at an inter-plane distance of ~ 3.4 A (as illustrated in figure 32), which is quite similar to the layer-to-layer distance in graphite.[81] Substituents at the imide position can significantly affect the stacking distance (the longitudinal and transverse offset between the

neighboring perylene diimides in the solid states), which influences the intermolecular interactions of the π- systems in the crystal lattice, results in perylene diimide powders of various colors, from red to dark.[75] On the other hand, substituents at the bay-positions could cause distortion of the flat π-systems due to the steric strain; this is considered an effective way to prevent significant π-π stacking interactions for perylene diimides both in solution or the solid states.
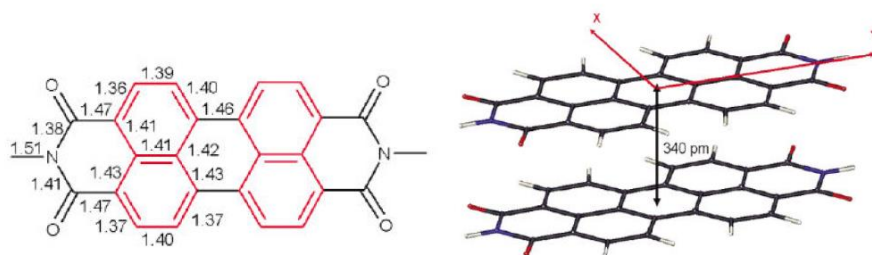

Figure 28: The bond length (left, in Å) and π-π stacking of Pigment Red 179 (right) in crystal [75]

1.10.5 Redox properties of PDI's

Perylene diimides without modification of their core bay-region are good electron acceptors, and they are quite easily reduced and rather difficult oxidized in solution. For most unsubstituted perylene diimides, two reversible reduction waves and one reversible oxidation wave (ca. -1.0 V and -1.2 V vs. $Fe(Cp)_2^{0/+}$, respectively) can be observed if appropriate organic solvents are chosen . Generally, perylene diimides exhibit a first reduction potential comparable to that of C_{60} and its derivatives, which makes them attractive acceptors for replacing fullerene derivatives in photovoltaic applications with their relatively lower cost in comparison to C_{60}-based acceptors, as well as better light harvesting and ease of chemical modification. Some relative small effects on the redox properties of perylene diimides in solution (in general less than 0.100 V on the reduction and oxidation half-wave potential) are observed from variation of the substituents at the imide positions.[75] However, the substituents in the core bay-area have pronounced effects on the redox potentials.[82] For example, perylene diimides with cyano or fluoro substituents in the bay positions are over 0.3 V more easily reduced and have a much higher oxidation potential than unmodified PDI-based compounds.[75] This change in the redox properties is primarily due to the inductive effect from the electron withdrawing groups, which could stabilize the perylene diimides by lowering the energy of both the HOMOs and LUMOs to a similar extent. However, with electron donating pyrrolidino groups at the bay-positions, a quasi-reversible oxidation wave can be observed, and the reduction potential of the material becomes ~ 0.3 V more negative, due to the electron donating effect of the amino moieties. PDI derivatives with conjugated substituents in the bay positions are generally somewhat more readily reduced compared to unsubstituted perylene diimides regardless of whether π-donor or π-acceptor groups are attached. This is probably due to

the extension of conjugation as conjugated substituents are incorporated in their core bay positions.[75]

**1.10.6 Application of PDI dyes in organic electronics (OFETs and OPVs)**

PDI-based materials, with small optical band-gaps (~2.2 eV),[75] low-lying LUMO levels (ca. -3.9 eV),[82] high electron mobilities (> 1 cm^{2}V^{-1}s^{-1}), good molecular ordering in thin films, high molar absorption coefficients (~ 1 × 10^5 M^{-1}cm^{-1}), and facile chemical functionalization at both imide and bay positions, show potential as promising electron-transport materials and/or organic acceptors in organic electronics, especially for OFET and OPV applications[75]:
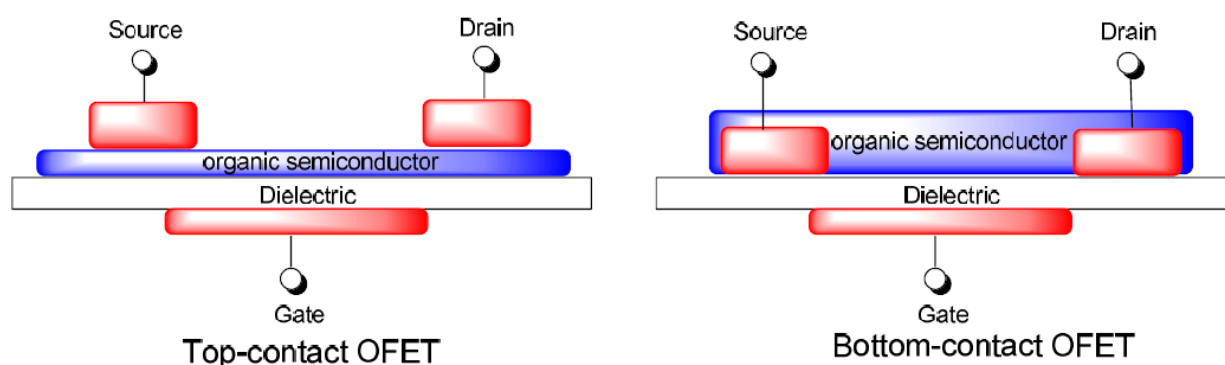
Figure 29: Schematic representations of two widely used OFET geometries: Top-contact OFET (left); bottom-contact OFET (right)

OFETs are a type of thin-film transistors (TFTs) with organic semiconductors as the active layers, analogous to conventional silicon-based metal-oxide-semiconductor thin-film transistors (MOSTFTs). The most commonly used transistor device geometry for an OFET device (as shown in figure 33) is the bottom gate with top contact drain and source electrodes. These generally show higher performance over other device geometries because of their smaller contact resistance compared with bottom-contact MOSTFTs, which can have lower fabrication costs. In the device "off" state, without applied gate bias, there is only limited current flow between the source and drain electrodes in an OFET device when it is operated. In the "on" state, as voltage is applied to the gate electrode, electron or holes can be injected from source/drain electrodes and accumulate at the semiconductor-dielectric interface forming the active channel, which results in increasing source-drain current.[76] Organic semiconductors are, in principle, expected to show ambipolar transport characteristics with both hole and electron conductivities when employed as the active layer in an OFET. In practice, the majority OFETs reported to date show p-type characters. OFETs based on organic materials with low electron affinity (electron affinity defined as the energy change

when an electron is added to the neutral species to form a negative ion), such as perylene diimides and C_{60} derivatives, show electron transport properties. OFETs using electron donors as the active materials, like polythiophenes, typically exhibit hole transport character. Only a limited number of materials can perform both processes simultaneously in OFETs. One of the reasons is the fact that in most organic semiconductors the HOMO-LUMO gap is sufficiently large that, at best, only one of the frontier orbitals (either HOMO or LUMO) is accessible for charge injection from a given electrode material, since charge preference is dependent on the injection barrier from the organic materials to metal electrode, as shown in figure 34 :
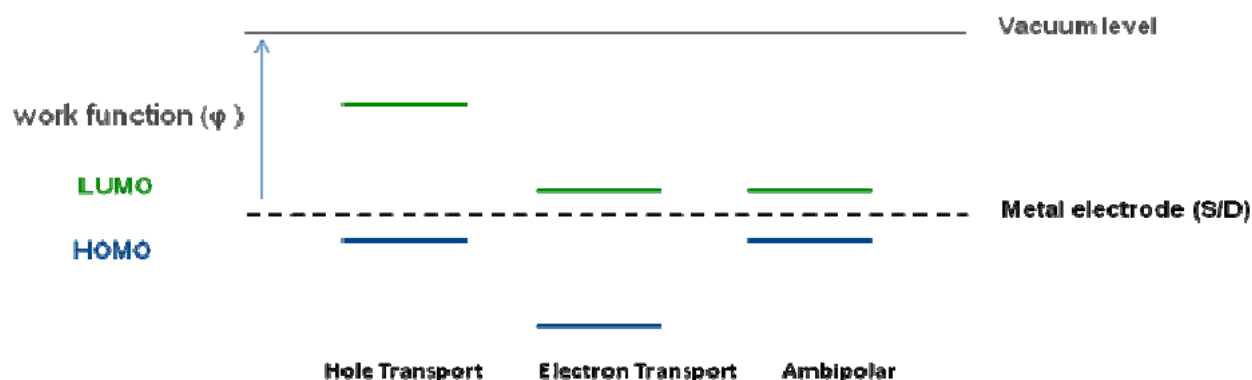
Figure 30: The energy diagram of various charge carrier transport according to a given electrode material. The charge preference is dependent on the injection barrier from the organic materials to the respective metal electrode, and ambipolar material exhibit a relatively small injection barrier from metal electrode for both hole and electron.

Photovoltaic science and technology is related to the processes of converting solar energy directly into electricity. Solar energy is expected to be one of the clean alternative energy sources to fossil fuels in the near future. Organic photovoltaic systems, using organic semiconductors as the active materials, are potentially a cost-effective and lightweight solar energy conversion platform as compared to their inorganic conterparts.[83] In inorganic semiconducting materials, such as silicon, excitons (the coulomb-correlated electron-hole pairs with no net charge) are generally bound weakly (< 0.01 eV), so that ambient thermal energy is sufficient to achieve the charge separation. However, the photo-generated excitons in organic semiconductors are typically strongly coulombically bound, with energies of hundreds of meV, i.e., much greater than thermal energy at ambient temperature, meaning efficient charge separation cannot be achieved in a single organic material. For the organic solar cells using the donor/acceptor heterojunction for charge dissociation, it is believed that a minimum energy difference of > 0.3 eV is required for the LUMO or the HOMO offset between the donor and acceptor materials to overcome such an "exciton-binding" energy for an efficient photovoltaic process in organic D/A interface.[83] Organic solar cells may not compete with silicon-based solar cells in device performance, due to their limitations in light

harvesting ability, charge carrier mobility, as well as the thermal- and photo-stability over silicon. As shown in figure 35, the process of converting solar energy into electricity using OPVs can be schematically described by the following several steps:

- absorption of a photon by the light-harvesting material, which leads to the formation of an exciton (the bound electron/hole pair)

- exciton diffusion from the bulk materials to the D/A interface for charge dissociation

- free charge transport within the active layer to the respective electrodes for charge-carrier collection
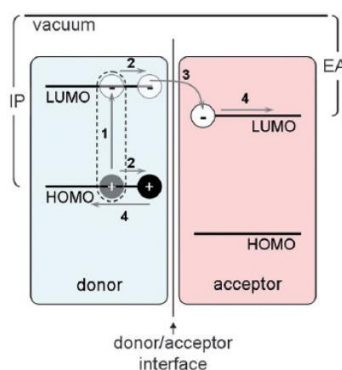
Figure 31: Schematic of frontier molecular orbitals (HOMO and LUMO) at a D/A interface, showing steps in the photovoltaic process. Ionization potential (IP) and electron affinity (EA) are depicted for the donor and acceptor, respectively.[84]

A typical organic solar cell consists of a thin film(s) of organic semiconductor(s) sandwiched between two electrodes. Commonly used architectures of OPV devices are shown in figure 36. There are two major architectures for single-cell-based OPVs: bilayer solar cells (in which donor and acceptor materials are sequentially stacked on top of each other as active layer) and bulk hetero-junction solar cells (BHJs, in which a blend of a donor and an acceptor material is the active layer). Bilayer solar cells are more closely analogous to conventional silicon-based solar cells. These devices benefit from the separated charge carriers transporting layers that ensure transport pathway to the correct electrode for each charge carrier type and give the separated charge carriers limited chance to recombine with their counterparts. However, such blends exhibit significant structural disorder, relying on random phase separation of the components. In most cases, these molecular domains are too large (cause excitonic loss) or too small (leading to facile charge recombination) in size, that causing a devise performance decreases.[84]
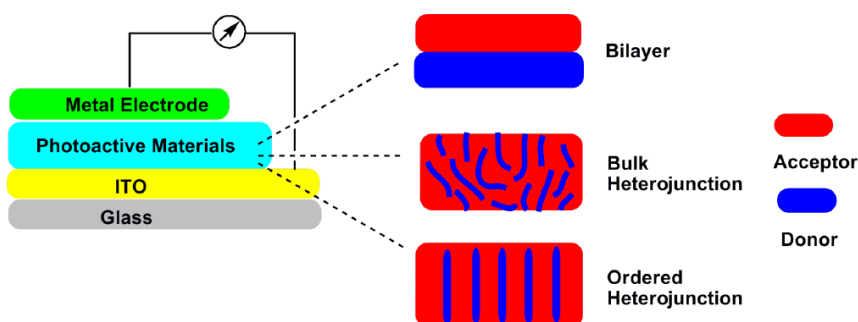
Figure 32:Schematic illustration of an OPV device: bilayer solar cell (top), BHJ solar cell (middle), and ordered heterojunction cells (bottom)

Currently, power conversion efficiencies (PCEs) of organic solar cells have so far been limited to approximately 8% with the Solarmer polymer blends in small area device (< 0.1 cm^2), while PCEs have been demonstrated to exceed 20% for Si-based solar cells, 15% for thin film inorganic cells, and 11% for dye-sensitized solar cells. However, further research attention on OPVs could potentially leads to increased PCEs comparable to other photovoltaic technologies.[85]

Recent research found that liquid crystals possess the ability to self-organize spontaneously into highly ordered structures. Due to the spontaneous ordering of the molecules in the liquid crystalline phase, very highly ordered films can be obtained after the liquid crystalline film is cooled to a crystalline phase. Therefore, the use of liquid crystalline perylene derivatives in organic p-n junctions is a promising method to increase the efficiency of such a solar cell.[86] While from an economic perspective, the cost/watt is a critical metric for evaluating competing energy generating technologies, from a scientific perspective, the device power conversion efficiency, is the most important characteristic when evaluating an organic solar cell.

REFERENCE:

1.   C. Corbella Roca. Thin Film Structures of Diamond-Like Carbon Prepared By Pulsed Plasma Techniques. *Thesis in Universitat de Barcelona. Departament de Física Aplicada i Òptica* (2006).

2.   May, P. W. Diamond thin films: a 21st-century material. *Philosophical Transactions of the Royal Society A: Mathematical, Physical and Engineering Sciences* **358,** 473–495 (2000).

3.   Xu, Y., Li, Z. & Duan, W. Thermal and Thermoelectric Properties of Graphene. 1–19 (2014). doi:10.1002/smll.201303701

4.   Robertson, J. Diamond-like amorphous carbon. *Materials Science and Engineering: R: Reports* **37,** 129–281 (2002).

5.   Mansour, A. Structural Analysis of Planar sp 3 and sp 2 Films : Diamond- Like Carbon and Graphene Overlayers Thesis by. *Thesis* (2011).

6.   Bewilogua, K. & Hofmann, D. History of diamond-like carbon films - From first experiments to worldwide applications. *Surface and Coatings Technology* **242,** 214–225 (2014).

7.   Of, N., Faculty, R., Engineering, E., Gajdo, L. & Vesel, M. Applicability of Diamond and Diamond-like Carbon Thin Films as Biomaterials. (2011).

8.   Kroto, H. W., Heath, J. R., O'Brien, S. C., Curl, R. F. & Smalley, R. E. C 60: buckminsterfullerene. *Nature* **318,** 162–163 (1985).

9.   Iijima, S. Helical microtubules of graphitic carbon. *Nature* **354,** 56–58 (1991).

10.   Https://www.boundless.com/chemistry/textbooks/boundless-chemistry-textbook/nonmetallic-elements-21/carbon-150/allotropes-of-carbon-582-3569/. [10] Https://www.boundless.com/chemistry/textbooks/boundless-chemistry-textbook/nonmetallic-elements-21/carbon-150/allotropes-of-carbon-582-3569/.

11.   Wang, Q. H., Kalantar-zadeh, K., Kis, A., Coleman, J. N. & Strano, M. S. Electronics and optoelectronics of two-dimensional transition metal dichalcogenides. *Nature Publishing Group* **7,** 699–712 (2012).

12.   Mak, K. F., Lee, C., Hone, J., Shan, J. & Heinz, T. F. Atomically Thin MoS 2 : A New Direct-Gap Semiconductor. *PHYSICAL REVIEW LETTERS* **136805,** 2–5 (2010).

13.   Canadell, E., Moulay, J. & El, A. Origin of Metal Clustering in Transition-Metal Chalcogenide Layers MX2 (M = Nb, Ta, Mo, Re; X =. *J. AM. CHEM. SOC.* 3778–3782 (1989).

14.   Lukowski, M. A. *et al.* Highly active hydrogen evolution catalysis from metallic WS $_2$

nanosheets. *Energy & Environmental Science* **7,** 2608 (2014).

15. He, J., Hummer, K. & Franchini, C. Stacking effects on the electronic and optical properties of bilayer transition metal dichalcogenides. *Physical Review B* **89,** 75409 (2014).

16. Huang, Y. H., Peng, C. C., Chen, R. S., Huang, Y. S. & Ho, C. H. Transport properties in semiconducting NbS 2 nanoflakes. *APPLIED PHYSICS LETTERS* **93106,** (2016).

17. Sohee Jeong, Dongwon Yoo, Jung-tak Jang, Minkyoung Kim, and J. C. Well-De fi ned Colloidal 2‐D Layered Transition-Metal Chalcogenide Nanocrystals via Generalized Synthetic Protocols. *J. AM. CHEM. SOC.* 1–4 (2012).

18. Geim, a K. & Grigorieva, I. V. Van der Waals heterostructures. *Nature* **499,** 419–25 (2013).

19. Goki Eda,,r Takeshi Fujita, Hisato Yamaguchi, Damien Voiry, Mingwei Chen, and M. C. Coherent Atomic and Electronic Heterostructures of Single-Layer MoS2. *American Chemical Society* 7311–7317 (2012).

20. Li, H. *et al.* Mechanical Exfoliation and Characterization of Single- and Few-Layer Nanosheets of WSe 2 , TaS 2 , and TaSe 2. *Small* 1974–1981 (2013). doi:10.1002/smll.201202919

21. Hai Li, Gang Lu, Zongyou Yin, Qiyuan He, Hong Li, Qing Zhang, and H. Z. Optical Identification of Single- and Few-Layer MoS2 sheets. *communications* 682–686 (2012). doi:10.1002/smll.201101958

22. Tongay, S. *et al.* Thermally Driven Crossover from Indirect toward Direct Bandgap in 2D Semiconductors: MoSe 2 versus MoS 2. *Nano Letters* (2012).

23. Husain, E. *et al.* Marine Corrosion Protective Coatings of Hexagonal Boron Nitride Thin Films on Stainless Steel. *American Chemical Society* **5,** 4129–4135 (2013).

24. He, W. *et al.* Electrophoretic deposition of graphene oxide as a corrosion inhibitor for sintered NdFeB. *Applied Surface Science* **279,** 416–423 (2013).

25. Wonjoo Lee, Soon Hyung Kang, Jae-YupKim, Govind B Kolekar, Y.-E. S. and S.-H. H. TiO 2 nanotubes with a ZnO thin energy barrier for improved current efficiency of CdSe quantum-dot-sensitized solar cells. *IOPscience* (2009). doi:10.1088/0957-4484/20/33/335706

26. Stouwdam, J. W. Red , green , and blue quantum dot LEDs with solution processable ZnO nanocrystal electron injection layers †. *Journal of Materials Chemistry* 1889–1894 (2008). doi:10.1039/b800028j

27. Boukai, A., Xu, K. & Heath, J. R. Size-Dependent Transport and Thermoelectric Properties of Individual Polycrystalline Bismuth Nanowires. *Advanced Materials* **18,** 864–869 (2006).

28. L.D Hicks. Thermoelectric figure of merit of a one-dimensional conductor. *The American Physical Society* **47,** 8–11 (1993).

29. Kuchibhatla, S. V. N. T., Karakoti, A. S., Bera, D. & Seal, S. One dimensional nanostructured materials. *Progress in Materials Science* **52,** 699–913 (2006).

30. Ren, X., Zelenay, P., Thomas, S., Davey, J. & Gottesfeld, S. Recent advances in direct methanol fuel cells at Los Alamos National laboratory. *Journal of Power Sources* 111–116 (2000).

31. Kamarudin, S. K., Achmad, F. & Daud, W. R. W. Overview on the application of direct methanol fuel cell (DMFC) for portable electronic devices. *International Journal of Hydrogen Energy* **34,** 6902–6916 (2009).

32. M.Winter, R. J. B. What Are Batteries , Fuel Cells , and Supercapacitors ? *Chem.Rev.* **104,** 4245–4269 (2004).

33. Hor, Y. S. *et al.* Nanowires and Nanoribbons of Charge-Density-Wave Conductor NbSe 3. *Nano Letters* **5,** 397–401 (2005).

34. Lao, J. Y., Wen, J. G. & Ren, Z. F. Hierarchical ZnO Nanostructures. *Nano Letters* **2,** 1287–1291 (2002).

35. Williams, J. R., Dicarlo, L. & Marcus, C. M. Quantum Hall Effect in a gate-controlled p-n junction of graphene. *REPORTS* (2007).

36. Novoselov, K. S. *et al.* Electric Field Effect in Atomically Thin carbon film. *Science* (2004).

37. Reina, A. *et al.* Large Area , Few-Layer Graphene Films on Arbitrary Substrates by Chemical Vapor Deposition. *Nano Letters* 1–6 (2009).

38. Mao, N., Chen, Y., Liu, D., Zhang, J. & Xie, L. Solvatochromic Effect on the Photoluminescence of MoS2 Monolayers. 1312–1315 (2013). doi:10.1002/smll.201202982

39. Nair, R. R. *et al.* Fine Structure Constant Defines visual transparency of graphene. *BREVIA* **320,** 2–3 (2008).

40. Kotov, N. A. Carbon sheet solutions. *Nature* **442,** (2006).

41. Parvez, K. *et al.* Exfoliation of Graphite into Graphene in Aqueous Solutions of Inorganic Salts. *J. AM. CHEM. SOC.* (2014).

42. Soldano, C., Mahmood, A. & Dujardin, E. Production , properties and potential of graphene. *Carbon* **48,** 2127–2150 (2010).

43. L. Tedesco, G.G. Jernigan, J.C. Culbertson, J.K. Hite, Y. Yang, K.M. Daniels1, R.L. Myers-Ward1, C.R. Eddy, Jr., J.A. Robinson, K.A. Trumbull, M.T. Wetherington, P.M. Campbell, and D. K. G. Morphology Characterization of Argon-Mediated Epitaxial Graphene on C-face SiC. 1–12

44. A.L Vàzquez de Parga, Calleja, F., Borca, B., Hinarejos, J. J. & Miranda, R. Periodically rippled graphene: growth and spatially resolved electronic structure. 1–5 (2008).

45. Mattevi, C. & Chhowalla, M. A review of chemical vapour deposition of graphene on copper. 3324–3334 (2010). doi:10.1039/c0jm02126a

46. Pierson, H. O. *HANDBOOK OF CHEMICAL VAPOR DEPOS I TION (CVD)*. (1999).

47. Hicks, J., Shepperd, K. & Wang, F. The growth and morphology of epitaxial multilayer graphene. doi:10.1088/0953-8984/20/32/323202

48. Narayan, R. & Kim, S. O. Surfactant mediated liquid phase exfoliation of graphene. *Nano Convergence* (2015). doi:10.1186/s40580-015-0050-x

49. Ciesielski, A. & Samorì, P. Graphene via sonication assisted liquid-phase exfoliation. *Chem. Soc. Rev.* **43,** 381–398 (2014).

50. Fathi, D. A review of electronic band structure of graphene and carbon nanotubes using tight binding. *Journal of Nanotechnology* **2011,** (2011).

51. Www.unimuenster.de/imperia/md/images/physik_pi/zacharias/research/graphene & /graphene_band_structure.png. [51] www.unimuenster.de/imperia/md/images/physik_pi/zacharias/research/graphene /graphene_band_structure.png.

52. Neto, A. H. C., Guinea, F., Peres, N. M. R., Novoselov, K. S. & Geim, A. K. The electronic properties of graphene. *REVIEWS OF MODERN PHYSICS* **81,** (2009).

53. A. K. GEIM AND K. S. NOVOSELOV. The rise of graphene. *Nature Publishing Group* 183–191 (2007).

54. Chen, J. H., Jang, C., Xiao, S., Ishigami, M. & Fuhrer, M. S. Intrinsic and Extrinsic Performance Limits of Graphene Devices on SiO 2.

55. Allen, M. J., Tung, V. C. & Kaner, R. B. Honeycomb Carbon : A Review of Graphene. *Chem. Soc. Rev* 132–145 (2010).

56. Lee, C., Wei, X., Kysar, J. W. & Hone, J. Measurement of the elastic properties and intrinsic strenght of Monolayer Graphene. (2008).

57. Schedin, F. *et al.* Detection of individual gas molecules adsorbed on graphene. *letters* **6,** 6–9 (2007).

58. Miao, X. *et al.* High Efficiency Graphene Solar Cells by Chemical Doping. *Nano Letters* 6–11 (2012).

59. Brodie, B. C., Trans, P. & Lond, R. S. On the Atomic Weight of Graphite. *Philosophical Transactions of the Royal Society of London* 249–259 (1859).

60. U. Hofmann, E. Kç nig, Z. Anorg. Allg. Chem. 1937, 234, 311 – 336. [60] U. Hofmann, E. Kç nig, Z. Anorg. Allg. Chem. 1937, 234, 311 – 336.

61. Ayrat Dimiev,Dmitry V. Kosynkin, Lawrence B. Alemany,,‖ Pavel Chaguine, and J. M. T.

Pristine Graphite Oxide. *J. AM. CHEM. SOC.* (2012).

62. Singh, R. K., Kumar, R. & Singh, D. P. Graphene oxide: strategies for synthesis, reduction and frontier applications. *RSC Adv.* **6,** 64993–65011 (2016).

63. Bansal, T. *et al.* New insights into the density of states of graphene oxide using capacitive photocurrent spectroscopy. *Carbon* **50,** 808–814 (2011).

64. Stankovich, S. *et al.* Synthesis of graphene-based nanosheets via chemical reduction of exfoliated graphite oxide. *Carbon* **45,** 1558–1565 (2007).

65. Dreyer, D. R., Park, S., Bielawski, W. & Ruoff, R. S. The chemistry of graphene oxide. *Chemical Reviews* (2010). doi:10.1039/b917103g

66. Bai, H., Li, C. & Shi, G. Functional Composite Materials Based on Chemically Converted Graphene. *Advanced Materials* 1089–1115 (2011). doi:10.1002/adma.201003753

67. Fan, B. X. *et al.* Deoxygenation of Exfoliated Graphite Oxide under Alkaline Conditions : A Green Route to Graphene Preparation. *Advanced Materials* 4490–4493 (2008). doi:10.1002/adma.200801306

68. Zhang, J., Yang, H., Shen, G. & Cheng, P. Reduction of graphene oxide via L -ascorbic acid. *ChemComm* 1112–1114 (2010). doi:10.1039/b917705a

69. Salavagione, H. J. Promising alternative routes for graphene production and functionalization. *Journal of Materials Chemistry A* 7138–7146 (2014). doi:10.1039/c3ta15455f

70. Titelman, G. I., Gelman, V., Bron, S., Khalfin, R. L. & Cohen, Y. Characteristics and microstructure of aqueous colloidal dispersions of graphite oxide. *Carbon* **43,** 641–649 (2005).

71. Xia, Z. Y. *et al.* Synergic Exfoliation of Graphene with Organic Molecules and Inorganic Ions for the Electrochemical Production of Flexible Electrodes. *ChemPlusChem* 439–446 (2014). doi:10.1002/cplu.201300375

72. Cai, J. *et al.* Atomically precise bottom-up fabrication of graphene nanoribbons. *Nature* **466,** 470–473 (2010).

73. Kazmaier, P. M. & Hoffmannt, R. A Theoretical Study of Crystallochromy. Quantum Interference Effects in the Spectra of Perylene Pigments. *J. AM. CHEM. SOC.* 9684–9691 (1994).

74. W. Herbst, K. H. *Industrial Organic Pigments*. (2004).

75. F.Würthner. Perylene bisimide dyes as versatile building blocks for functional supramolecular architectures. *ChemComm* 1564–1579 (2004).

76. Ito, Y. *et al.* Crystalline Ultrasmooth Self-Assembled Monolayers of Alkylsilanes for

Organic Field-Effect Transistors. *J. AM. CHEM. SOC.* 9396–9404 (2009).

77. Heinz Langhals. CYCLIC CARBOXYLIC IMIDE STRUCTURES AS STRUCTURE ELEMENTS OF HIGH STABILITY . NOVEL DEVELOPMENTS IN PERYLENE DYE CHEMISTRY. *HETEROCYCLES* **40,** 477–500 (1995).

78. Blanco, R. & Segura, J. L. Spectroelectrochemical Study of Electron and Energy Transfer in Poly (fluorene- alt -phenylene) with Perylenediimide Pendant Groups. *J.Phys. Chem* 16668–16674 (2008).

79. Chang, Y., Kuo, M., Chen, C., Lu, H. & Chao, I. On the Air Stability of n -Channel Organic Field-Effect Transistors : A Theoretical Study of Adiabatic Electron Affinities of Organic Semiconductors. *J. Phys. Chem.* 11595–11601 (2010).

80. Sautter, A., Thalacker, C., Heise, B. & Wu, F. Hydrogen bond-directed aggregation of diazadibenzoperylene dyes in low-polarity solvents and the solid state. *PNAS* **99,** 4993–4996 (2002).

81. Jime, Ä. J., Spa, F., Salome, M., Fukuzumi, S. & Guldi, D. M. LETTERS A Tightly Coupled Bis (zinc (II) phthalocyanine) − Perylenediimide Ensemble To Yield Long-Lived Radical Ion Pair States †. *ORGANIC LETTERS* **9,** 2481–2484 (20007).

82. Jones, B. A., Facchetti, A., Wasielewski, M. R. & Marks, T. J. Tuning Orbital Energetics in Arylene Diimide Semiconductors . Materials Design for Ambient Stability of n-Type Charge Transport. *J. AM. CHEM. SOC.* **56,** 15259–15278 (2007).

83. Kippelen, B. Energy & Environmental Science. *Energy& Environmental Science* **2,** (2009).

84. Darling, S. B. Energy & Environmental Science. *Energy & Enviromental Science* **2,** 1266–1273 (2009).

85. Liang, Y. *et al.* Highly Efficient Solar Cell Polymers Developed via Fine-Tuning of Structural and Electronic Properties. *J. AM. CHEM. SOC.* 7792–7799 (2009).

86. Struijk, C. W. *et al.* Liquid Crystalline Perylene Diimides : Architecture and Charge Carrier Mobilities. *J. AM. CHEM. SOC.* 11057–11066 (2000).

Chapter II - THEORETICAL PRINCIPLE

2.1 Spectrophotometer technique

Electromagnetic radiation, or light, is a form of energy whose behaviour is described by the properties of both waves and particles. The optical properties of electromagnetic radiation, such as diffraction, are explained best by describing light as a wave. Many of the interactions between electromagnetic radiation and matter, such as absorption and emission, however, are better described by treating light as a particle, or photon.

Electromagnetic radiation consists of oscillating electric and magnetic fields that propagate through space along a linear path and with a constant velocity (figure 1). In a vacuum, electromagnetic radiation travels at the speed of light, c, which is 2.99792 x 10^8 m/s.

Electromagnetic radiation moves through a medium other than a vacuum with a velocity, v, less than that of the speed of light in a vacuum.
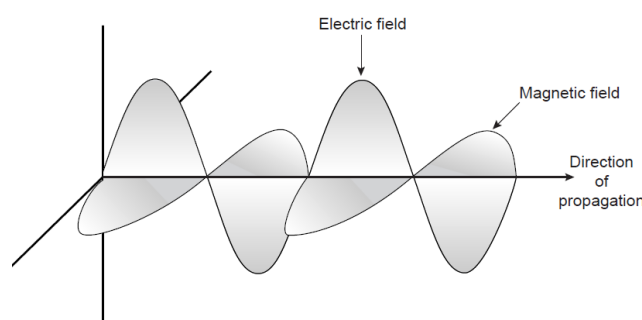
Figure 33: Plane-polarized electromagnetic radiation showing the electric field, the magnetic field, and the direction of propagation.[1]

The wavelength of an electromagnetic wave, is defined as the distance between successive maxima, or successive minima (see figure 34). The A_e is the electric field's maximum amplitude. For ultraviolet and visible electromagnetic radiation the wavelength is usually expressed in nanometers (nm, 10^{-9} m), and the wavelength for infrared radiation is given in microns (mm, 10^{-6} m).[1]
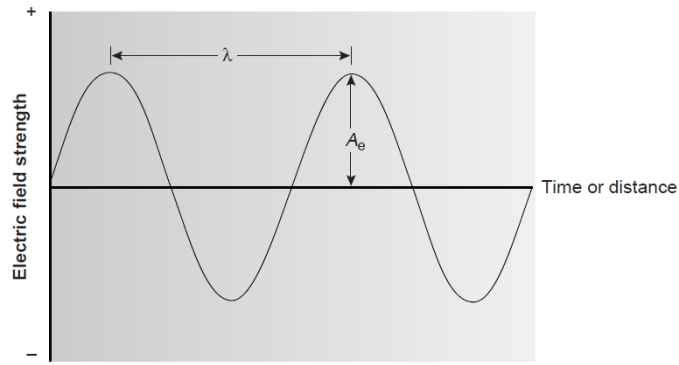
Figure 34: Electric field strength vs time. [1]

When a sample absorbs electromagnetic radiation it go through a change in energy. The interaction between the sample and the electromagnetic radiation (photons) **i**ncrease the energy acquired by the sample. The energy of a photon, in joules, is related to its frequency, wavelength, or wavenumber by the following equations:

$$E = hc\nu$$

Where E is the energy, h where h is Planck's constant, which has a value of $6.626 * 10^{-34}$ J $\cdot$ s, c is the light speed and v is the frequency. The spectrophotometer scheme is shown in the figure 35:
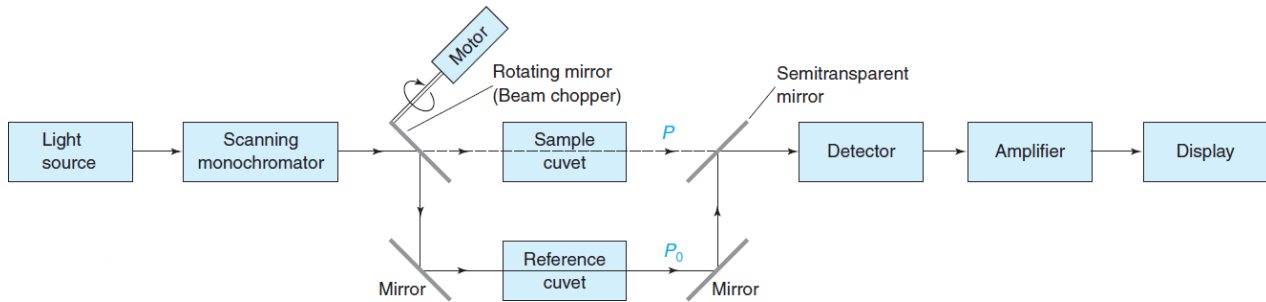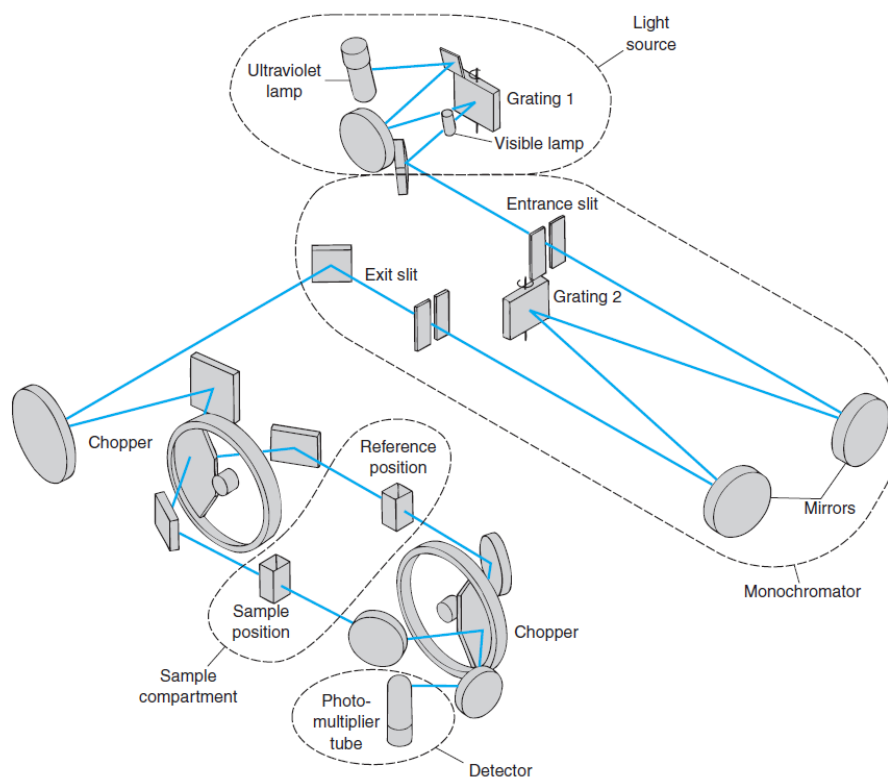
Figure 35: The spectrophotometer operating scheme. Adapted with permission from Varian Australia Pty.Ltd.,Victoria, Australia.[1]

When light is absorbed by a sample, the *irradiance* of the beam of light is decreased. The output signal, by spectrophotometer, is given in absorbance. Absorbance is so important because it is directly proportional to the concentration, *c*, of the light-absorbing species (chromophore) in the sample, by beer's law.

$$\text{Beer's law: } A = \varepsilon \, b \, c$$

The concentration of the sample, *c*, is usually given in units of moles per liter (M). The pathlength, *b*, is commonly expressed in centimeters. The quantity (epsilon) is called the molar absorptivity (or *extinction coefficient*) and has the units $M^{-1} \, cm^{-1}$ to make the product *bc* dimensionless. Molar absorptivity is the characteristic of a substance that tells how much light is absorbed at a particular wavelength.[2]

2.2 Spectroscopy based on emission

An analyte in an excited state possesses an energy, E_2, which is greater than that when it is in a lower energy state, E_1. When the analyte returns, or relaxes to a lower energy state (ground state) the excess energy, ΔE,

$$\Delta E = E_2 - E_1$$

Relaxation occurs through collisions between A^* and other species in the sample, by photochemical reactions, and by the emission of photons. In the first process, which is called vibrational deactivation, or nonradiative relaxation, the excess energy is released as heat. In either case the excess energy the is released as a photon of electromagnetic radiation.

$$A^* \rightarrow A + h\nu$$

The release of a photon following thermal excitation is called emission, and that following the absorption of a photon is called photoluminescence.

Photoluminescence is divided into two categories: fluorescence and phosphorescence. Absorption of an ultraviolet or visible photon promotes a valence electron from its ground state to an excited state with conservation of the electron's spin. For example, a pair of electrons occupying the same electronic ground state have opposite spins (figure 36) and are said to be in a singlet spin state. Absorbing a photon promotes one of the electrons to a singlet excited state. Emission of a photon from a singlet excited state to a singlet ground state, or between any two energy levels with the same spin, is called fluorescence.
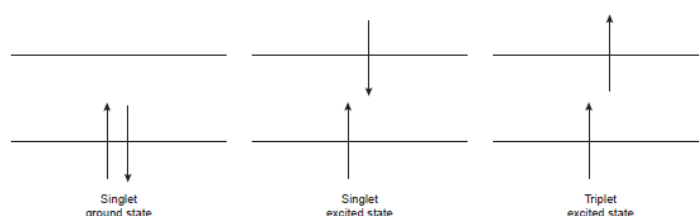
Figure 36: Difference between singlet and triplet states

Fluorescence, therefore, decays rapidly after the excitation source is removed. In some cases an electron in a singlet excited state is transformed to a triplet excited state in which its spin is no longer paired with that of the ground state. Emission between a triplet excited state and a singlet ground state, or between any two energy levels that differ in their respective spin states, is called phosphorescence. Because the average lifetime for phosphorescence ranges from 10^{-4} to 10^4 s, phosphorescence may continue for some time after removing the excitation source. Molecular fluorescence and, have been used for the direct or indirect quantitative analysis of analytes in a

variety of matrices. A direct quantitative analysis is feasible when the analyte's quantum yield for fluorescence is favorable.[3]

In general the quantum yield is calculate respect to a standard molecules where is know the physical-chemical properties (quantum yield, refractive index, density etc). The quantum yield, of new matrix is calculated by the following equations:

$$\Phi = \Phi_r*(I/I_r)*(A_r/A)*(n^2/n^2_r)$$

Where Φ_r is the quantum yield, A is the absorbance at the excitation wavelength, n is the refractive index of solvent; r is reference.[4]

2.3 Surface area and pore structure by gas adsorption (BET)

A relative great proportion of the atoms to of a fine powder are in or near the surface. If, in addition, the powder particles have cracks, crevices or pores within their structure, the proportion of exposed atom is still greater. This causes powders to exhibit distinctly different properties from the same material in bulk from and to do so in a manner strongly dependent on the magnitude of their surface area and the nature of their porosity. A fine powder is more reactive than the same material in bulk; it shows enhanced solubility; it sinters at low temperature; it has more adsorptive capacity; and it exhibits greater catalytic activity. Gas adsorption in solid surface and pore spaces is a complex phenomena involving mass and energy interaction and phase changes. The physical adsorption of gases by solid increases with decreasing temperature and with increase pressure. The process is exothermic, i.e., energy is released. The kinetics and thermodynamics of adsorption have been extensively studied, but, when surface area and pore structure are the subjects of interest, the investigate procedure is first to establish what is known as an adsorption (desorption) isotherm. This, quite simply, is a measure of the molar quantity of gas n (or standard volume V_a) taken up, or released, at a constant temperature T by an initially clean solid surface as a function of a gas pressure P. most frequently the test is conducted at a cryogenic temperature, usually that of a liquid nitrogen (LN_2) at its boiling point (77.35 K at atmospheric pressure). Convention has establish that the quantity of gasses adsorbed is expressed as its volume at standard condition of T and P (0°C and 760 torr and signified STP) while the pressure is expressed as a relative pressure which is the actual gas pressure P divided by the vapor pressure P_0 of the adsorbing gas at the temperature which the test is conducted. These data having been gathered at one temperature , constitute the adsorption (desorption) isotherm for the material in question. Plots of V_a as the ordinate against P/P_0 as the abscissa reveal much about the structure of the adsorbing material (called the adsorbent) simply

from their shape. Adsorption isotherms generally follow one of the six behavior. In this thesis we focus about only one, that can be shown in the figure 37:
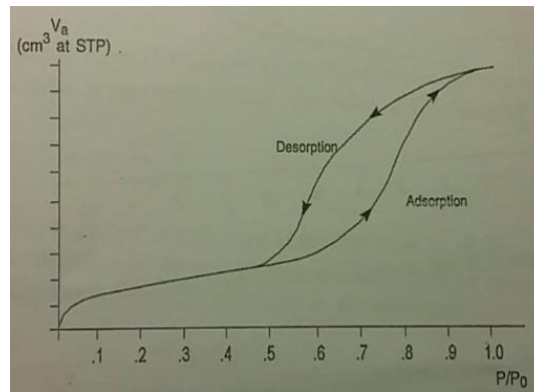
Figure 37: Adsorption and desorption isotherms for a porous solid

The adsorption curve of figure 5 has the typical behavior of mesoporous and macroporous materials, i.e., those that have pores with opening greater than 2 nm and 50 nm respective. The Langmuir theory development more properly applies to chemisorption situations than to physical adsorption ones because its first assumption is that gases form only one molecular layer on solid. Collision on a gas molecules with a solid is taken to be inelastic, so that the gas molecule remaining in contact with the solid for a time before returning to the gas phase. This time delay is taken as responsible for the phenomena of adsorption. In this specific case the surface area of the adsorbent (the area of 1 g of it) is then calculates from:

$$s = V_m \sigma N_A / m V_0$$

Where σ is the area of surface occupied by a single adsorbed gas molecule (1,62 nm in the case of nitrogen), N_A the Avogadro constant (6,023 x10^{23} molecules/moles), m the mass of the adsorbing sample, and V_0 the molar volume of the gas (22414 cm^3). When nitrogen is the adsorptive, the equation, shown before, becomes:

$$s \ (m^2/g) = 4,35 Vm(cm^3 \text{ at STP})/m(g)$$

2.4 TGA

Thermogravimetric analysis or thermal gravimetric analysis (TGA) is a method of thermal analysis in which changes in physical and chemical properties of materials are measured as a

function of increasing temperature, or as a function of time. Thermogravimetric Analysis (TGA) measures the amount and rate of change in the weight of a material as a function of temperature or time in a controlled atmosphere (inert atmosphere (nitrogen) or in reactive atmosphere (O_2 /air). Measurements are used primarily to determine the composition of materials and to predict their thermal stability at temperatures up to 1200°C. The technique can characterize materials that exhibit weight loss or gain due to decomposition, oxidation, or dehydration. A TGA analysis gave a lot of information, i.e., 1)Thermal Stability of Materials 2) Oxidative Stability of Materials 3) Composition of Multi-component Systems 4) Estimated Lifetime of a Product 5) Decomposition Kinetics of Materials 6) The Effect of Reactive or Corrosive Atmospheres on Materials 7) Moisture and Volatiles Content of Materials. The mechanisms of weight change in TGA are in divided in two different category:

1. Weight Loss :
   – Decomposition: The breaking apart of chemical bonds.
   – Evaporation: The loss of volatiles with elevated temperature.
   – Reduction: Interaction of sample to a reducing atmosphere (hydrogen, ammonia, etc.).
   – Desorption

2. Weight Gain:
   – Oxidation: Interaction of the sample with an oxidizing atmosphere.
   – Absorption

The functional scheme of TGA analysis is shown in figure 38:
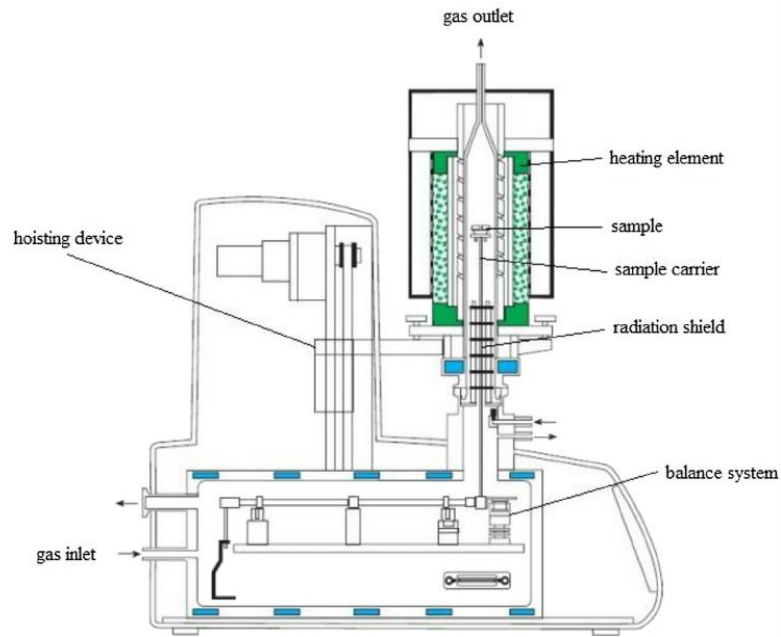
Figure 38: TGA operative scheme

The balance operates on a null-balance principle. At the zero, or "null" position equal amount of light shine on two photodiodes. If the balance moved out of the null position an equal amount of light shines on the two photodiodes. Current is then applied to the meter movement to return the balance to the null position. The amount of current applied is proportional to the weight loss or gain.[5]

2.5 DSC

Differential scanning calorimetry or DSC is a thermoanalytical technique to study what happens to samples when they are heated. DSC measures the amount of energy absorbed or released by a sample when it is heated or cooled, providing quantitative and qualitative data on endothermic (heat absorption) and exothermic (heat evolution) processes. DSC is used to measure melting temperature, heat of fusion, latent heat of melting, reaction energy and temperature, glass transition temperature, crystalline phase transition temperature and energy, precipitation energy and temperature, denaturization temperatures, oxidation induction times, and specific heat or heat capacity. Only non-corrosive samples can be analyzed in this very sensitive instrument. No organic or other materials containing F, Cl, Br, or I may be submitted for DSC analysis without our knowledge. The operative schema of DSC is shown in figure 39:
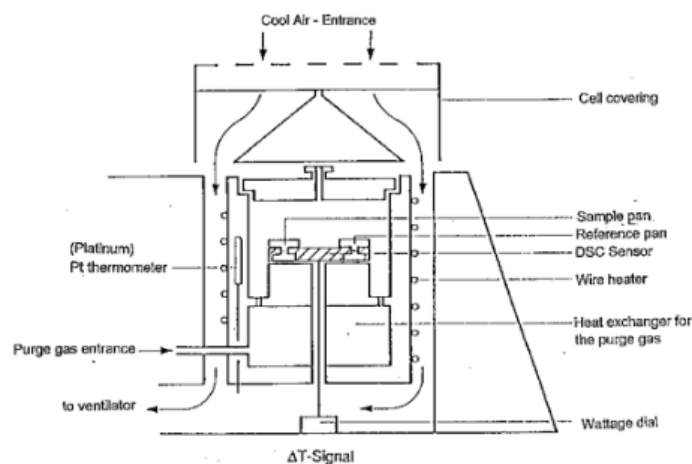
Figure 39: DSC schematic instrument

There are two pans. In one pan, the sample pan, there is the sample. The other one is the reference pan. Each pan sits on top of a heater. There are a lot of Pans but the principal are in Al, Cu, Au, Pt, alumina, and graphite are available and need to be chosen to avoid reactions with samples. It can be choosing the atmospheres: nitrogen, air, oxygen, argon, vacuum, controlled mixed gases that it can be change on the basis of the samples typology. In the measurement chamber are placed two pans: The sample pan, where the sample under investigation is located. The reference pan, which normally is left empty. Each pan is positioned on the top of a heater. Via a computer interface, it is possible select the rate of the heating of the two pans; usually it is set to ca. 10 °C/min. The adsorption of heat will be different in the two pans due to the different composition in the pan. In order to keep the temperature of the two pans constant during the experiment, the system needs to provide more or less heat to one of the two pans. The output of the DSC experiment is the additional quantity of heat which is given to the pan in order to keep the temperature of the two pans equal. In other words, the output of the DSC is a plot of the difference in heat output of the two heaters vs. temperature (T). The heat capacity (Cp) of a system is the quantity of heat needed to raise the temperature of the system of 1 °C. It is usually given in units of Joules/°C. It can be derived introducing two parameters, namely the heat flow and heating rate. Whilst the heat flow is the heat (q) supplied per unit time (t), the heating rate is variation of temperature (ΔT) per unit time (t), namely:

$$\frac{heat}{time} = \frac{q}{t} = heat\ flow\ ; \quad \frac{temperature\ increase}{time} = \frac{\Delta T}{t} = heating\ rate$$

The ratio about heat flow and heating rate gave, the heat capacity Cp.

At the melting temperature (Tm) the compound are allowed to move around freely, thus they do not possess an ordered arrangements. Upon melting the compound absorb heat, thus melting is an endothermic transition. The melting is a first order transition since when the melting temperature is reached; the compound's temperature does not rise until all the crystals have completely melted. In the figure 40 is shown the heat flow vs T for melting processes.
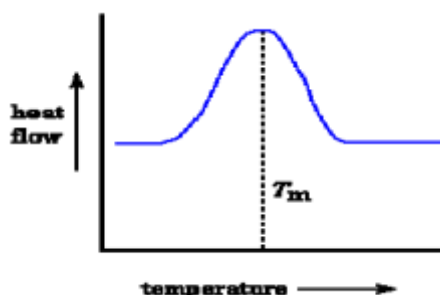
Figure 40:DSC analysis for the melting processes

When the matrix fall into these crystalline arrangements, they give off heat to the system, thus the process is exothermic. In fact the heat flow drops as one can note from the big dip in the plot of (q/t) vs. T [6]:
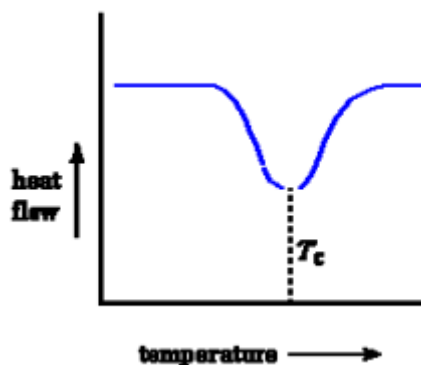
Figure 41:DSC analysis for the crystalline arrangements

2.6 ICP

In principle, emission spectroscopy can be applied to both atoms and molecule. Atomic emission occurs when a valence electron in a higher-energy atomic orbital returns to a lower-energy atomic orbital. An atomic emission spectrum, therefore, consists of a series of discrete lines at wavelengths corresponding to the difference in energy between two atomic orbitals. The intensity, I, of an emission line is proportional to the number of atoms, N^*, populating the excited state:

$$I = k \, N^*$$

where *k* is a constant related to the efficiency of the transition. For a system in thermal equilibrium, the population of the excited state is related to the total concentration of atoms, *N,* by the Boltzmann distribution. For many elements at temperatures of less than 5000 K the Boltzmann distribution for the *i*-th excited state is approximated as:

$$N^* = N_0 \, (g_i/g_0) e^{-(E_i/kT)}$$

where g_i and g_0 are statistical factors accounting for the number of equivalent energy levels for the excited state and ground state, E_i is the energy of the excited state relative to that of the ground state ($E_0 = 0$), k is Boltzmann's constant ($1.3807 * 10^{-23}$ J/K), and T is the temperature in Kelvin.

Inductively coupled plasma mass spectrometry (ICP-MS) is a type of mass spectrometry which is capable of detecting metals and several non-metals at concentrations as low as one part in 10^{15} (part per quadrillion, ppq) on non-interfered low-background isotopes.

This is achieved by ionizing the sample with inductively coupled plasma and then using a mass spectrometer to separate and quantify those ions.[7]

A plasma consists of a hot, partially ionized gas, containing an abundant concentration of cations and electrons that make the plasma a conductor. The plasmas used in atomic emission are formed by ionizing a flowing stream of argon, producing argon ions and electrons. The high temperatures in a plasma result from resistive heating that develops due to the movement of the electrons and argon ions. Because plasmas operate at much higher temperatures than flames, they provide better atomization and more highly populated excited states. Besides neutral atoms, the higher temperatures of a plasma also produce ions of the analyte. The ICP torch consists of three concentric quartz tubes, surrounded at the top by a radio-frequency induction coil. The sample is mixed with a stream of Ar using a spray chamber nebulizer similar to that used for flame emission and is carried to the plasma through the torch's central tube. A radiofrequency current in the induction coils creates a fluctuating magnetic field that induces the argon ions and electrons to move in a circular path. Atomic emission spectroscopy is ideally suited for multielemental analysis because all analytes in a sample are excited simultaneously. A scanning monochromator can be programmed to move rapidly to an analyte's desired wavelength, pausing to record its emission intensity before moving to the next analyte's wavelength. In figure 42 is shown an operative scheme of ICP:
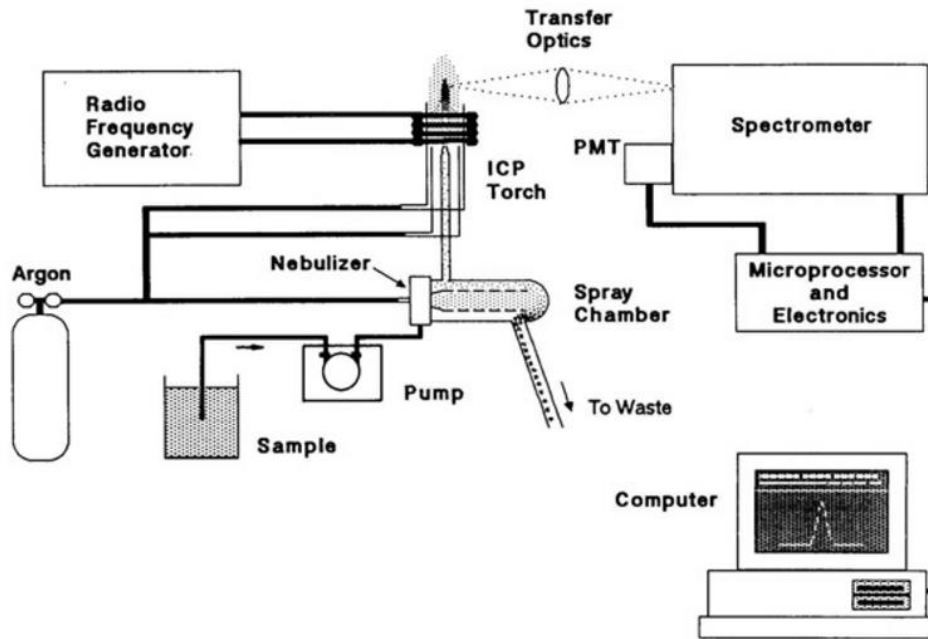
Figure 42: ICP operative scheme[8]

2.7 XRD

X-ray diffraction (XRD) is one of the most important non-destructive tools to analyse all kinds of matter -ranging from fluids, to powders and crystals. From research to production and engineering, XRD is an indispensible method for structural materials characterization and quality control which makes use of the Debye-Scherrer method. This technique uses X-ray (or neutron) diffraction on powder or microcrystalline samples, where ideally every possible crystalline orientation is represented equally. The resulting orientation averaging causes the three dimensional reciprocal space that is studied in single crystal diffraction to be projected onto a single dimension. Diffraction effects are observed when electromagnetic radiation impinges on periodic structures with geometrical variations on the length scale of the wavelength of the radiation. The interatomic distances in crystals and molecules amount to 0.15–0.4 nm which correspond in the electromagnetic spectrum with the wavelength of x-rays having photon energies between 3 and 8 keV.

X-rays are generated in an X-ray tube, in which a target material (Cu, Fe, Mo, or Cr) is excited using an electron beam, causing inner shell electrons to be ejected and replaced by electrons from higher energy outer orbitals. This interaction produces X-rays that are characteristic of the target material, which are then filtered and concentrated into a monochromatic incident beam of X-rays that is focused on the sample. Interactions between the incident X-ray beam and the sample produce intense reflected X-rays by constructive interference when conditions satisfy Bragg's Law ($n \lambda = 2d \sin\theta$). This law describes the general relationship between the wavelength of the incident X-rays,

the incident angle of the beam, and the spacing between the crystal lattice planes of atoms. Constructive interference occurs when the differences in the travel path of the incident X-rays is equal to an integer multiple of the wavelength. When this occurs, a diffracted X-ray beam leaves the crystal at the same angle as the incident angle (θ). Diffracted X-rays are detected, processed, and counted as the sample is scanned through a range of 2θ angles. This method allows for all possible diffraction directions (for X-rays of a fixed wavelength) produced through beam interaction with a unique crystalline substance to be measured during analysis (i.e. the diffraction pattern). Identification of the specific mineral phase is achieved by converting the diffraction peaks to d-spacings and comparing the d-spacings to those known from analysis of standard reference materials.[9,10] In figure 43 is shown an operative scheme of XRD:
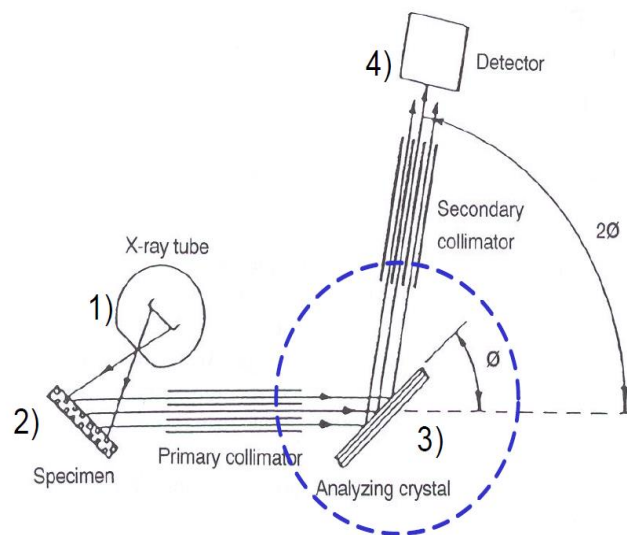
Figure 43: XRD operative scheme[10]

2.8 EDS/EDX

EDS or energy-dispersive X-ray spectroscopy, makes use of the X-ray spectrum emitted by a solid sample bombarded with a focused beam of electrons to obtain a localized chemical analysis. All elements from atomic number 4 (Be) to 92 (U) can be detected in principle, though not all instruments are equipped for 'light' elements (Z<10). Qualitative analysis involves the identification of the lines in the spectrum and is straightforward owing to the simplicity of X-ray spectra. Quantitative analysis (determination of the concentrations of the elements present) entails measuring line intensities for each element in the sample and for the same elements in calibration Standards of known composition. By scanning the beam in a television-like raster and displaying the intensity of a selected X-ray line, element distribution images or 'maps' can be produced. In addition, images produced by electrons collected from the sample reveal surface topography or

mean atomic number differences according to the mode selected. The scanning electron microscope (SEM), which is closely related to the electron probe, is designed primarily for producing electron images, but can also be used for element mapping, and even point analysis, if an X-ray spectrometer is added. There is thus a considerable overlap in the functions of these instruments. Energy-dispersive spectrometers (EDSs) employ pulse height analysis: a detector giving output pulses proportional in height to the X-ray photon energy is used in conjunction with a pulse height analyzer (in this case a multichannel type). A solid state detector is used because of its better energy resolution. Incident X-ray photons cause ionization in the detector, producing an electrical charge, which is amplified by a sensitive preamplifier located close to the detector. Both detector and preamplifier are cooled with liquid nitrogen to minimize electronic noise.[11,12] In figure 44 is shown an operative scheme of EDX:
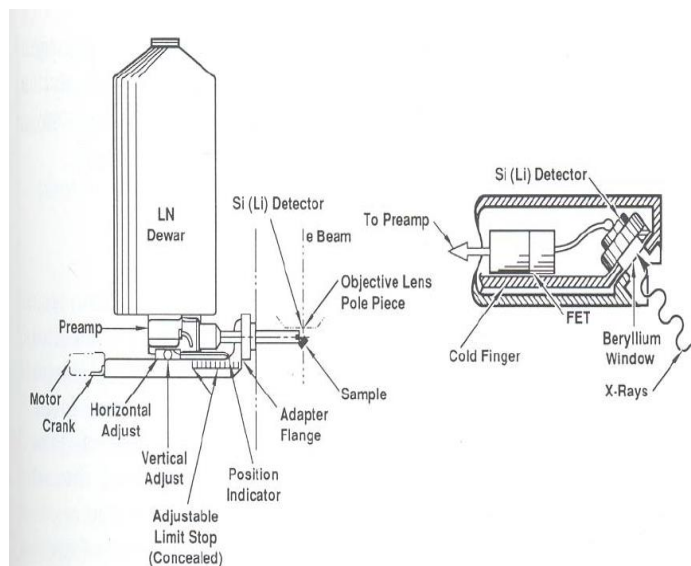
Figure 44: EDX/EDS operative scheme[11]

2.9 SEM

The scanning electron microscope (SEM) uses a focused beam of high-energy electrons to generate a variety of signals at the surface of solid specimens. The signals that derive from electron-sample interactions reveal information about the sample including external morphology (texture), chemical composition, and crystalline structure and orientation of materials making up the sample. In most applications, data are collected over a selected area of the surface of the sample, and a 2-dimensional image is generated that displays spatial variations in these properties. Areas ranging from approximately 1 cm to 5 microns in width can be

imaged in a scanning mode using conventional SEM techniques (magnification ranging from 20X to approximately 50,000X, spatial resolution of 50 to 100 nm).

The SEM is also capable of performing analyses of selected point locations on the sample; this approach is especially useful in qualitatively or semi-quantitatively determining chemical compositions (using EDS), crystalline structure, and crystal orientations (using EBSD). Accelerated electrons in an SEM carry significant amounts of kinetic energy, and this energy is dissipated as a variety of signals produced by electron-sample interactions when the incident electrons are decelerated in the solid sample. These signals include secondary electrons (that produce SEM images), backscattered electrons (BSE), diffracted and heat. Secondary electrons and backscattered electrons are commonly used for imaging samples: secondary electrons are most valuable for showing morphology and topography on samples and backscattered electrons are most valuable for illustrating contrasts in composition in multiphase samples (i.e. for rapid phase discrimination). X-ray generation is produced by inelastic collisions of the incident electrons with electrons in discrete orbitals (shells) of atoms in the sample. As the excited electrons return to lower energy states, they yield X-rays that are of a fixed wavelength (that is related to the difference in energy levels of electrons in different shells for a given element). Thus, characteristic X-rays are produced for each element in a mineral that is "excited" by the electron beam. SEM analysis is considered to be "non-destructive"; that is, x-rays generated by electron interactions do not lead to volume loss of the sample, so it is possible to analyze the same materials repeatedly.[13]

In figure 45 is shown an operative scheme of Scanning electron microscope:
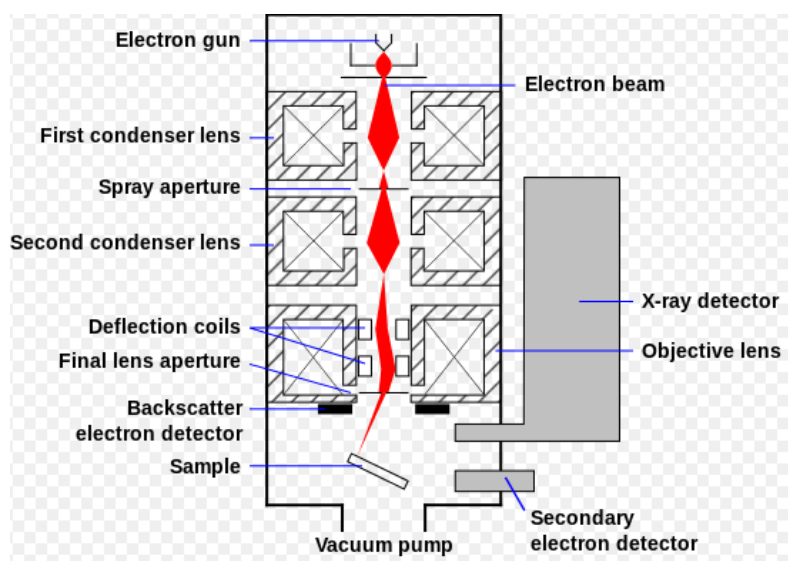
Figure 45: Operative scheme of scanning electron microscopy

2.10 Particle size distribution

Particle size influences many properties of particulate materials and is a valuable indicator of quality and performance. The size and shape of powders influences flow and compaction properties. Larger, more spherical particles will typically flow more easily than smaller or high aspect ratio particles. Smaller particles dissolve more quickly and lead to higher suspension viscosities than larger ones. Smaller droplet sizes and higher surface charge (zeta potential) will typically improve suspension and emulsion stability. Powder or droplets in the range of 2-5μm aerosolize better and will penetrate into lungs deeper than larger sizes. The measure of the size can be conduct considering the particle like a sphere. A spherical particle can be described using a single number the diameter because every dimension is identical. In the case of non-spherical particles can be described using multiple length and width measures (horizontal and vertical projections are shown here). These descriptions provide greater accuracy, but also greater complexity. Thus, many techniques make the useful and convenient assumption that every particle is a sphere. The reported value is typically an equivalent spherical diameter. This is essentially taking the physical measured value (i.e. scattered light, settling rate) and determining the size of the sphere that could produce the data. Although this approach is simplistic and not perfectly accurate, the shapes of particles generated by most industrial processes are such that the spherical assumption does not cause serious problems. Problems can arise, however, if the individual particles have a very large aspect ratio, such as fibers or needles. A light scattering device will average the various dimensions as the particles flow randomly through the light beam, producing a distribution of sizes from the smallest to the largest dimensions.

The only techniques that can describe particle size using multiple values are microscopy or automated image analysis. When reporting a particle size distribution the most common format used even for image analysis systems is equivalent spherical diameter on the x axis and percent on the y axis.

Another common approach to define the distribution width is to cite three values on the x-axis, the D_{10}, D_{50}, and D_{90} as shown in figure 46. The D_{50}, the median, has been defined as the diameter where half of the population lies below this value. Similarly, 90 percent of the distribution lies below the D_{90}, and 10 percent of the population lies below the D_{10}.[14]
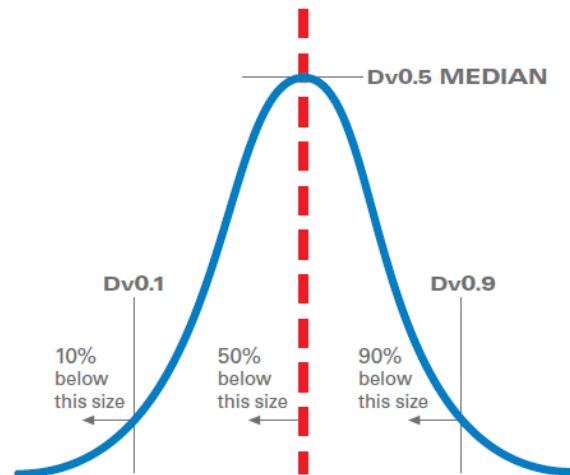
Figure 46: Three x-axis values D$_{10}$, D$_{50}$ and D$_{90}$ [14]

2.11 AFM:

The atomic force microscope (AFM) is one kind of scanning probe microscopes (SPM). SPMs are designed to measure local properties, such as height, friction, magnetism, with a probe. To acquire an image, the SPM raster-scans the probe over a small area of the sample, measuring the local property simultaneously. AFMs operate by measuring force between a probe and the sample. Normally, the probe is a sharp tip, which is a 3-6 um tall pyramid with 15-40 nm end radius (figure 47). Though the lateral resolution of AFM is low (~30nm) due to the convolution, the vertical resolution can be up to 0,1nm.
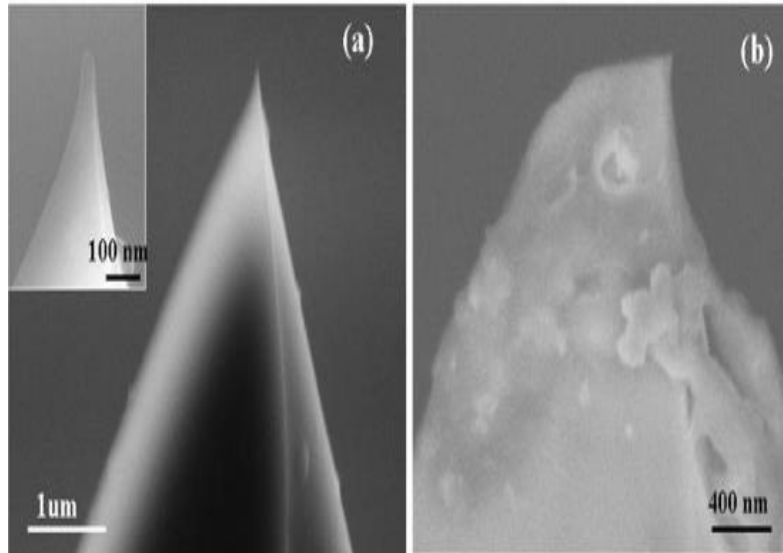
Figure 47: (a) A new AFM tip; inset: The end of the new tip. (b) A used AFM tip.

To acquire the image resolution, AFMs can generally measure the vertical and lateral deflections of the cantilever by using the optical lever. The optical lever operates by reflecting a laser beam off the cantilever. The reflected laser beam raids a position-sensitive photo-detector consisting of four-segment photo-detector. The differences between the segments of photo-detector of signals indicate the position of the laser spot on the detector and thus the angular deflections of the cantilever (figure 48).
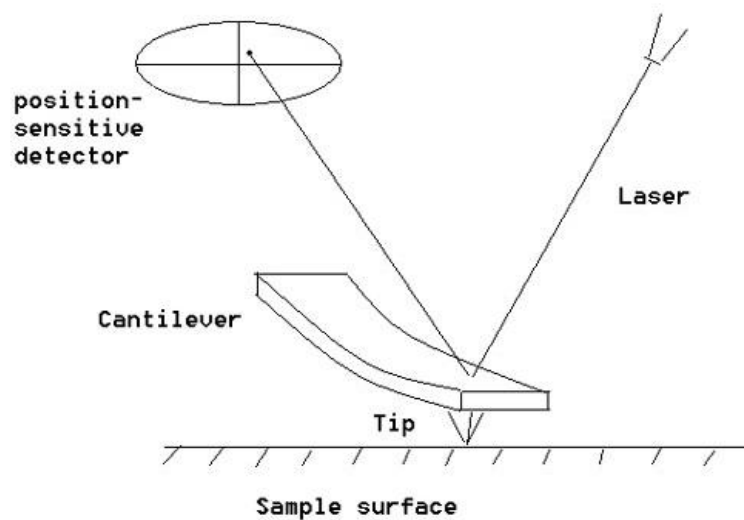
Figure 48: AFM that working with an optical lever

Piezo-ceramics position the tip with high resolution. Piezoelectric ceramics are a class of materials that expand or contract when in the presence of a voltage gradient. Piezo-ceramics make it possible to create three-dimensional positioning devices of arbitrarily high precision. In contact mode, AFMs use feedback to regulate the force on the sample. The AFM not only measures the force on the sample but also regulates it, allowing acquisition of images at very low forces. The feedback loop consists of the tube scanner that controls the height of the tip; the cantilever and optical lever, which measures the local height of the sample; and a feedback circuit that attempts to keep the cantilever deflection constant by adjusting the voltage applied to the scanner.[15]

2.12 Fluorescence microscope:

Fluorescence microscopy is a special form of light microscopy. It uses the ability of fluorochromes to emit light after being excited with light of a certain wavelength. A fluorescence microscope (upright or inverted) is similar to an ordinary light microscope, except that the illumination is provided by a laser as monochromatic light or a bright and powerful light source like a mercury-vapor or a xenon arc lamp. In addition, it contains an excitation filter and an emission filter. The excitation filter transmits only light that is able to excite the specimen with its particular dye. The light emitted by the specimen has to pass through the emission filter before it reaches the detector. The emission filter is only translucent for light with a distinct wavelength, like the light emitted by the specimen. In figure 49 is shown the operative scheme of fluorescence microscope.
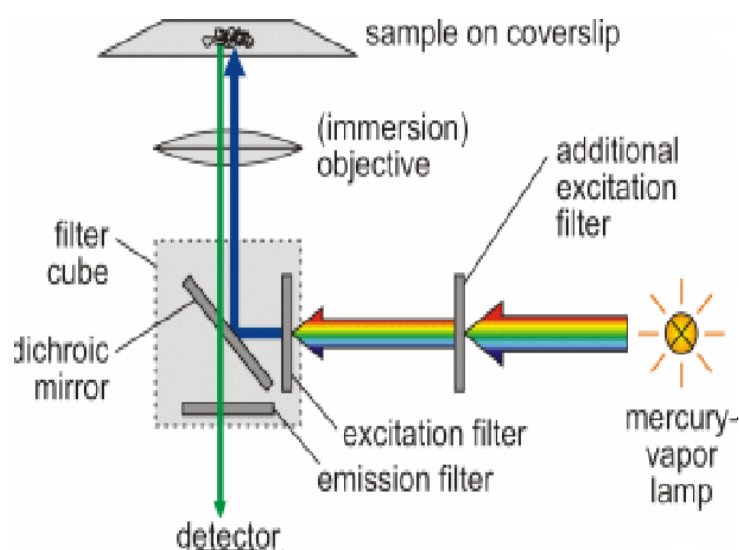
Figure 49: Light path through a fluorescence microscope[16]

Most fluorescence microscopes are epi-fluorescence microscopes. The illuminator and objective lens are positioned on the same side of the specimen and the light does not pass through the specimen. Besides the excitation and the emission filter, a dichroic mirror is needed for this kind of fluorescence microscope. A dichroic mirror allows light of a certain wavelength to pass through, while light of other wavelengths is reflected. The filters and the dichroic mirror are often plugged in together in a filter cube (figure 50).
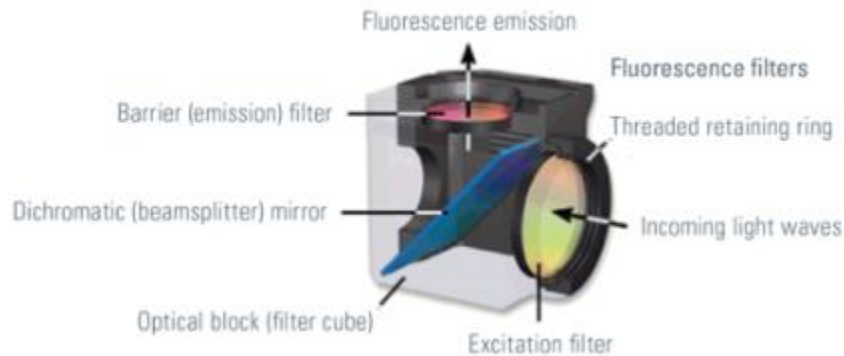
Figure 50: Principle of a dichroic cube[16]

The excitation light passes through the excitation filter and is directed to the dichroic mirror. This reflects the light through the objective towards the specimen. Fluorochromes in the specimen are excited and emit photons. This emission light passes back through the objective to the dichroic mirror. The emitted light has an appropriate wavelength and is able to pass. Excitation light that is reflected by the specimen is not able to pass through the dichroic mirror and will be blocked. If excitation light is able to pass through the dichroic mirror it will be blocked when it reaches the emission filter. Light passing through the emission filter can be measured with a detector.[17]

REFERENCE

1. Harvey, D. Modern Analytical Chemistry. *Mc Graw Hill* 543–621 (2000). doi:10.1136/jcp.30.1.93-a

2. http://teaching.shu.ac.uk/hwb/chemistry/tutorials/molspec/uvvisab1.htm.

3. PerkinElmer. An Introduction to fluorescence spectroscopy. *PerkinElmer, Inc.* 1–36 (2000). doi:10.1016/S0026-265X(00)00048-5

4. Guidebook to particle size analysis.

5. Dean, D. Thermal Gravimetric Analysis. *University of Alabama at Birmingham* 1–77 (2015). doi:10.1016/0025-5416(80)90238-4

6. Rabe, P. Differential scanning calorimetry investigation of polymers. *HUMBOLDT-UNIVERSITÄT ZU BERLIN* 1–17 (2011).

7. Thomas, R. A guide to ICP-MS. *Spectroscopy* **16,** 38–42 (2001).

8. spettro_plasma @ lac.chem.polimi.it.

9. Lindsay, F. J. M. X-ray Diffraction (XRD). **5,** 371–372 (1970).

10. Diffraction, X. & Xrd, C. S. X-Ray Diffraction and Crystal Structure. doi:10.1002/9780470823002

11. Noran. Energy-Dispersive X-ray Microanalysis. *Noran Instruments* 68 (1999). doi:10.1007/BF01567579

12. Energy Dispersive X-ray Spectrometry and X-ray Microanalysis X-ray Microanalysis.

13. Egerton, R. F. *Physical Principles of Electron Microscopy. Materials Today* (2016). doi:10.1007/978-3-319-39877-8

14. Scientific, H. a Guidebook To Particle Size Analysis. *Distribution* 1–17 (2010).

15. All., J. V. ; M. sendne. et. Atomic Force Microscopy. *Karls Universität Heidelberg Kirchhoff-Institut für Physik* (2014).

16. http://www.microfilm.net.au/glossary-imaging-scanning-related-terms-compiled-laurie-varendorff-digital-microfilm-equipment-dme/.

17. Spring, K. R. Fluorescence Microscopy. (2011). doi:10.1081/E-EOE

Chapter III - ANALYTICAL METHODS FOR DETERMINATION OF THE INTERACTION BETWEEN PERYLENE DIIMIDES AND GRAPHITE SUBSTRATES

All the molecules used for the various assays (PDI and graphite) were purchased through Sigma Aldrich and dissolved in chloroform until reaching a final concentration of 1.125×10^{-5} M. The dissolution was carried out using magnetic stirring and heating the whole mixture at a temperature of 55 ° C for 1 hour. After 1 hour of heating, the bottles containing the solutions were wrapped into aluminum foil and placed in the dark in order to avoid possible interactions with light. The characteristics of the used compounds are listed below.

Table 2: Physical chemical characteristics of the molecules employed

Reagents	CAS Number	Molecular Weight (g/mol)	Melting point(°C)
PDI-H	67075-37-0	598.65	410-415
PDI-F	215726-57-1	634.63	368-370
PDI-Cl	215726-51-5	667.54	390-392
Graphite Flakes	7782-42-5	12.01	3652-3697

For spectrophotometric and fluorimetric meauserments, all the solutions, with and without graphite, were filtered using "CHROMAFIL® XTRA H-PTFE-45/25" filters, i.e. (id est) filters with a mesh size of 25 μm. The use of these filters excludes, in subsequent analyzes, the presence of graphite particles larger than 25 μm.

3.1 Spectrophotometric assay

Any substance solicited by electromagnetic radiation, such as light radiation, absorbs in a variable amount the energy that comes from it, utilizing it for an increase in molecular energy, moving from a "fundamental" energy state to an "excited" state.When light is absorbed by a sample, the *irradiance* of the beam of light is decreased. The output signal, by spectrophotometer, is given in absorbance. Absorbance is so important because it is directly proportional to the concentration, c, of the light-absorbing species (chromophore) in the sample, by Beer's law.

The solutions described above, were used to perform the assays using a spectrophotometer "PerkinElmer 650 UV / VIS Spectrophotomer", as shown in figure 51:
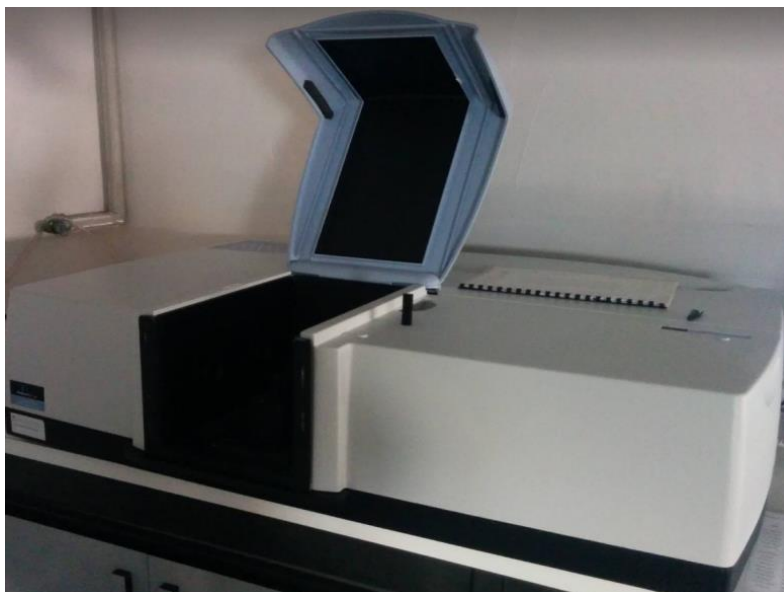
Figure 51: Spectrophotometer model's used for the assays, with the black cuvette on the right, used for the background

After the addition of graphite, all solutions were placed under constant stirring, at a speed of 400 RPM, for a total period of 23 days. Figure 52 shows the solutions thus obtained:
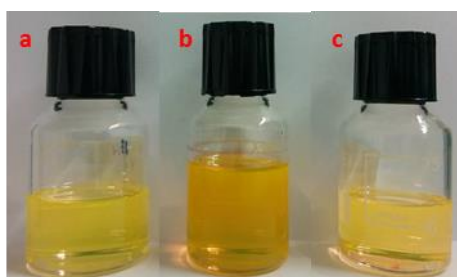
Figure 52: PDI + GF solutions, before stirring: a)PDI-H+ GF 3 mg ,b) PDI-F+ GF 3 mg c) PDI-Cl+ GF 3 mg

Every 24 h the solutions were stopped and left to rest for 30 minutes to allow the deposition of heavy particles of graphite. After passing these, 3 ml of the solution were taken, filtered and inserted into a quartz cuvette.

The spectrophotometer was set with the following parameters:

- Measure range: 350-600 nm
- Scan speed: 266,75 nm
- Data interval: 1,00 nm

- Slits: 2,00 nm

Prior to determining the absorbance values of the solutions containing the graphite, day after day, is performed the blank (or zero) before each measurements employing ,in this case chloroform, and scan in the measuring range.

This value will be used as a baseline, so with an absorbance value of 0; The counterpart has also done a measure of the maximum absorbance possible, this is done by inserting within the instrument a completely black cell, thus all the P0 intensity radiation is absorbed while the reflected part is 0 because the black body absorbs all radiation of the visible. Once these 2 absorbance values have been set, sample analyzes are carried out. The spectra thus recorded provide the actual absorbance of chloroform, as the signal derived from chloroform has already been removed during background recording. At the end of the recording of the spectra, the contents of the cuvette are reinserted inside the bottles containing the solution and subjected to another 24 hours of agitation to proceed until day 23.

3.2 Fluorescence assay

The fluorescence analysis were conducted with the same solutions employed in the case of UV-Vis microscopy. All employees solution were diluted with a dilution ratio of 1:10, and then were taken 0.2 mL of solution per day x to which were further 1.8 mL of solvent. The analyzes were conducted in a spectrophotometer "PERKIN ELMER Luminescence Spectroscopy LS 50 B" (figure 53).

Figure 53: Scheme of spectrofluorometer "PERKIN ELMER Luminescence Spectroscopy LS 50 B"

The dilution ratio was decided to avoid the phenomenon of "blinding" the phototube, ie the excessive arrival of photons at the phototube. The so prepared solutions were analyzed following the following parameters:

- Scan rate: 480-700 nm

- Excitation wavelength: 460 nm

- Excitation slit: 10 nm

- Emission slit : 10 nm

- Scan speed: 240 nm/min

The first measurement is made using only chloroform, in order to assess the zero emission of the solvent. Once the solvent was characterized, all the solutions containing the graphite were analyzed either with a quantity of 3 mg or with a quantity of graphite equal to 5 mg. All solutions were characterized by the above conditions for a total of 23 days. At the end of the analysis all the solutions have been deleted since they showed too low a concentration to be able to be inserted in the original solution.

3.3 BET surface area measure

Surface area measurements were carried out using the BET theory (Brunauer-Emmett-Teller), which aims to explain the physical adsorption of the gas molecules on a solid surface and then to determine the specific surface area of the samples. The analysis were carried out using an analyzer "ASAP (accelerated surface area and porosimetry) 2020 micromeritics" as shown in figure 54.

Figure 54: Scheme of "ASAP 2020 micromeritics"

Surface area measurements were carried out on samples of graphite flakes which had a different agitation time (0, 2, 4, 6, 8, 10, 12, 15, 18, 21, 24 days). These timings have been chosen to observe what happens to graphite at the end of kinetics, which occurs after 23 days. Graphite flakes are inserted into the solvent (chloroform), and a agitation at a speed of 400 RPM for the predetermined time is applied. At the end of the present time, the mixture was stopped and the solvent was removed using a rotavapor.

The resulting powders were transferred to the older ones (ampoules shown in Figure 4). To define the exact surface area value, the older ones were weighed before the addition and immediately after the addition from which it then goes back to the surface area value based on the inserted mass. Determined mass of the older sample is transferred to the degas unit, which performs a sample pretreatment. (In the left part of the image). The procedure used in the degas process is as follows:

1) Heating phase :

- Temperature ramp rate: 10°C/min
- Hold temperature: 300 °C
- Hold time: 60 °C

2) Evacuation phase:

- Temperature ramp rate: 10°C/min
- Target temperature: 60°C/min
- Evacuation rate: 6,7 mbar/s
- Vacuum set-point: 13 μbar
- Evacuation time: 10 min

Upon completion of the sample degas process, the older containing the samples are weighed to determine the mass variation that occurred during pretreatment. Generally, the variation in mass is due to the presence of moisture on the surface of the sample. Obtained the actual mass of the sample, the older are transferred into the measuring cell (right part of Figure 4), for surface area determination. During the analysis phase, different nitrogen pressures are applied to the sample, as required by the ISO standard that provides for these analyzes, furthermore, the rule states that the older is contained within a liquid nitrogen-containing cryostat at a temperature of -196 °C. The nitrogen pressures used are: 0.05; 0.1125; 0.1750; 0.2375; 0.3 (P/P^0). Each pressure value provides a surface area value, and then the automatic instrument performs an average of these 5 values to obtain the final surface area value.

3.4 Granulometer measure

The particle size measurements were carried out as complementary to the analysis of surface area measures, as with the BET surface area is obtained by the value, while with the granulometric measurements comes the size of the particles present in the compound to be analyzed. The analyzes were conducted using a "Saturn DigiSizer II, high definition digital particle size analyzer micromeritics" as shown in figure 55.

For the analyzes carried out on the granulator, the same powders used for surface area measurements were used. For the determination of the lateral dimension of the particles, which then is obtained the particle size of the sample, a small aliquot of sample (a few tens of mg) were collected and placed inside a small bottles containing fourty mL of isopropyl alcohol.

The solvent in this case is chosen according to the ISO norms specified in the determination of the powder granulometry. The suspensions thus obtained were used for the determination of the lateral dimension.

The operating conditions used for granulometric measurements are as follows:

- Flow enter rate: 9,0 L/min
- Obscuration: min: 10% max: 25%
- Circulate before data collection: 30s
- Data collection: start at beam angle: 0° , stop at beam angle: 25°
- Number of test: 2
- Sample material: graphite Density: 2,1 g/cm^3
- Analysis liquid: isopropanol: viscosity: 1,799 cP density: 0,777 g/cm^3 refractive index: 1,376

The solution so prepared are inserted into the measuring cell of the instrument (top right of figure 5), slowly reaching a beam obscuration value of up to about 10% (the light intensity adsorbed by the material is measured as obscuration and indicates the amount of sample added to the dispersant

liquid). Once this value is reached, the analysis starts where a laser starting at an angle of 0°, reaching an angle of 25°, hits the sample. The light scattering phenomenon that derives from the interaction of the particle with the beam gives an average particle size value to that exact angle value. After scanning all 25 °, the tool automatically provides a dimension distribution graph, which then returns to the percentile D_{10}, D_{50}, D_{90}. Tests are played back two times to test the reproducibility of the system.

3.5 TGA/DSC and ICP ANALYSIS

The thermo gravimetric analyzes were conducted to determine the behavior of molecules and graphite molecule interactions with the increase of graphite. For this purpose, thermal analyzes have been studied both in an oxidizing environment and in an inert environment. For TGA / DSC analyzes both pure molecules and the solutions of the molecules containing graphite were also analyzed. For samples of the sun molecules, an aliquot of the solid commercial product has been characterized directly using the instrumentation shown in figure 56:

Figure 56: Scheme of TGA (on the left) and DSC instrument (on the right)

TGA and DSC analyzes were conducted using the TGA: "TGA Q600 TA Instruments"; While for DSC: "DSC Q2000 TA Instruments". For the case of the molecules as well a quantity of between 10 and 20 mg of compound was collected and inserted into the cell sample holder, where it was previously inserted a heating rate, both in air and in nitrogen subsequently, equal to 15 °C / min.

During the heating phase, the gases produced by the decomposition of the molecules were also channeled into an infrared analyzer for the determination of the species that formed during the analysis. For this purpose, the infrared used is "IR Cary 600 Agilent" as shown in figure 57:
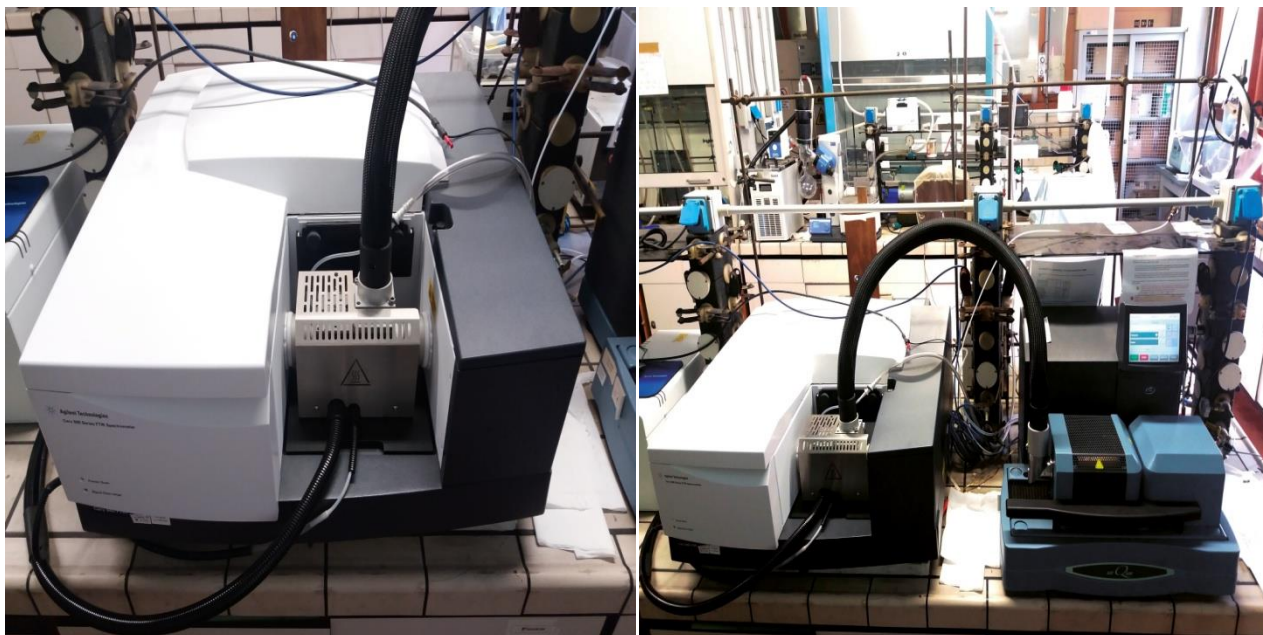
Figure 57: On the left "IR cary 600 Agilent", on the right TGA/IR combination

Once determined the mass variations and temperature profiles of the pure compounds, it is passed to the analysis graphite samples. To the solution containing the molecules was added a quantity of graphite equal to 3 mg /mL. All solutions were maintained under constant stirring at 400 RPM for a period of 23 days to compare quantitative data obtained by UV-VIS microscopy with those obtained by thermal analysis. At the end of the agitation period, the samples were filtered, on filter paper, and then transferred into vials for subsequent thermal determination. It was decided to use filtration with filter paper and not by rotating but to overcome the problem of the re-aggregation phenomenon due to lack of solvent. The ICP analysis was performed to verify the presence of metals and possible contaminants within the graphite commercial sample. For this purpose, before the measurement of the quantity of metals present inside were conducted of the calibration curves of the main metals such as: Mn, Mg, Fe, Ti, Zn, B, Pb, Th employing concentrations of these equal to 25 , 50, 100, 250, 500, 1000 PPM. Once the calibration line of these metals has been obtained, the sample is prepared as follows: the graphite sample is taken (0,1279 g) and inserted into a microwave reactor together with 5 ml of nitric acid conc. And 2 mL of water, the whole mixture is enclosed within the microwave (MW) reactor where it remains for 1 h at 220 ° C. After this period of time the sample is diluted with water in a ratio of 1:100 to obtain a mixture having a part per

million (PPM) in concentrations equal to 7.5763×10^{-5} (g/g) or 75.763 PPM. The thus prepared mixture was analyzed by ICP (inducted couple plasma) "OPTIMA 7000 DV optical emission spectroscopy Perkinelmer" as shown in figure 58:

Figure 58: ICP "OPTIMA 7000 DV optical emission spectroscopy Perkinelmer"

3.6 SEM and EDX measures

SEM measurements were performed to determine the morphology of the samples in the presence and absence of graphite. For this purpose the samples within the molecules, or both(molecules and graphite) were placed under constant stirring (400 RPM) for a variable duration (5 and 15 days respectively). At the end of the agitation period the solutions were taken, after waiting for 30 minutes for the precipitation of the larger particles, and by drop casting technique were deposited on a silicon oxide wafer.

The substrate cleaning is performed by using an ultrasonic bath according to the following procedure:

- 15 minutes inside a bath containing isopropyl alcohol
- 15 minutes inside a bath containing acetone

Between the first and the second wash the sample is dried with nitrogen to remove the possible contaminants remaining on the surface of the sample.

The thus obtained samples were used for the determination both morphological and atomic respectively using the SEM and the EDX analyzer (GEMINI ZEISS LEO 1530 microscope equipped with a Schottky emitter, figure 59.

Figure 59: "GEMINI ZEISS LEO 1530 microscope equipped with a Schottky emitter"

SEM images and XRD atomic analyzes were conducted using a beam power of 5 keV and a zoom from 1000 to 10000X.

3.7 AFM

The atomic force microscopy measurements were performed with a Digital Instruments AFM (Aura NT-MDT), using cantilevers in semicontact mode (Bruker RTESP tips, material: 1-10 Ω·cm phosphorus (n)- doped Si, $f_0 = 27–309$ kHz, k = 20–80 N/m;). Raw AFM data were treated by using histogram-flattening procedures. In figure10 is shown instrument employed:

Figure 60: Digital Instruments AFM "Aura NT-MDT"

All samples used for AFM characterization were deposited by drop-cast technique on a SiOx (Si/SiO$_2$) wafer and allowed to dry at room temperature prior to characterization. SiOx specimens prior to deposition were washed with the same methodology used for sample preparation for SEM analysis.

3.8 Fluorescence microscopy

Fluorescence microscopy measurements were conducted to determine what happens to chromophore when it interacts with graphite or not. For the determination of the variation of the fluorescence of the samples containing the graphite and the molecules, agitated for a variable period of time, have been deposited on a transparent support so as to allow the passage of visible light coming from the bottom or from the epifluorescence lamp where the light comes to the sample with an angle of 90 °. The transparent support used for the deposition of the solutions is the optical glass, previously washed with the same methods used for the cleaning of silicon wafers. The solution used to determine the fluorescence variation of the moles was agitated for a different time period of 5, 15 and 23 days to observe how the suspension varies with time. For the observation, 100 μL of these solutions were taken and deposited on a glass support by drop casting. The thus prepared samples were inserted into the port of the microscope slides, and then the images are being recorded both using the visible light, coming from an incandescent lamp, either from a light coming from a lamp in which mercury vapor It provides a light in the ultraviolet spectrum. Samples were displayed using different zoom of the target port (10X to 40X) as well as the eyepieces (5X). In order to determine the interaction between the epifluorescence light source and the sample, filters were used

to select specific wavelengths. Figure 61 shows the instrumentation used for fluorescence microscopy.

Figure 61: Fluorescence microscopy set

As seen from the previous figure, the image recording device (Nikon digital sight DS-U1) on the left side of the screen is located, the optical microscope (Nikon eclipse 80 i) in the middle and on the right is the presence Of the epifluorescence lamp (super high mercury lamp power supply). The filters used were placed between the slide door and the eyepiece of the microscope. In the case of fluorescence microscopy, a monochromatic filter has been used to select only a narrow range of wavelengths, shown in figure 62.

Figure 62: "Violet" filter

The filter used, called "wide blue", allows to select a range of excitation wavelengths (coming from a mercury vapor lamp) of 455 ± 35 nm, which means that the excitation filter passes all the lengths d Then included in the 420-490 nm range. Once "filtered" the light, this is collimated on the sample

through a dichroic mirror. The sample hit by the light emits in turn and this light is collimated in a high pass filter that "cuts" all wavelengths below 515 nm, this filter is fired to collect more light to red. A second type of filter was also used, called "violet" used to collect a larger amount of radiation towards the blue, which has the following characteristics: λ_{exc} = 385-425nm $\lambda_{collect}$ = 455, ie with this filter cut all the frequencies those are cut a wavelength below 455 nm. In figure 63 shows the diagrams of the instrumentation used:
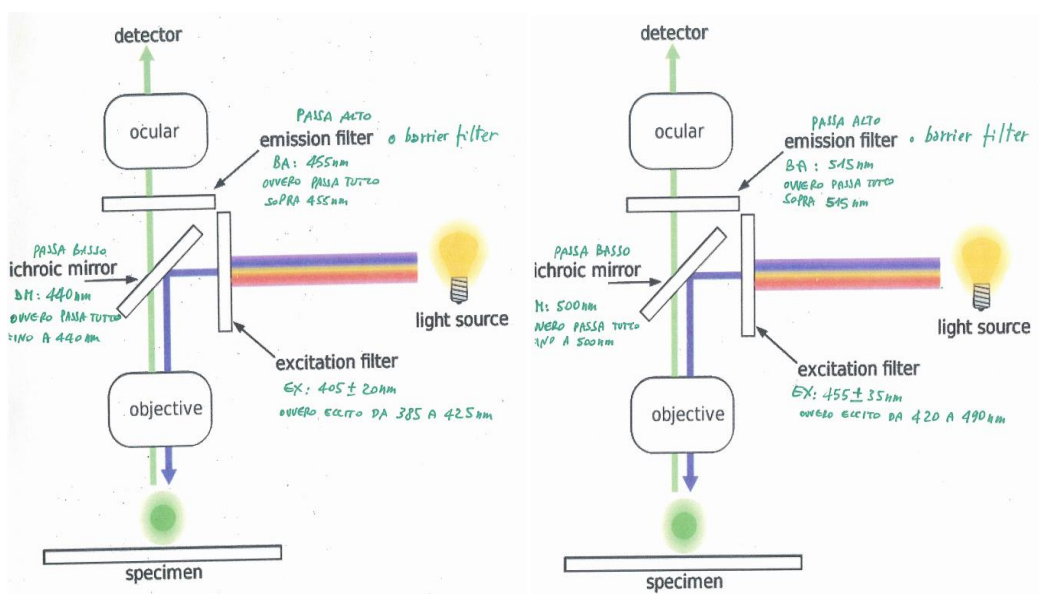
Figure 63: Scheme of filter used for fluorescence microscopy

3.9 XRD measure

X-ray analyzes were conducted to verify the crystallinity of molecules, and molecules when interacting with graphite. The XRD measurements were performed on the 3 powders of pure molecules and later on of the molecules with the graphite powders. The powders that have been employed for the XRD analysis are the same that have been employed for the thermal characterization or even PDI + GF agitated for 5 and 15 days, respectively, and then filtered on filter paper to prevent re-aggregation. XRD analyzes were characterized using the following parameters:

- Start angle: 3 (2θ)
- End angle: 35 (2θ)
- Step size: 0,0501 (2θ)
- Time x step: 50 s
- Slits: ½ °

Figure 14 shows the schema of the instrument used " X port PRO, PANanalytical:
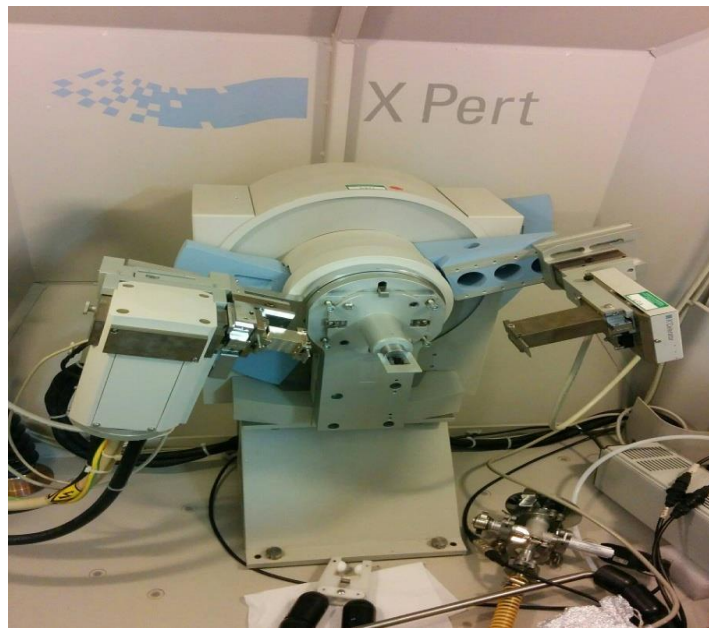
Figure 64: XRD "X port PRO, PANanalytical" scheme

From the figure 64 it was seen in the left part of the radiogenic part where the X-ray beam is collimated and passed through the slots where it is then collimated on the sample, is observed on the right side instead of the instrument detector. The radiogenic part is provided with a motor that allows movement of this according to the previously fixed angles 2θ.Once characterized the pure samples free from graphite, it was decided to carry out the tests in temperatures only for the PDI-Cl, which presents a particular behavior in TGA. Figure 65 shows a diagram of the instrument where the temperature tester was inserted:

Figure 65: XRD Sample holder's for temperature measurements

Chapter IV – RESULTS

The purpose of this work is to study the interaction of small aromatic compounds (perylene diimide such as PDI-H, PDI-F, and PDI-Cl) with a graphitic substrate. By using a rather simplified description of the exfoliation process, small aromatic molecules, like these, are often described as aromatic surfactants. It is well-known that the hydrophobic nature of graphitic materials coupled with the relatively stable inter- layer adhesion of graphite make it difficult to directly exfoliate graphene in water. These compounds are considered as "molecular wedges" with the apolar, aromatic part interacting with graphene through π-π stacking and the negatively charged part favouring sheet stabilization in solvents and hindering re-aggregation.[1] The efficiency of amphiphilic perylenes to interact with graphene has been attributed to their aromatic nature and to their electron donating/withdrawing character due to the difference in the dyes' electronegativity with respect to graphene.[2] The final efficiency of graphite exfoliation with small aromatic dyes depends not only on the thermodynamics of exfoliation, but also on the presence of local energy minima, which will influence kinetics. Other factories that influence the kinetics are the interaction between solvent-molecule, graphene-molecule and graphene-solvent. and on the solvent–molecule, graphene–molecule and graphene–solvent competitive interactions. The affinity of the dyes towards graphitic substrates and their efficiency in exfoliating and suspending graphene were studied using optical absorption and other technique.[2] The extraordinary optical and chemical properties of these molecules such as their well-defined absorption and emission in the visible spectrum, tuneable absorption, emission, make them interesting materials to be combined with graphene. Shown below the molecules tested for this scope
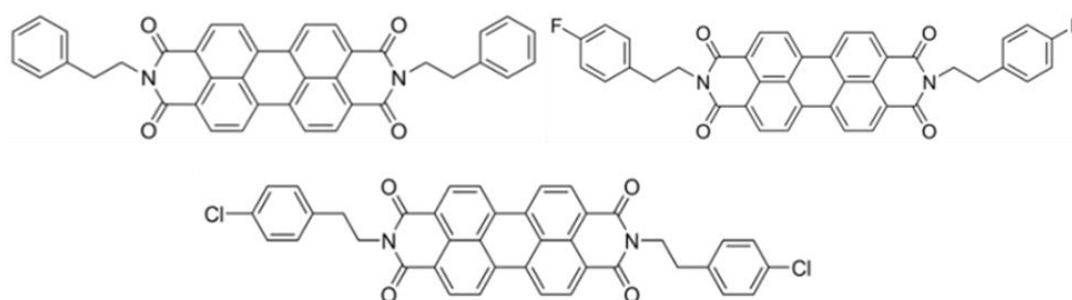
Figure 66: Different compounds of perylene diimide family (PDI-H, PDI-Cl, and PDI-F, respectively)

4.1 Spectrophotometer analysis

The absorption spectroscopy was used because it shows that the fragmentation yield, when it put, on the solution, a little amount of graphite powder, leaves to decrease in absorbance, because the dye's interact with graphite and consequently the amount of free dye in solution is less. The first step were obtained UV-VIS spectra, without graphite, in order to understand the "fingerprinted" of these molecules, and only in the second step it be add the graphite powder (flakes) which can be studied the dye's capturing phenomena. The interaction between PDI and graphite substrate can be observed by spectrophotometric techniques, which determine the absorption spectrum in the visible range (350-600nm).The studied it be focused of the interactions in different types of solvents in which the compounds are dissolved, in order to demonstrate that changing the solvent leads to a shift of the absorption peaks and the absorbance values. As is well known in literature the best solvents that solubilize these molecules are halogenated solvents or solvents having an aromatic nucleus and therefore, thanks to their greater interaction, they can solubilize such compounds more efficiently.The solutions were prepared at same starting concentration of 0,1 mg/ml in different solvents (CHCl3 and THF). The concentration of 0.1 mg/mL was employed and used by measurements carried out previously in the same laboratory. Note the molecular weights of the molecules employed (see table 3) and the value of the final concentration, below are reported the calculation for each sample.

Table 3: Physical chemical characteristics of the molecules employed

Molecules	CAS Number	Molecular Weight (g/mol)
PDI-H	67075-37-0	598.65
PDI-F	215726-57-1	634.63
PDI-Cl	215726-51-5	667.54

$$PDI - H = \frac{0.1mg}{ml} * 50mL * \frac{1g}{1000mg} * \frac{1mol}{598.65g} = 8.352 \ 10^{-6} mol$$
$$= 8.352 * 10\wedge(-6) \ mol * \ 598.65 g/mol = 0.005 \ g$$

$$PDI - F = \frac{0.1mg}{ml} * 50mL * \frac{1g}{1000mg} * \frac{1mol}{634.63g} = 7.879 \ 10^{-6} \ mol$$
$$= 7.879 * 10\wedge(-6) \ mol * \ 634.63 g/mol = 0.005 \ g$$

$$PDI - Cl = \frac{0.1mg}{ml} * 50mL * \frac{1g}{1000mg} * \frac{1mol}{667.54g} = 7.492 \ 10^{-6} \ mol$$
$$= 7.492 * 10\wedge(-6) \ mol * \ 667.54 g/mol = 0.005 \ g$$

The real weight (mg) of each sample, dissolved into different solvents, are listed below (table 4):

Table 4: Amount of substance weighed for each compound in two different solvent.

	PDI-H	PDI-F	PDI-Cl
THF	4.84 mg	4.94 mg	5.15 mg
CHCl$_3$	5.12mg	5.16 mg	5.12 mg

Once obtained the solution for each PDI, the spectrophotometric measurements were perform in order to determine the number of peaks and the relative wavelengths of the maximum. Before making spectrophotometric measurements of real samples we need to make an auto calibration of the instrument using the blank solvent (without the addition of PDI): a cuvette containing only the solvent without the analyte, was inserted on spectrophotometer, then the UV-VIS spectra was recorded. Once obtained the blank spectra, this may be used as base line, which later will be automatically subtracted from measurements of real sample, to obtain the true/real absorbance of the single analyte Shown below are the spectra UV-VIS.
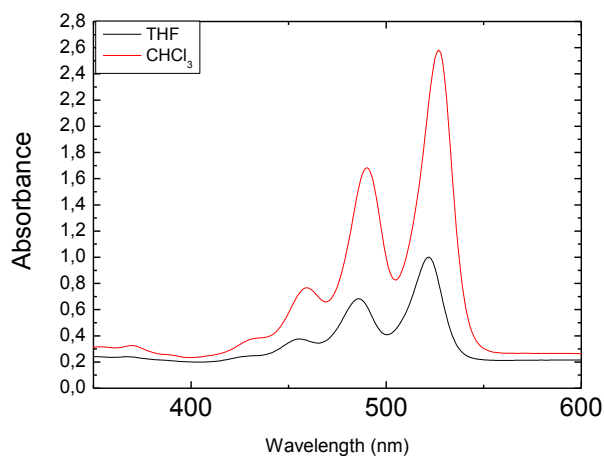
Figure 67: UV/VIS absorption spectra of PDI-H in both solvent
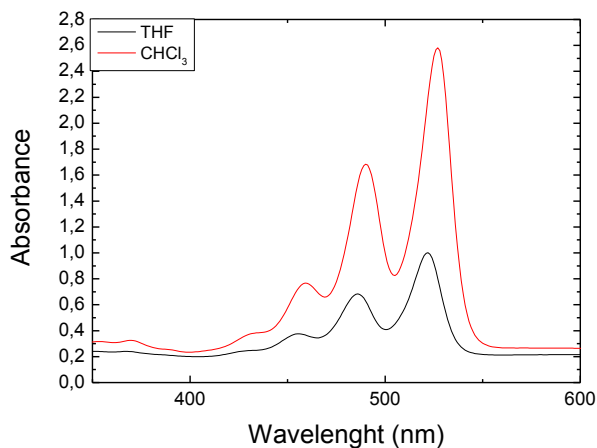
Figure 68: UV/VIS absorption spectra of PDI-F in both solvent
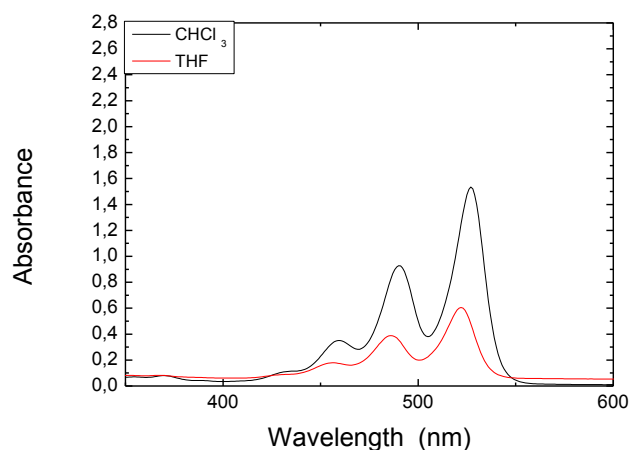
Figure 69: UV/VIS absorption spectra of PDI-Cl in both solvent

Figures 67-69 shown the absorption spectra's of the three compounds in two the different solvents. The main difference of these spectra consist in the changing of the absorbance value when these compounds solubilize in different solvents. This indicates that although the molecules with different substituents, the resulting spectra are super imposable, indicating that the contribution of the substituent is not comparable respect to the central pyrenic chromophore. The pictures show a higher solubility in chloroform, and this leads to greater absorbance value, because the amount of the molecules dissolved in chloroform is higher.Since the excessively high absorbance values (beer's law is not respected by absorbance values greater than 1), it was decided to dilute the solutions that have an absorbance value in the range in which this law is valid (0.05-1). The next steps will be to dilute the mother solution three times and repeat the experiment UV-VIS spectra. It was initially decided to dilute the solution with a 1:3 ratio. These solutions were prepared by taking five mL of mother solutions of each sample and diluting with further 10 mL of solvent, in which

these samples are previously dissolved. After obtaining these new six solution, it was performed the spectrophotometric tests, in the same range were used in previous samples (350-600nm). They have been made in three measurements, for each samples, in order to demonstrate the reproducibility of the measurements. Shown below are the overlapping absorption spectra of various samples, dissolved in different solvent.
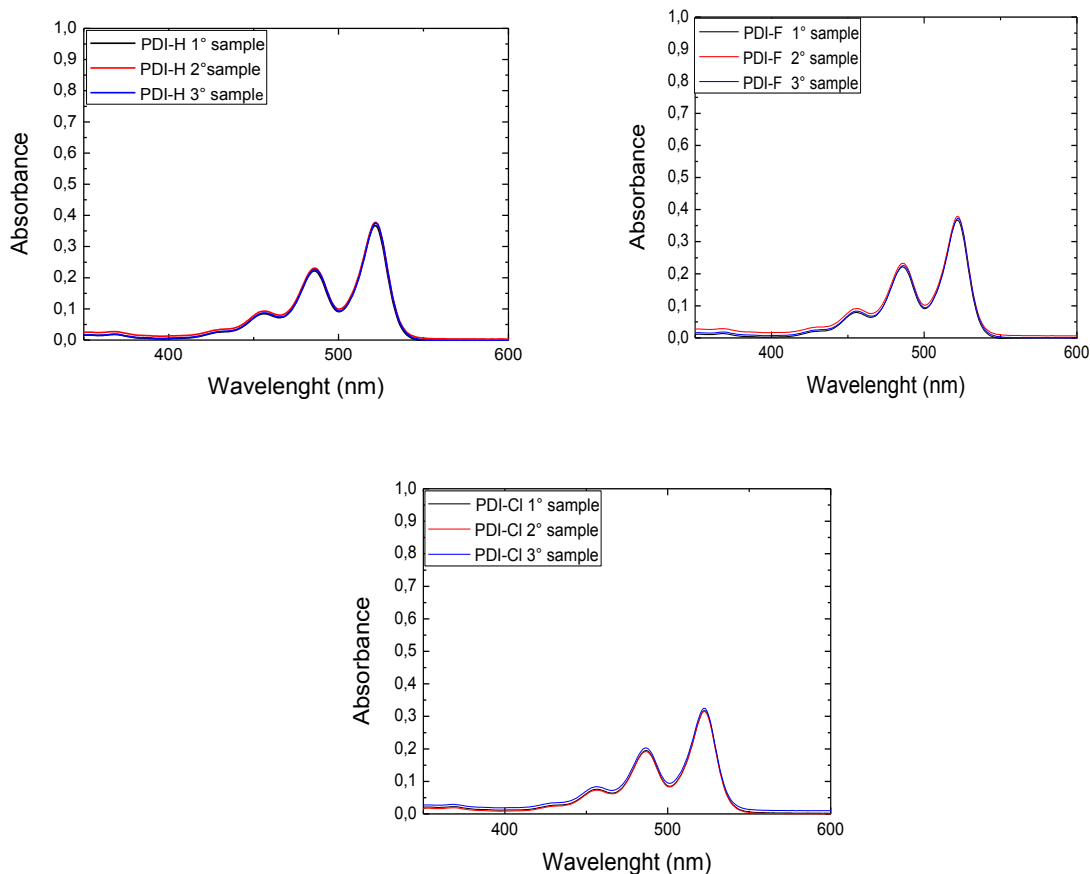
Figure 70: Absorption spectra's of each PDI (PDI-H, PDI-F, PDI-Cl) diluted with, 1:3 ratio, in THF
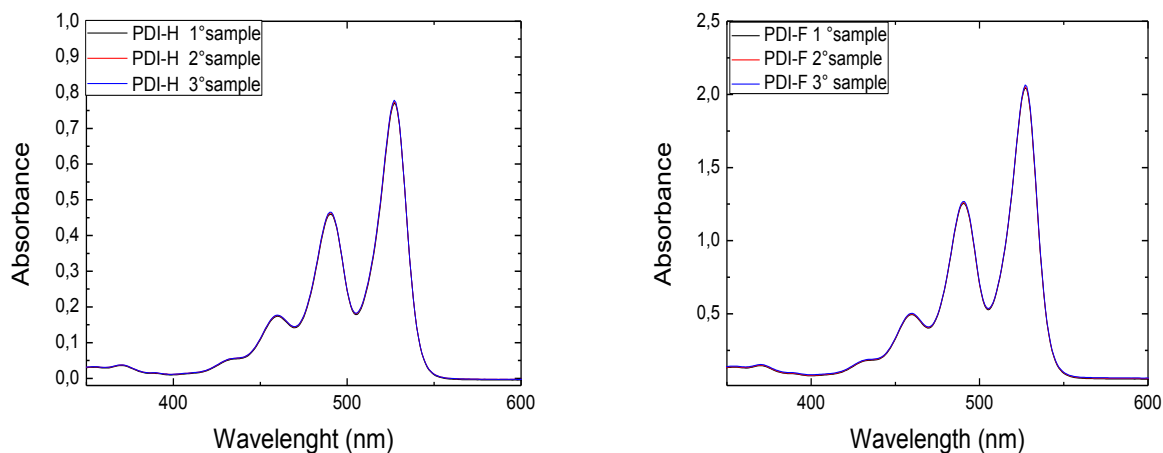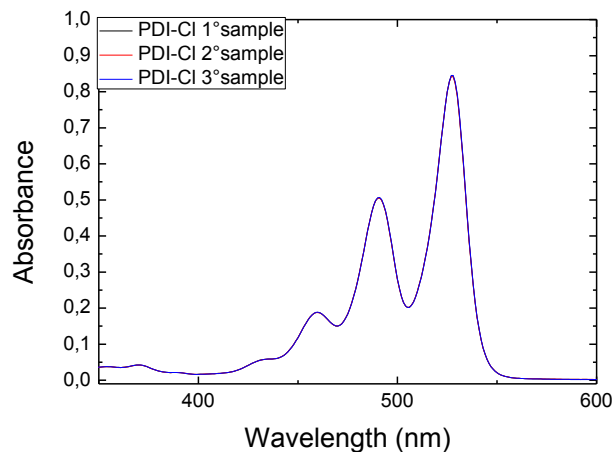
Figure 71: UV/VIS absorption spectra's of each PDI diluted, with 1:3 ratio, in chloroform

Since as noted, in the graphs, the solubility of the molecules is greater in chloroform compared in THF, since the absorbance values are higher. For this reason, it was decided, to dissolve the molecules only in CHCl3. From the previous tests, was found out that we are close to saturation of the molecules in CHCl$_3$, although the dilution had been reduced by 1/3 the absorbance value before and after the dilution was similar, for this reason it was decided to work with a lower concentration of molecules in solution, to avoid problems caused by solid precipitation. This problem was due to the concentration value superior to the solubility limit, so the starting mother solution was diluted with a 1/5 ratio, in order to have a molarity (M = m / (M.W. × V)) equal to 5 mM. Obtained these new solutions, in the two solvents previously selected, spectrophotometric assays were again performed. Shown below the spectra's of each molecules at the same concentration dissolved in chloroform and tetrahydrofuran (figure 72):
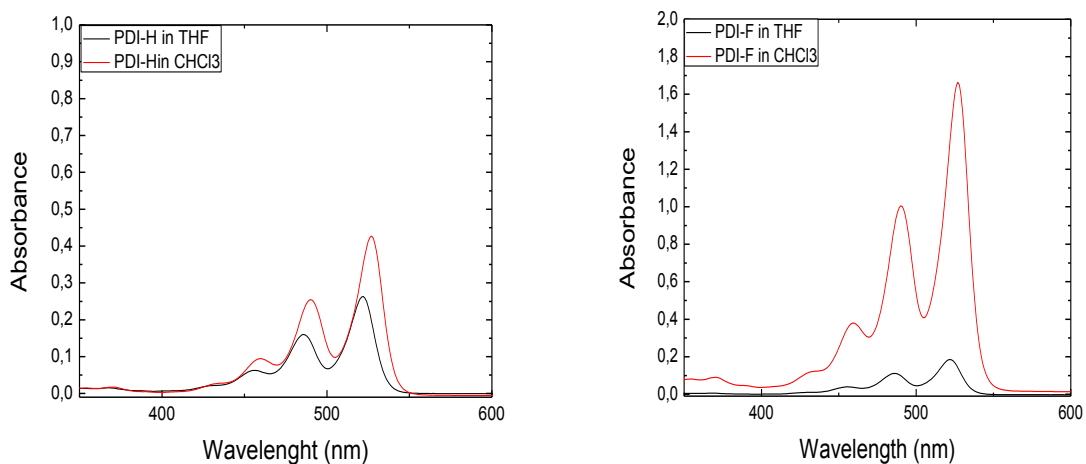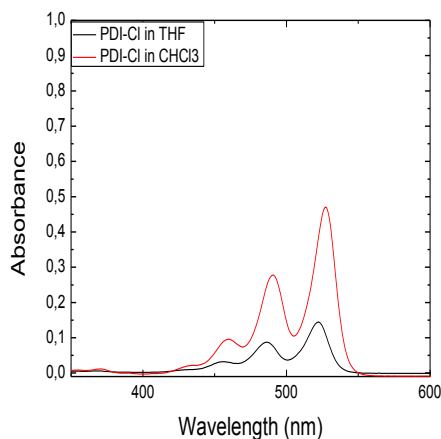
Figure 72: UV-VIS Spectra's with 1/5 dilution ration in both solvents

As can be seen by further increasing by dilution, from 1/3 to 1/5, the variation in absorbance is not change a lot. For this reason, the solutions were further diluted to reach a concentration of 1,125 * 10^{-5} M. This value was obtained by subjecting the solution to progressive dilutions until solid solubilization has taken place. Due to the lower solubility of these compounds in THF, it was decided to use the only chlorinated solvent for all subsequent tests. For this reason the 3 solutions were prepared again, using the weights reported following:

$$PDI\text{-}H = 1.125 * 10^{-5} \text{ (mol/L)} * 0.4 \text{ (L)} * 598.65 \text{(g/mol)} = 2.69 \text{ mg}$$

$$PDI\text{-}F = 1.125 * 10^{-5} \text{ (mol/L)} * 0.4 \text{ (L)} * 634.64 \text{(g/mol)} = 2.85 \text{ mg}$$

$$PDI\text{-}Cl = 1.125 * 10^{-5} \text{(mol/L)} * 0.4 \text{ (L)} * 667.54 \text{(g/mol)} = 3.00 \text{ mg}$$

From these 3 new mothers solutions we were obtained the new spectra, as shown below:
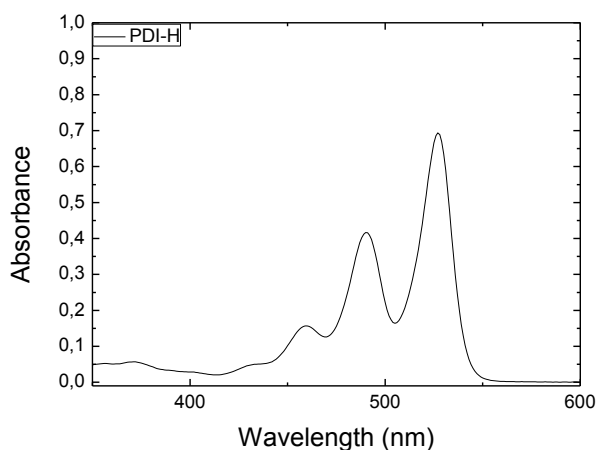
Figure 73: UV/VIS absorption spectra of the new mother solution of PDI-H
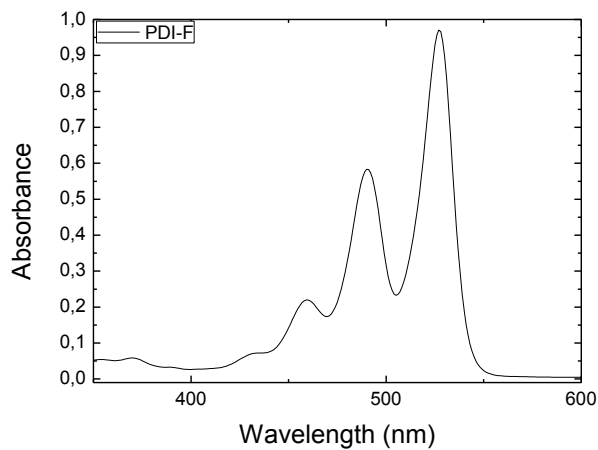
Figure 74: UV/VIS absorption spectra of the new mother solution of PDI-F
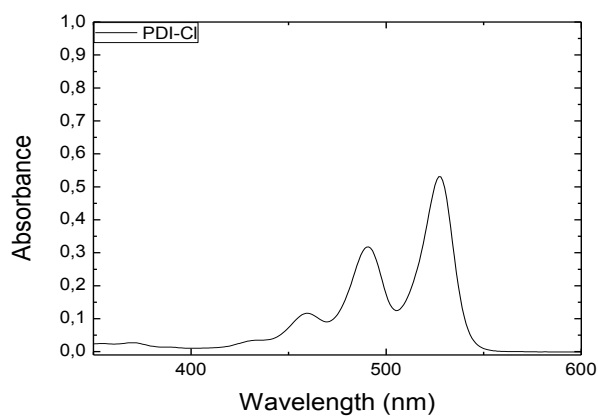
Figure 75:UV/VIS absorption spectra of the new mother solution of PDI-Cl

In this case, other tests were not carried out for reproducibility because in the previous tests it was observed that this property is respected. In order to verify the validity of Beer's law, for the three molecules, were recorded different absorption spectra at different dilution ratios, respectively: 1/2, 1/3,1/4, 1/5, 1/10, 1/15. Below shows the graphs obtained (figure 76-78).
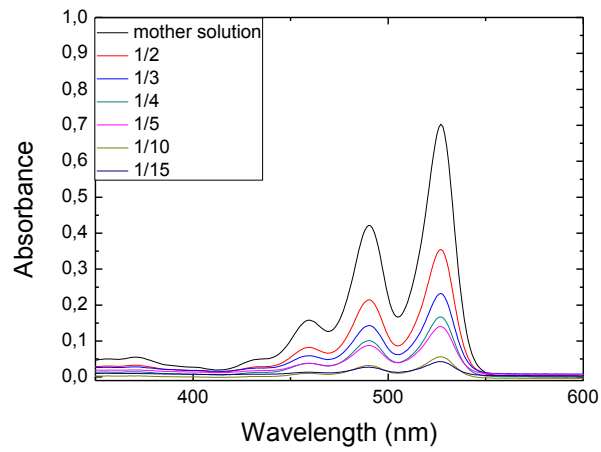
Figure 76: UV-VIS spectra's of PDI-H with different dilution ratio
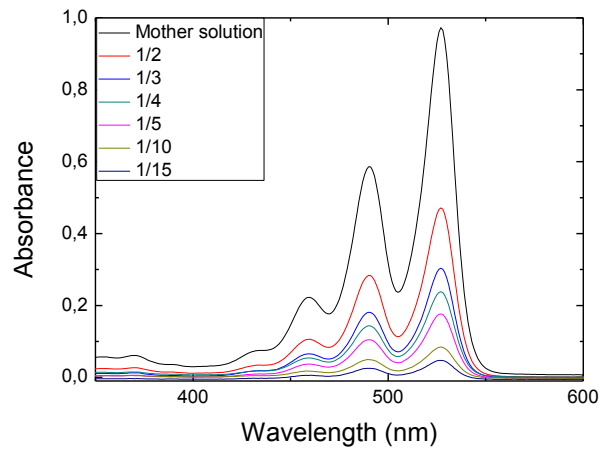
Figure 77: UV-VIS spectra's of PDI-F with different dilution ratio
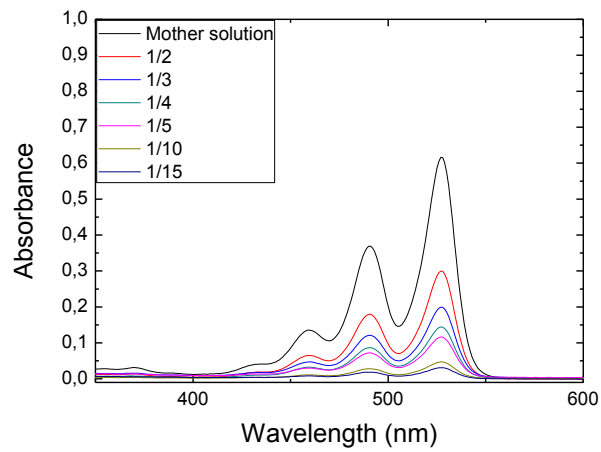
Figure 78: UV-VIS spectra's of PDI-Cl with different dilution ratio

The calibration lines 79-81 are shown below. Once registered the spectra at various concentrations, we proceeded to the validity of Beer's law occurs, considering the peak absorbance value at 527 nm and plotting this value to the value of the concentration.
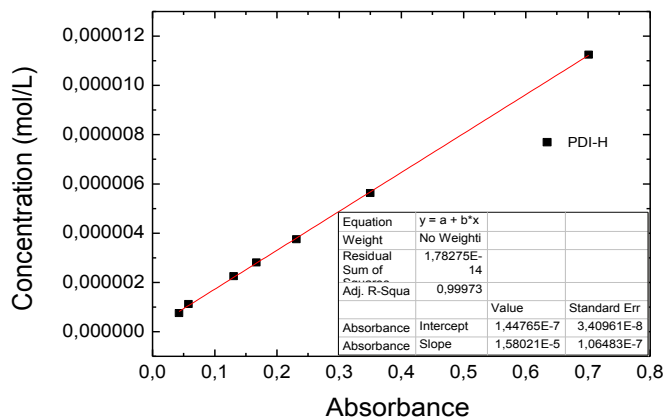
Figure 79: Linear fit of PDI-H at different concentration
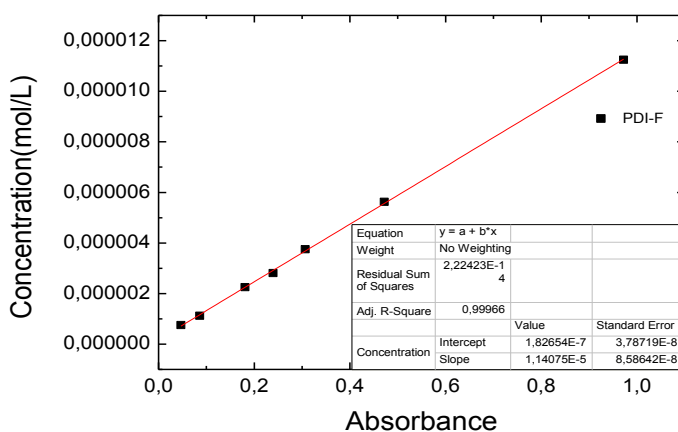
Figure 80: Linear fit of PDI-F at different concentration
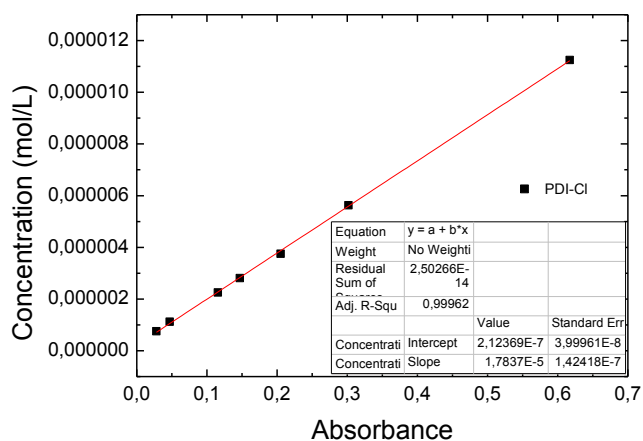
Figure 81: Linear fit of PDI-Cl at different concentration

Once verified the validity of Beer's law (A= ε*b*c , where A is the absorbance, b is the pathlength (cm) and c is the concentration (mol/L)), it be proceeded to the calculation of the value of the molar extinction coefficient (Ɛ). The absorbance value it has been used considered a specific wavelength of maximum at 527 nm. The following table (table 5) shows the average values obtained:

Table 5: Molar attenuation coefficient's of PDI

Molecules	Average of molar attenuation coefficient (ε) (L/mol cm)
PDI-H	58783.49
PDI-F	79489.52
PDI-Cl	74774.25

Once the validity of Beer's law, he began to study the interaction that exists between the dye molecules with carbon materials. This process is called Dye's capturing. A natural approach to exfoliate graphene is to use surfactants based on nano-graphenes (NGs), i.e., small polyaromatic hydrocarbons such as pyrenes, perylenes, coronenes, tetracenes, etc. These conjugated moieties exhibit a polyaromatic structure similar yet smaller, to that of graphene, and are self-assemble on its surface forming ordered layers, at least in ultra-high vacuum conditions. While the efficiency of pyrene derivatives in exfoliating graphene is well known, the exact details of pyrene-graphene interactions, and more Generally of NG-graphene interactions, are still unclear. The efficiency of amphiphilic pyrenes to interact with graphene Has Been Attributed to Their aromatic nature and to Their electron donating / withdrawing character two to the difference in the dyes' electronegativity with respect to graphene.[3] The effect of the dye's capturing was monitored every 24 hours by recording a spectrum of absorbance, and observing the decrease in absorbance. The decrease is due to the interaction of dye molecules (PDI) with graphite flakes. This interaction leads to a decrease in the number of free molecules in solution and consequently a decrease in absorbance.

DYE CAPTURE ON GRAPHITE POWDER
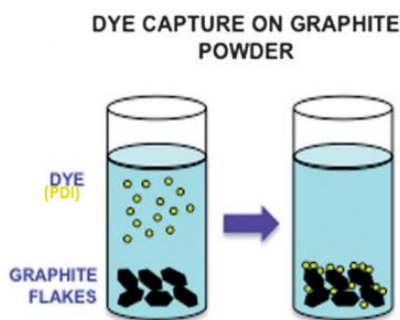
Figure 82: Dye's capture mechanism

The tests were conducted only in chloroform, given the greater solubility of the dye's. In any kinetics are studied three different solutions: one containing only the molecule, another consists of the stock solution and the graphite flakes, and finally the last are placed only $CHCl_3$ with graphite flakes. The first solution, containing only the PDI, is designed to evaluate a possible change in absorbance of the original solution. The solution that containing only chloroform and graphite flakes is studied: 1) to observe a possible variation of the signal due to the fragmentation of the flakes, as a result of stirring 2) the absorbance value which is obtained serves of the background signal which will be removed from the signal of the solution that containing graphite and the dye, in order to obtain only the signal arising from the analyte. Stirring was applied to avoid artefacts due to diffusion limits; samples were stirred for different days to ensure efficient adsorption. In the absence of sonication, the exfoliation does not take place, although the molecules having a higher affinity for graphite may initiate their adsorption process on the surface of the graphite powder. Therefore, the graphite powder acts as a trap for the molecules in solution, thereby capturing the dyes from the solution. The amount of this "dye's capture" process was calculated by simply observing the decrease in optical absorption intensity upon exposure time. As expected, stirring without graphite does not change the original absorption spectrum of the dyes; conversely, in the presence of graphite spontaneous adsorption from solution to the graphitic surface is observed. The fraction of molecules adsorbed on graphite has been calculated by monitoring the change in the maximum absorption peak for each molecule (at 527 nm).The dye capture phenomenon was analysed by studying the kinetics of absorption of the molecules tested in function of time. The study is conduct by adding a predetermined amount of graphite flakes, equal to 3 mg/mL, on a different mother solution (PDI-H, PDI-F, and PDI-Cl).
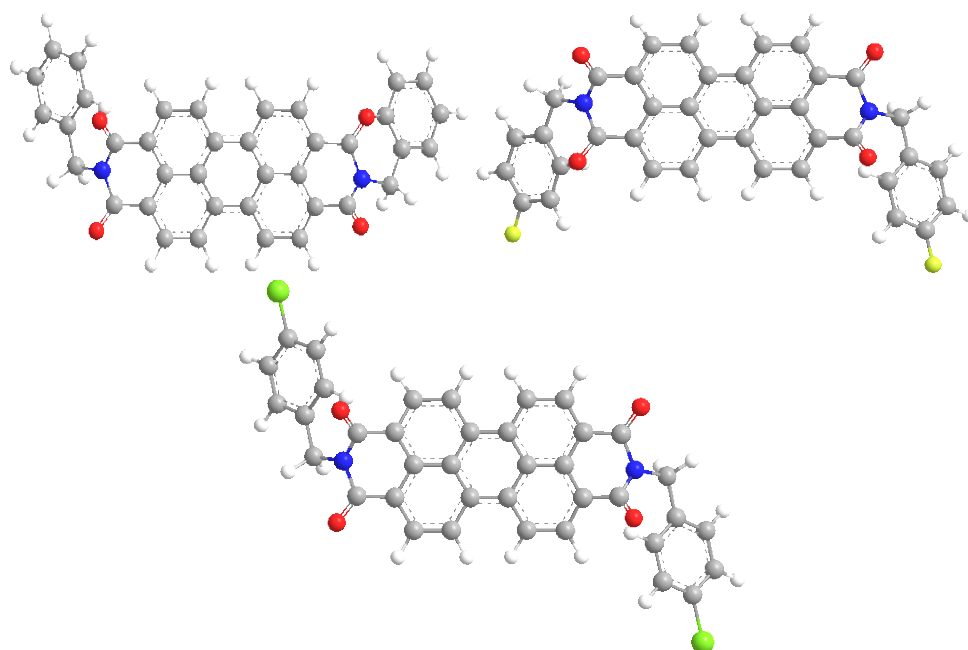
Since these structures are able to determine, theoretically, the size of the molecules employed, in table 6 are reported the values obtained:

Table 6: Theoretically distance in perylene dimmide

Molecules	Distance between H-H pyrene core ($°A$)	Distance between X-X heteroatoms ($°A$)
PDI-H	6.538	H-H = 14.790
PDI-F	6.538	F-F = 15.468
PDI-Cl	6.538	Cl-Cl = 19.547

The reason for which it was decided to use an initial amount of graphite of 3 mg is due to the fact that it assumes a graphite surface area of $5m^2/g$ and to have a graphite concentration of 3mg / mL, from calculations which follow, it can be seen that the amount of graphite used is sufficient to interact all PDI molecules with graphite. Calculations are given, considering a total volume of 30 ml of mother solution in which 90 mg of graphite flakes (GF) are added:

$$molecules\ in\ a\ liter = 6.022 * 10^{23} \left(\frac{molecule}{mol}\right) * 1.125 * 10^{-5} \left(\frac{mol}{L}\right)$$

$$= 6.78 * 10^{18} molecule/L$$

$$molecules\ in\ 3\ mL(cuvette\ volume) =$$

$$6.78 * 10^{18} \left(\frac{molecule}{L}\right) * 0.003L = 2.034 * 10^{16} molecule$$

$$surface\ area\ of\ graphite = 5\frac{m^2}{g} * 0.09\ g = 0.045\ m^{\wedge}2 = 4.5 * 10^{16} nm^2$$

$$area\ for\ each\ molecule = 4.5 * 10^{16} nm^2 * 2.034 * 10^{16} molecule = 2.0651 \frac{nm^2}{molecules}$$

As can be seen from the previous calculations, the amount of graphite inserted is sufficient for practically all the molecules to attach, by interaction π-π, to graphite. The three solutions so obtained, are placed under stirring 24/24 h. The stirring of the solution is stopped 30 minutes before analysis, to allow the graphite particles suspended to settle to the bottom of the bottles. The analyses were performed every 24 h in the same range as previously used (350-600 nm). Shown below are the spectra's records for the three molecules versus time (figure 84-86):
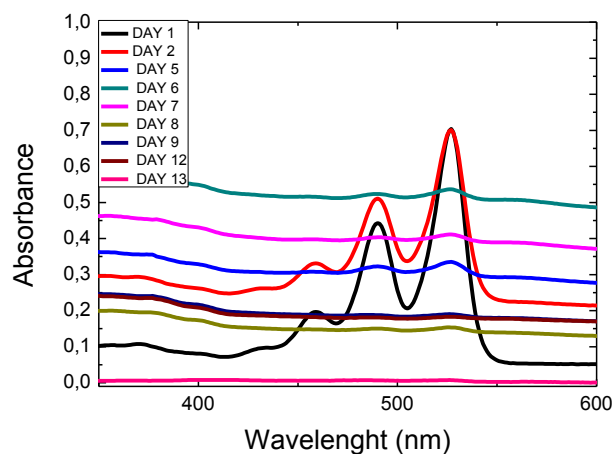
Figure 84: Adsorption kinetic of PDI-H + GF
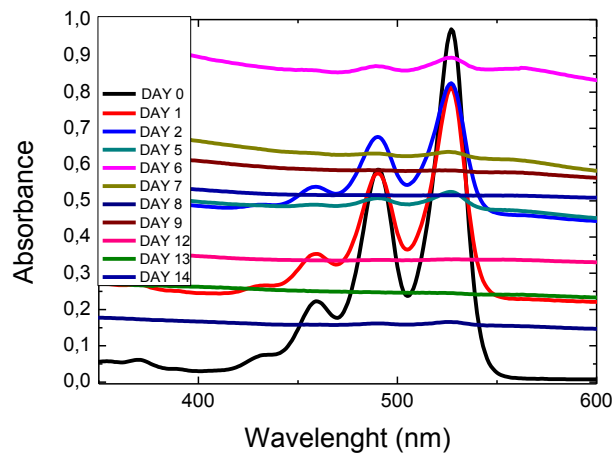
Figure 85: Adsorption kinetic of PDI-F
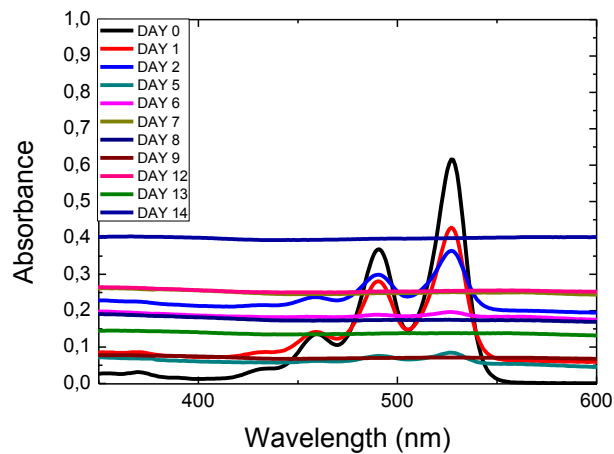
Figure 86: Adsorption kinetic of PDI-Cl

An important factor to note is the irregularities of the baseline; such a deviation of zero is due to the presence of suspended particles within the solutions. These particles cause light scattering, precisely due to the interaction of electromagnetic radiation with the particle, this scattering is more and more intense with the passing of time, in fact the magnetic stirring breaks the graphite flakes making them smaller and hardly to remove, and this cause a great light scattering phenomena . In order to avoid the presence of light scattering it was decided to remove these suspended particles, employing two separation techniques: filtration and centrifugation. The filtration was conducted using filters of PTFE (polytetrafluoroethylene) with a pore diameter equal to 0.45μm. The centrifugation was conducted by employing the PTFE tube in which is inserted the solution and placed inside the centrifuge with the following parameters: rotation speed: 20000 rpm; rotation time: 15 minutes. The temperature was set at 3 °C, to limit the evaporation of the solvent. Once removed the graphite

particles, the clear solution was analyzed, and the absorption spectra was record. Show below the absorption spectra of PDI-Cl solutions thus obtained

.
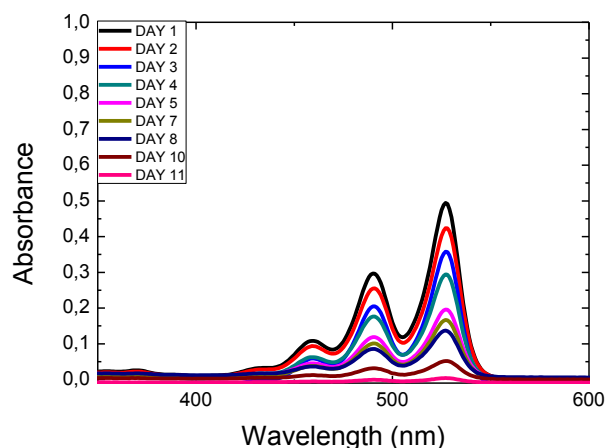
Figure 87: Kinetic of PDI-Cl + GF after filtration step
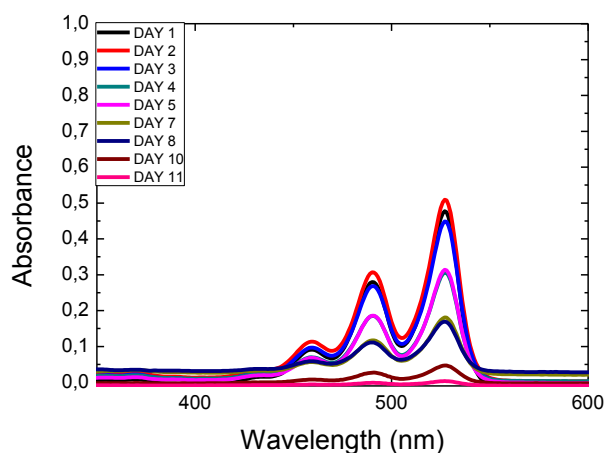
Figure 88: Kinetic of PDI-Cl + GF after centrifuge step

Since as can be noted by the separation methods, the base line, that are obtained, are always approximately equal to zero, index that does not have more the light scattering phenomena. Both method gave a good results, but for different reason (principally time) it be choose the filtration separation, because gave the best performance in less time. For this reason, all subsequent tests will be filtered to avoid the presence of suspended particles, and then the light scattering phenomenon.

Solved the problem to due by light scattering it be focused on the control of temperature and stirring speed of the solution, as they have encountered problems of reproducibility of the different kinetics.

The following is a comparison of two consecutive kinetics. In figure 89, are reported the absorbance value at 527 nm (maximum) respect time:
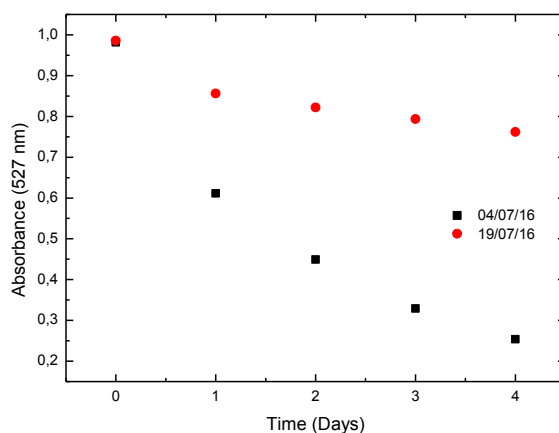
Figure 89: comparison between two PDI-Cl kinetics

Since as can be noted between the first kinetic and the next there is a considerable difference in terms of absorbance changes as a function of time, for this reason it was decided to maintain the solution always at the same temperature (21 ± 1 °C), to order to avoid possible variations of the adsorption speed due to temperature. Along with the temperature, adjustment was done by using two identical magnetic plates, so you always have the same parameters and the same performance. Set these two parameters, we have been conducted of new kinetics in order to demonstrate an increase of the reproducibility of the measurements. The following are the kinetics of adsorption of the PDI-Cl solution in the presence of graphite flakes (3 mg /mL)
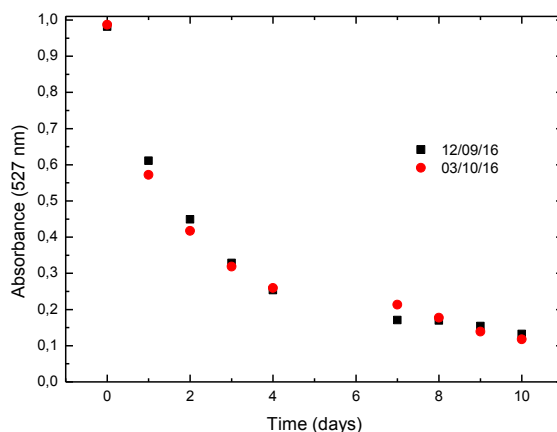
Figure 90: Comparison between two PDI-Cl kinetics after fixed temperature and speed

Verified the reproducibility of the measurements were carried out the kinetics of adsorption even for the other perylene dimmide (PDI-H, PFI-F), maintaining the amount of graphite flakes fixed at 3mg/mL (figure 91-93).
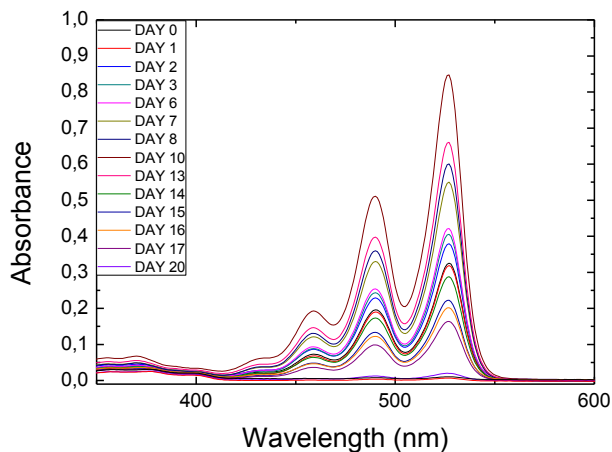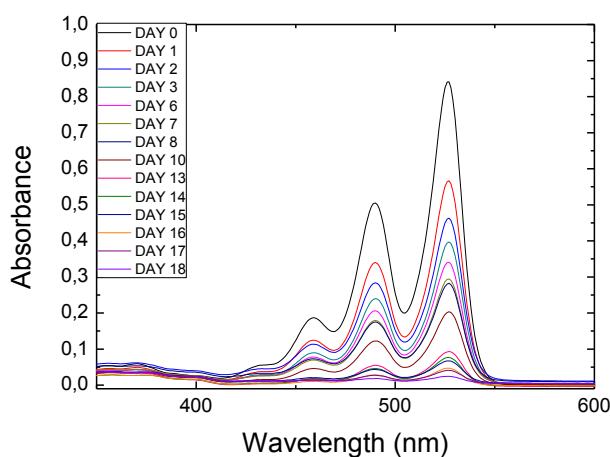

Figure 91: kinetic of PDI-H + GF 3 mg/mL
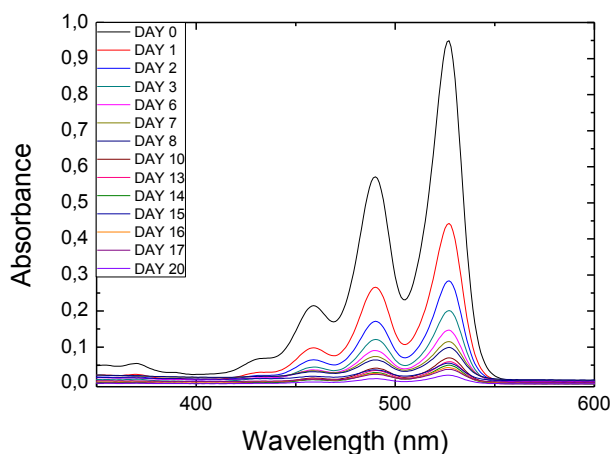

Figure 92: kinetic of PDI-F + GF 3 mg/mL

From the graphs shown above is found as the kinetics of the PDI-F adsorption is faster compared to those of the PDI-H and PDI-Cl. To make it clearer that the decrease in quantities of free molecules in solution and then the absorbance was plotted the maximum absorption (527 nm) vs. time.
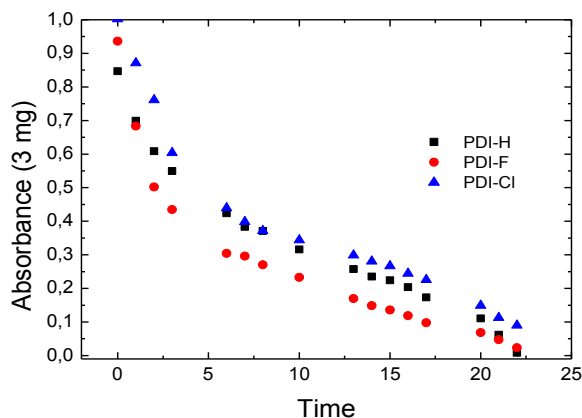
Figure 93: Comparison of PDI's kinetics

 From the figure it is observed as the speed of adsorption of perylene diimide that contain chlorine or hydrogen are very similar. Determine the speed of the kinetics carried out with 3 mg of graphite, it is proceeded to perturb the system by adding an upper quantity of graphite flakes, equal to 5 mg / mL, and subsequently recording the absorption spectra. It was decided to increase the concentration of graphite, since from the previous kinetics it has been found that despite the achievement of the predetermined 23 days, there are still free PDI molecules in solution, and therefore the amount has been increased to 5 mg / ml. By inserting a quantity of graphite, the area available to the molecules increases from 2.21 nm^2/molecule to 2.98 nm^2 /molecule, assuming always a surface area of 5 m^2/g. All solutions were tested in the same conditions used previously (350-600nm).

Figure 94: Kinetic of PDI-H + GF 5 mg/mL
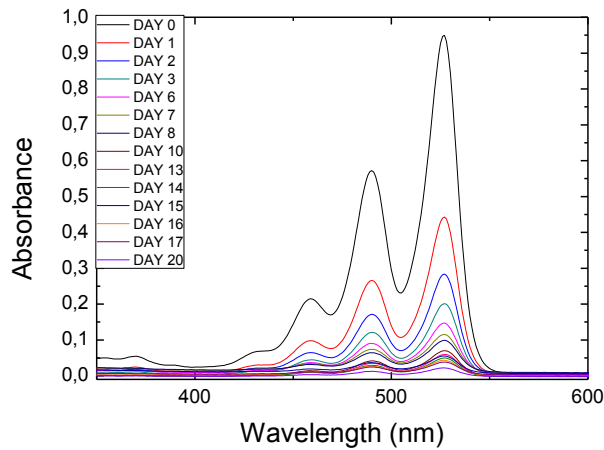
Figure 95: Kinetic of PDI-F + GF 5 mg/mL
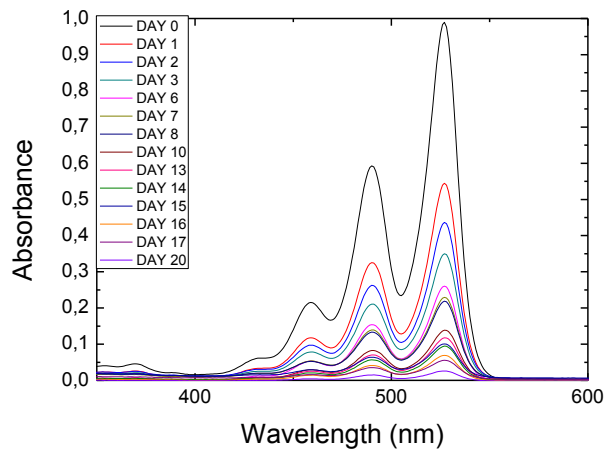
Figure 96: Kinetic of PDI-Cl + GF 5 mg/mL

As can be seen, the kinetics conducted with a larger amount of graphite have an adsorption speed of the dye on the surface considerably higher respect the kinetics with 3 mg, because already after the first three days of stirring, the 50% of free molecules in the solution disappeared. In figure 32 are reported the absorbance value, at specific wavelength (527 nm), respect time. In addition, in this case the PDI-F adsorption speed on the graphite surface is higher than that of the other two molecules.
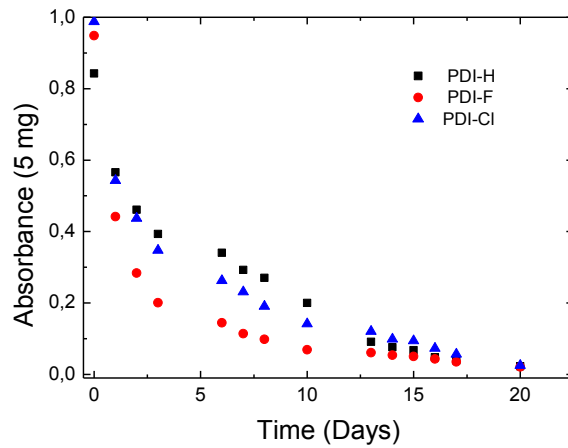
Figure 97: comparison about PDI's kinetics with 5 mg of GF

To determine the different absorption speed between the kinetic conducted with the addition of 3 mg of GF and those with 5 mg of GF, they were plotted the maximum values (527 nm) versus time (days). For simplicity the comparison was only performed for the PDI-F.
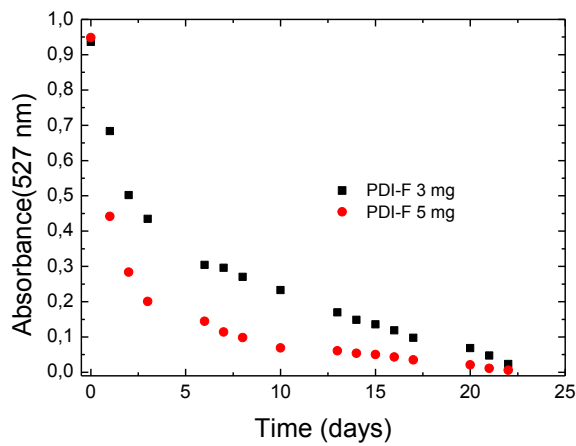
Figure 98: Comparison about PDI-F kinetics with different amount of GF

4.2 Fluorescence analysis

The interaction between fluorescent emitters and graphene is associate local dipole-inducted electromagnetic fields that are strongly enhanced due to the unique properties of graphene: graphene is an extraordinary energy sink with great potential for prospective application in photo-detection, nano-photonic and photovoltaic device.[3] It has evaluated the need to carry out the measurement using spectrofluorimetric techniques in order to understand that interaction occurs between the chromophore (perylene diimide) and the carbon materials, specifically with commercial graphite flakes. Given its high sensitivity, this technique allows monitored with more efficiency possible phenomena of adsorption of molecules on the graphite surface. The solutions used are the same that have been used to perform the studies of kinetics in spectrophotometric techniques. The solutions used have been previously filtered, in order to avoid the phenomenon of light scattering, and subsequently diluted by applying a dilution ratio of 1/10, In this way the absorbance values are less than one, thus avoiding the phenomenon of re-emission that would lead to a false measure. The spectra of the solutions, thus obtained, were excited at a wavelength of 460 nm, and the photons emitted from the excited state of the chromophore, were collected from 480 nm up to 700 nm. The kinetics were conducted by recording the fluorescence spectra of the different solutions every 24 hours. Were tested four different solution: three solutions that having the different perylene diimide with graphite (3 mg/mL) and the fourth containing only the graphite flakes dispersed in chloroform. The integral value, of fourth solution is used as base line and later removed, from the spectra of the chromophore, in order to determine the emission intensity of these compounds. Shown below, are the overlapping fluorescence spectra's of the molecules in exam:
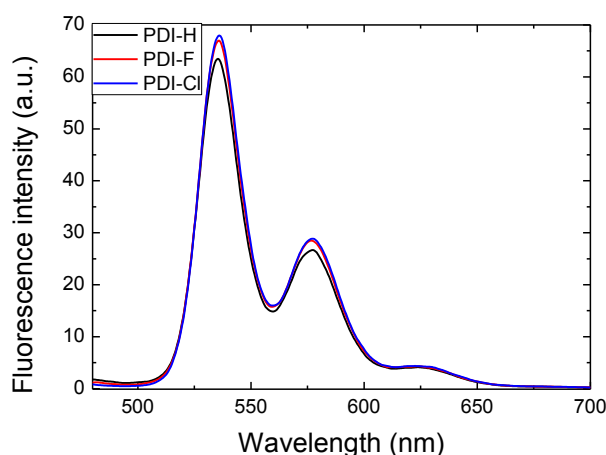

Figure 99: Fluorescence spectra's of PDI

Even in this case is observed as the PDI-F and the PDI-Cl have emission values slightly higher than that of the PDI-h as also found with the previous methodology. Once it was established that the

fluorescence value obtained, does not cause a "blindness" of the photo tube due to excessive exposure to photons of this, it proceeded to analysis of the different solutions. In order to have a comparison with the spectrophotometric techniques, employing previously, the kinetics have been studied up to 23 days after the placing of the graphite and the start of agitation. The following are the kinetics of adsorption studied by fluorimetric techniques:
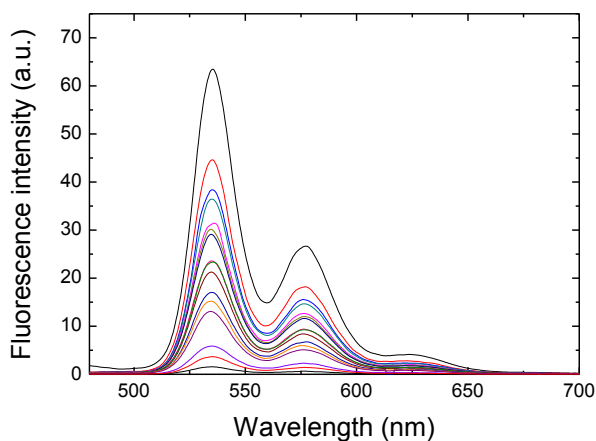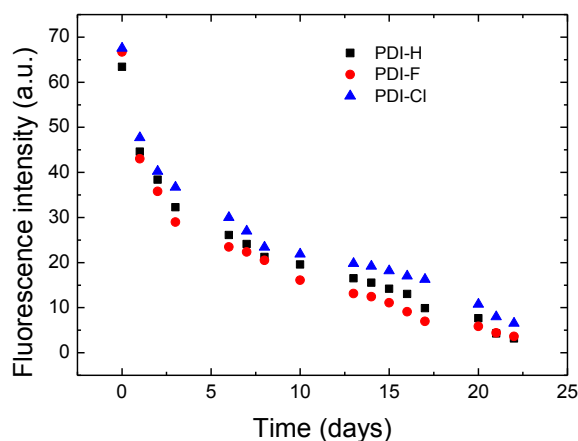

Figure 100: Fluorescence assays of PDI-H
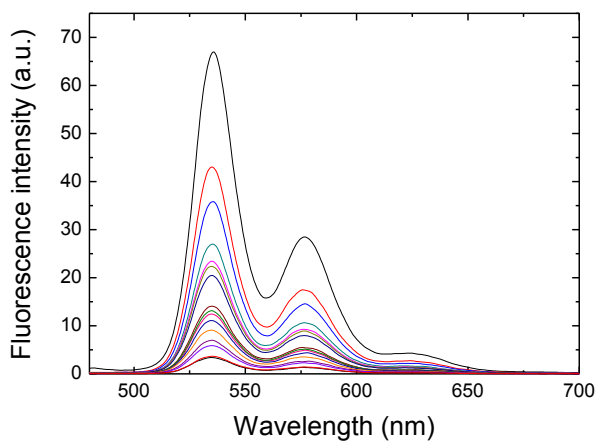
Figure 101: Fluorescence assay of PDI-F
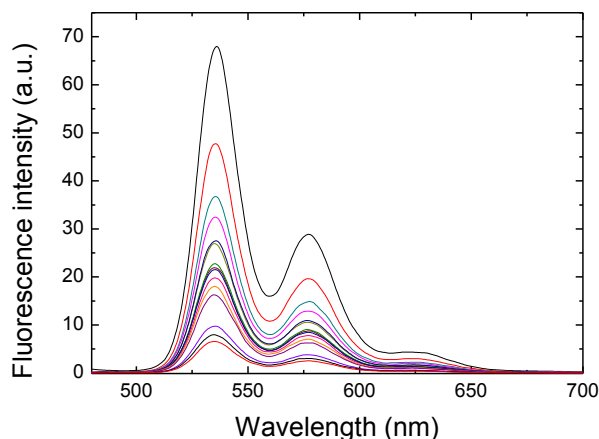
Figure 102: Fluorescence assays of PDI-Cl

Also in this case the speed of decrease of the intensity of fluorescence were compared, whereas the emission maximum (535 nm) as a function of time (figure 103).

Figure 103:Comparison about kinetics conducts with 3 mg of graphite flakes

In this case it can be note how at the beginning the three kinetic shown a very similar decrease, however, already after 5 days of stirring, it is observed a slightly higher decrease in fluorescent intensity for the PDI-F. It may also be observed that after 23 days is still presents the residual fluorescence index that not all PDI molecules are adsorbed on the graphite surface. The next step was determine the speed of adsorption of these molecules, varying the quantity of graphite present. In this case in the solutions were added 5 mg/ml of GF, the operating parameters were held constant, then the order to be able to compare the kinetics conducted with different amounts of adsorbent. Even in the kinetic containing 5 mg of GF were recorded daily four different spectra's

(three going to molecules and one belonging only to chloroform and in which the flakes were included). On day zero, all four tested solutions with those obtained previously, as regards the solution free from the analyte (perylene diimide) there was a constant value of the signal around zero. By kinetic registered, it can see how going from day zero to day one it has a fluorescence decay approximately 50%, which comes to about 70% after 10 days, and then became almost equal to 0 in the last few days. The following are the kinetics of three different molecules.
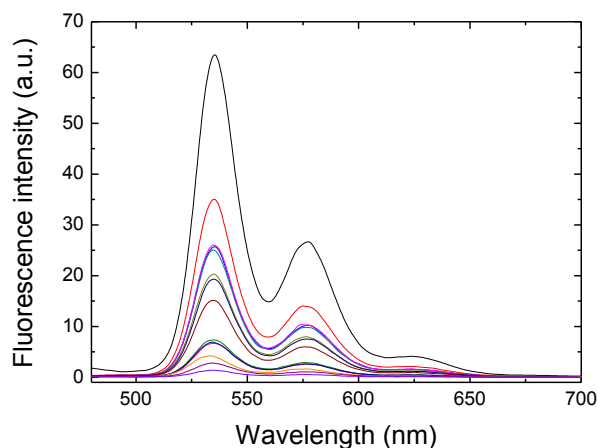
Figure 104: Fluorescence assay of PDI-H with 5 mg/mL
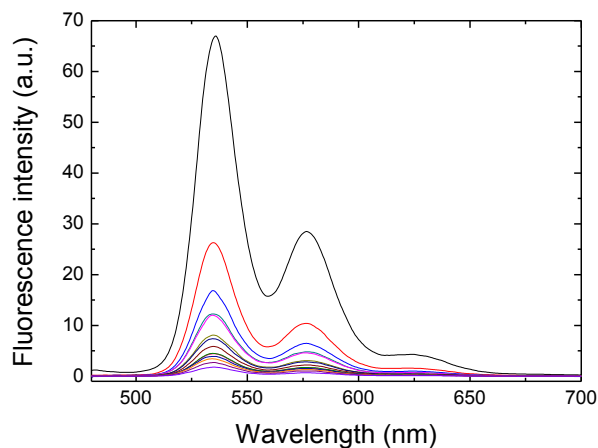
Figure 105: Fluorescence assay of PDI-F with 5 mg/mL
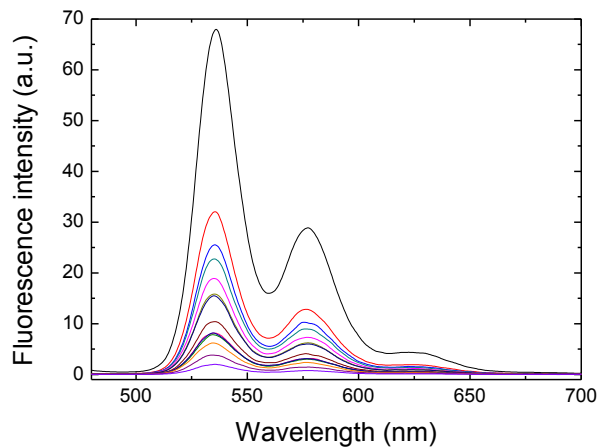
Figure 106: Fluorescence assay of PDI-Cl with 5 mg/mL

Also in this case the PDI-F adsorption speed on the graphite surface is greater than the other 2 molecules, which have very similar trend. In figure 107 were reported the fluorescence intensity at maximum value (535 nm) versus time
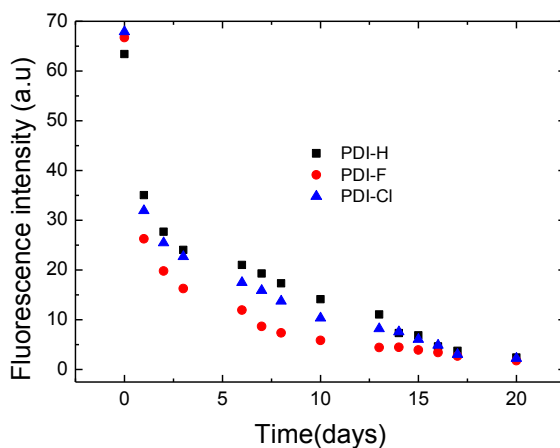
Figure 107: Correlation about the kinetics speed of three molecules

Even in the case of fluorimetric measurements, it is noted that the adsorption speed of the PDI-F molecules is higher than that found in the other molecules.

It shown below (figure 108), the comparison of the speed of the PDI-F adsorption 3 and 5 mg of GF, considered a specific wavelength (535 nm) respect time:
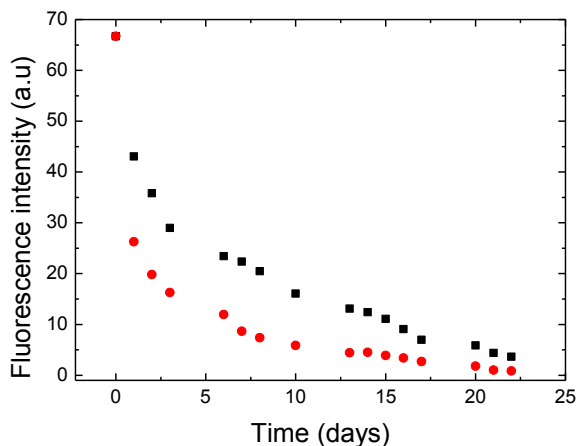
Figure 108: Correspondence about PDI-F with different amount of GF (black dots 3 mg and red dots 5 mg)

It can be see, the previously graph that when the amount of graphite was increase the speed of adsorption clearly increase, in fact after the day 0 where the absorbance value is identical in both solution, after 24 h it can be seen how in the solution with 3 mg of graphite the decrease is around 40 %, meanwhile in the solution with 5 mg of GF the decrease is around 60%. Furthermore, it can be seen that in the solution containing a lower amount of graphite at the end of the kinetics there are less of 6 % of free molecules, whereas this value falls to about 2% with the solution containing 5 mg of graphite flakes.

In the case of a chemical reaction, the interaction between the fluorophore and the photon is determined according to the parameter of the quantum yield. In general the quantum yield is calculate respect to a standard molecules where is know the physical-chemical properties (quantum yield , refractive index, density etc.) The quantum yield, of new matrix is calculate by the following equations:

$$\Phi = \Phi_r * (I/I_r) * (A_r/A) * (n^2/n^2_r)$$

Where Φ_r is the quantum yield, A is the absorbance at the excitation wavelength, n is the refractive index of solvent; and r is the reference. The reference used as a standard molecule, for quantification of the quantum yield was coumarin 153, which has been solubilized in ethanol. The solutions analyzed by spectrofluorometer (PDI and coumarin) must submit an absorbance value less than 0,05-0,1, in order to avoid the phenomenon of "reabsorption of fluorescence" which would lead to an incorrect value of quantum yield.
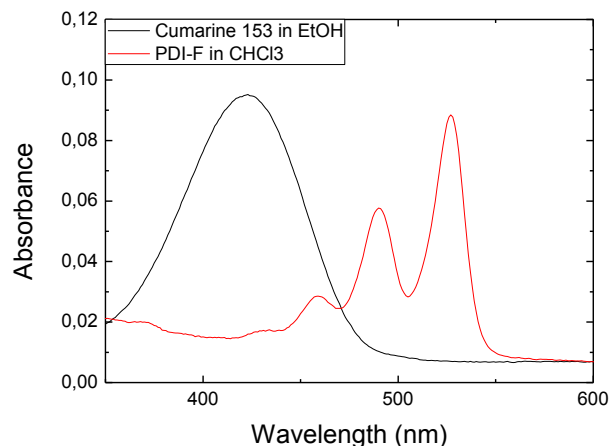
Figure 109: Correlation between the reference molecule (Cumarine) with PDI-F

The resulting solutions were excited at the wavelength of 470 nm, and began to collect photon decay from the excited to the fundamental state at 490 nm. From the obtained fluorescence spectra, the value of the integer (area under the curve) is obtained, which will then be used to determine the value of the quantum yield, known by all other parameters (refractive index, absorbance, integral value).The following are the values of the quantum yields obtained and compared with the values of the ε (molar extinction coefficient) obtained previously.

Table 7: Relationship between ε and Φ.

Molecules	Molar attenuation coefficient (ε) (L/mol*cm)	Quantum yield % (emitted photon/adsorbed photon)
PDI-H	58783,49	64,27
PDI-F	79489,52	63,62
PDI-Cl	74774,25	64,45

Since as can be observed, in the case of the quantum yields the values obtained are more or less similar and this indicates that the lateral substitution slightly changes the properties of these molecules.

4.3 Surface area analysis

A relative great proportion of the atoms to of a fine powder are in or near the surface. If, in addition, the powder particles have cracks, crevices or pores within their structure, the proportion of exposed atom is still greater. This causes powders to exhibit distinctly different properties from the same material in bulk from and to do so in a manner strongly dependent on the magnitude of their surface area and the nature of their porosity.

For this reason it was chosen to determine the surface area of the graphite sample commercial (Sigma Aldrich) to determine, if such material undergoes dimensional changes as a result of the treatment to which it is subjected. The surface area measurements were carried out by comparing the variation of the surface area, of the solutions obtained by combining graphite and chloroform, respect to the stirring time. To determine the variation of surface area it is decided to determine this property in different solution treat from zero, two, four, six , eight, ten, twelve, to fifteen, eighteen, twenty-one and twenty-four days of constant stirring. At the end of predetermined days, the samples are stopped, and the solvent removed by filtration. The quantity that is inserted within the older is determined based on an estimate of the surface area, as materials having low surface area require higher amounts of materials, vice versa for those containing high surface area. In the case of a graphite commercial sample, which is expected to have a low surface area, the quantity that has been inserted within these ampoules is about 2 g. In such measurements the result is reproduced as a surface area per gram of inserted material, in fact the sample is weighed immediately before pretreatment and immediately after. Obtained the powders they are inserted inside the older, undergoing a pre-treatment at 300 °C, under high vacuum condition (13 µbar) for 3 hours as required by ISO 9277: 2010. The difference in weight that is obtained before pretreatment and after is due to the loss of materials on the surface such as humidity or volatile organic compounds that during pretreatment are removed. Performed the pretreatment of the sample and weight it, the older are positioned in the measuring unit, where the interaction takes place between the powder (in this case graphite flakes) with the gas (nitrogen) that are going to adsorb on the solid surface. The whole system is inserted into a chamber containing liquid nitrogen as provided in the ISO norms mentioned above. Result, that is obtained, derive from an average of the weight changes that are obtained when the sample is blown with nitrogen at different pressures (0,05; 0,1125; 0,175; 0,2375; 0,3 P/P^0). The value obtained is then the BET surface area. Since the graphite used, a commercial product, it was decided to perform for each time a series of different measures(six samples for each different stirring time), in such a way also as to determine the variability of the substrate. All samples with stirring time, different from zero, were treated in the same method also

describe before. Shown below are the average values of BET surface area (expressed in m^2/g) of the samples tested.

Table 8: BET area values with different stirring days

Stirring time (days)	BET average value (m^2/g)
0	1,7 ± 0,2
2	2,2 ± 0,1
4	3,0 ± 0,05
6	3,6 ± 0,1
8	4,4 ± 0,2
10	5,5 ± 0,1
12	6,3 ± 0,1
15	7,2 ± 0,1
18	8,6 ± 0,1
21	9,8 ± 0,1
24	11,0 ± 0,1

As can be observd the prolonged agitation leads to the fragmentation of graphite flakes, with a consequent increase in surface area of the graphite. In figure 44 it was plotting the area values ,obtained, respect time. It can be observed that there is a linear increase over time, indicating that increasing the stirring times it always get a more uniform material without harshness.
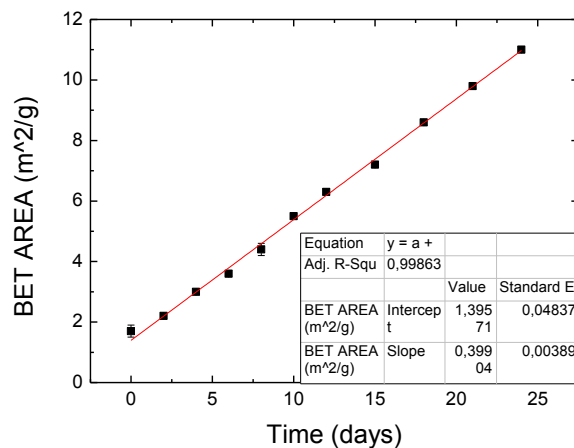
Figure 110: Best linear fit between BET area and time

The increase of surface area, this may also be seen as an increase of the space available to the PDIs molecules to interact through π-π*bonds with graphite. Knowing the absorbance value obtained by UV-VIS spectrum as a function of time, it is possible to determine the concentration of the solution in that specific day, the known value of Avogadro's number is cleared later to determine the remaining number of free molecules in solution. Known also the surface area value (assuming a linear behavior up to 23 days), it is possible to determine the space that each of PDI molecule has available on the graphite surface.

Determined the space available for each molecule of PDI on the graphite surface, it expands the determination even for the kinetics that were conducted with 5 mg of GF. The results demonstrate that increasing the quantity of graphite, also the quantity of surface area for each molecule increases, since as can be seen in figure 111:
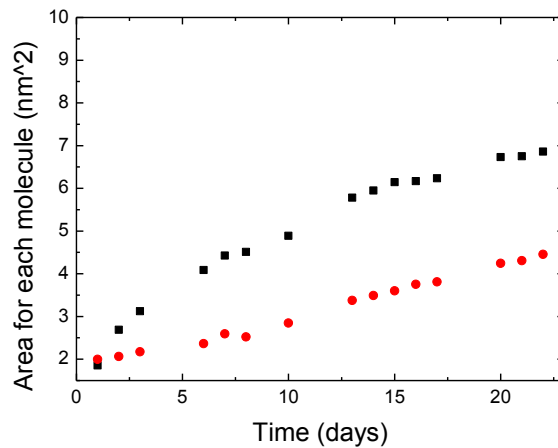
Figure 111: Comparison between area for each molecules of PDI- F with 3(red dots) and 5 mg of graphite flakes (black dots)

From the figure is also encountered another important factor, namely in the early days the values of available space for the molecules and about the same in both the kinetics, but already after 5 days of stirring it has been observe a rapid increase of the available space in the kinetic conducted with 5 mg of graphite.

4.4 Granulometric measures

The size of the particles greatly influence the properties of the material, for this reason, should usually match in addition to the determination of the surface area of the powder under examination also a size of the particles contained in it, so as to also establish the main properties such as the reactivity.

The determination of the size of the particles is conducted by introducing within the granulometer a suspension of the test material in an appropriate solvent. In the case under examination we were tested the same "solutions" used previously for the measures of surface area. The ISO standards concerning the measures of the size of the particles (EN ISO 8130-13), involving the use of various solvents to suspend the powder (mainly isopropanol, ethanol, water, toluene). For our case of the graphite material (few mg) are suspended in 20 mL of IPA (isopropyl alcohol or 2-propanol) until obtaining a homogeneous suspension. The granulometric measure of the size of the particles consists in the determination of the variation of the angle of diffraction which is obtained when a laser hits the particles. For a simpler treatment of calculations, graphite particles are considered to be spheres, although their actual form aren't spherical. Large particles scatter light at small angles relative to the laser beam and small particles scatter light at large angles, as illustrated below. The angular scattering intensity data is then analyzed to calculate the size of the particles responsible for

creating the scattering pattern. The particle size is reported as a volume equivalent sphere diameter. From the measurements of different samples, it goes back to a population distribution of particle size. In figures (112-114) are reported the population distributions of the equivalent diameters of the particles recorded for the days two, eight, fifteen:
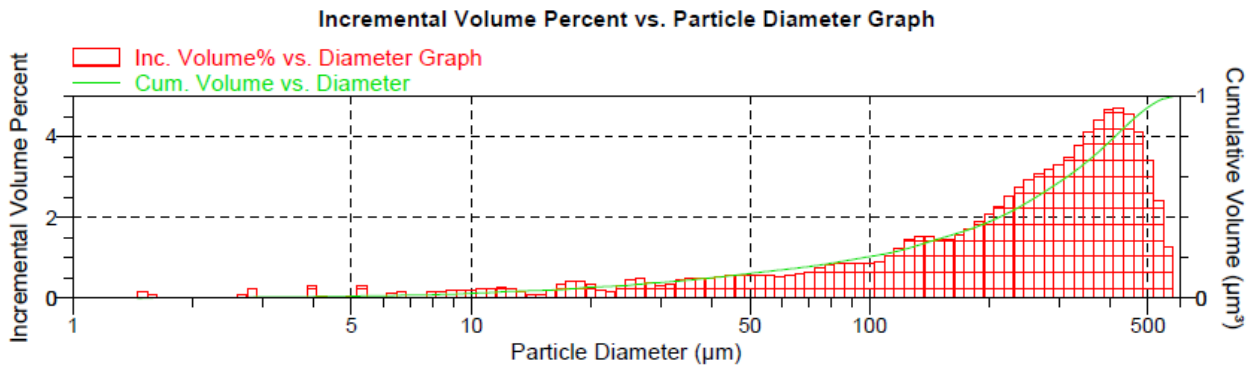
**Figure 112: Population distributions of the equivalent diameters of the particles for the sample stirring for two days**
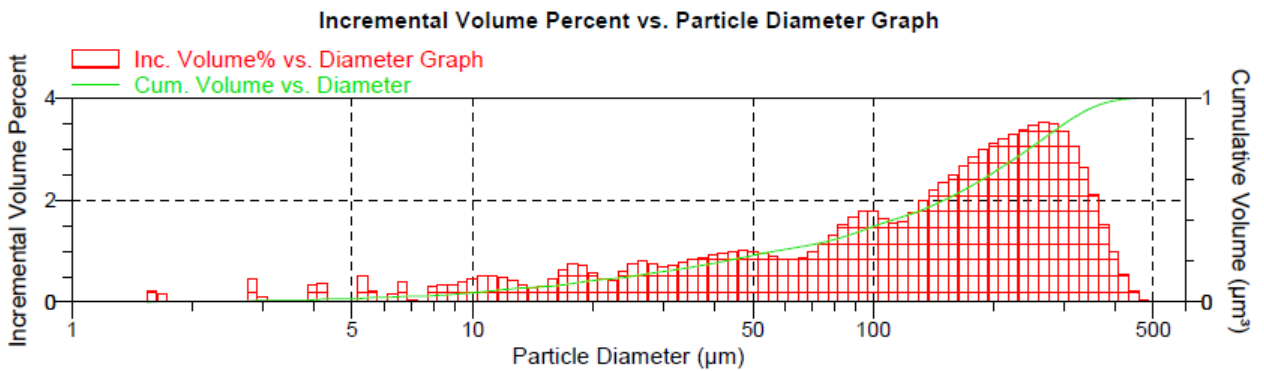
Figure 113: Population distributions of the equivalent diameters of the particles for the sample stirring for 8 days
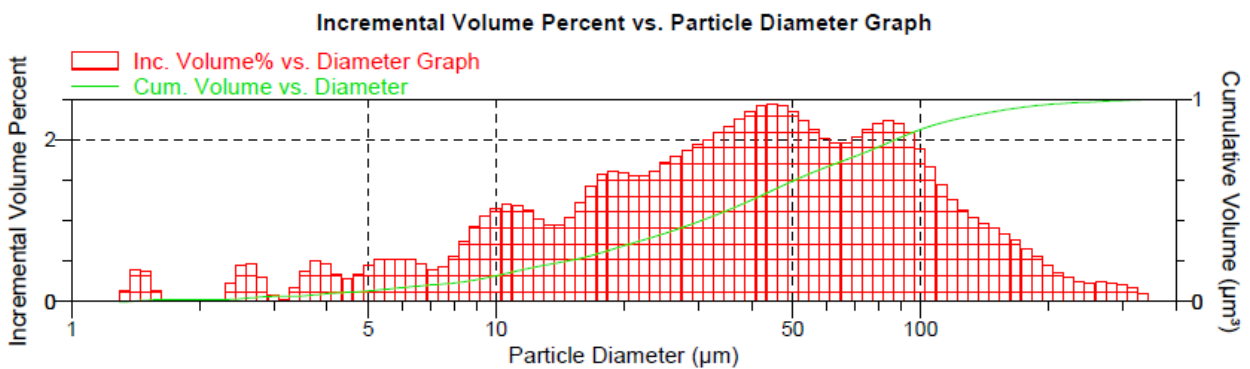
Figure 114: Population distributions of the equivalent diameters of the particles for the sample stirring for 15 days

Since as can be observed from figures 3 above, is known as increasing the stirring period you have

a left shift of the particles, or a decrease of the equivalent diameter of the spheres. In figure 115 are shown the effective diameter versus time.
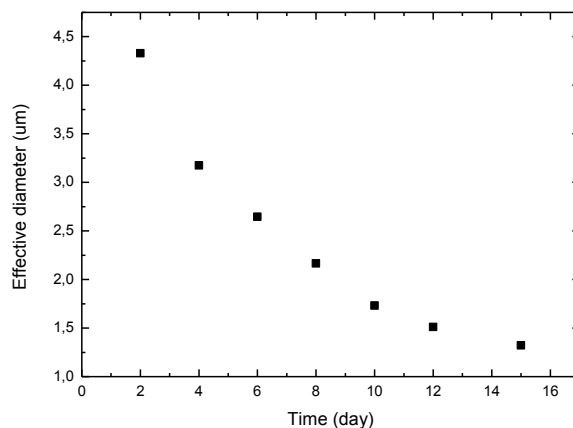
Figure 115: Comparison between effective diameter and time

In the previous figure it is shown that increasing the agitation days the effective diameter of the particles decreases, in fact, from day zero to day fifteen it can be seen how the effective diameter changes from an average value of 4.5 μm to about 1.25 μm. No further tests have been carried out after 15 days of agitation, but already as confirmed in the case of BET this diameter value will tend to decrease as the stirring time is increased. The BET distribution of the diameters provides other important information including the D_{10}, D_{50}, D_{90}. These three values are mainly used in the industrial environment, as they give an idea of the average value of the particle size, which is especially important in the case of catalysts, in which the smaller particle size gave the best efficiency of the catalyst. The D_{50} value is the median, has been defined above as the diameter where half of the population lies below this value. Similarly, 90 percent of the distribution lies below the D_{90}, and 10 percent of the population lies below the D_{10}.
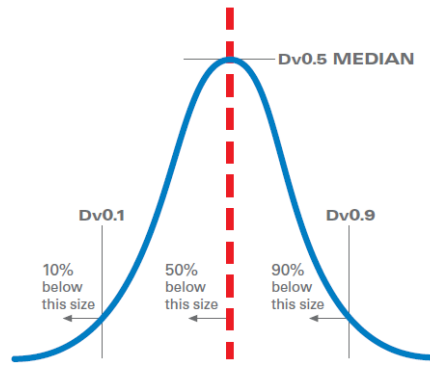
Figure 116: Three x-axis values D10, D50 and D90

The determination of these three values are obtained considering the percentiles at 10, 50 and 90 and determining the value that is obtained through the following graph:
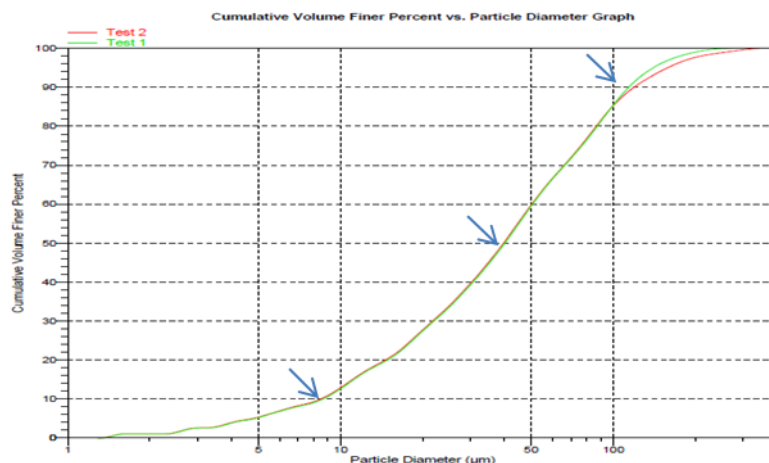

Figure 117: Determination of D values

Figure 117 shown a graph in which the y axis is reported the number of percentiles, while the x-axis shows the diameter of the particles.

The arrows shown in the graph indicate where the three values above are derived, let's consider the D_{50} to take the straight line starting from the percentile at 50 and tracing a parallel straight to find the particle diameter distribution curve in this. Therefore, it can get the percentage of population, 50 %, which has a diameter below this value.

Applying the same principle for all the samples analyzed and plotting the values obtained respect time (figure 118), it is observed as the values obtained for the D_{10} remain almost unchanged, as opposed to those of the D_{90} where passing from day two to fifteen days is It has a remarkable decrease (from about 500 to about 150 µm):
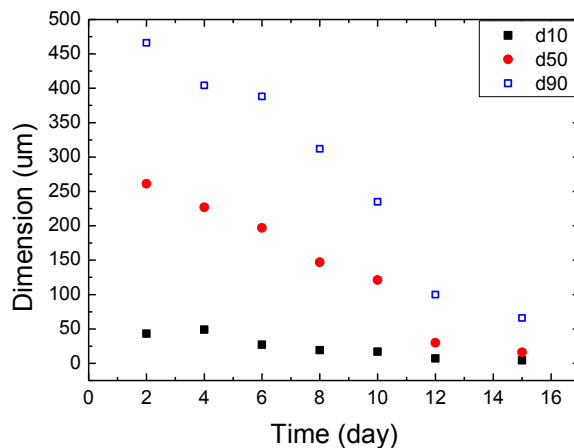
Figure 118: Different D values respect time

4.5 TGA/DSC,ICP and IR analysis

The thermo gravimetric analysis has been conducted, since the graphite being a commercial sample, it wants to determine the purity of this, and possibly determine any contaminants that may interfere with the fluorescence and spectrophotometry analysis.

In the case of thermo gravimetric analysis of the graphite flakes samples were added inside of sample holder and transfer on TGA instrument, and the analysis was conducted with a temperature gradient of 15 °C per minute. The TGA analyzes were performed either in an inert atmosphere (N_2) which in a reactive atmosphere (in the air), in order to determine possible thermal degradation in the presence or absence of oxygen. The temperature ramp was set to 15 °C per minute so as to test all the possible variations in mass.

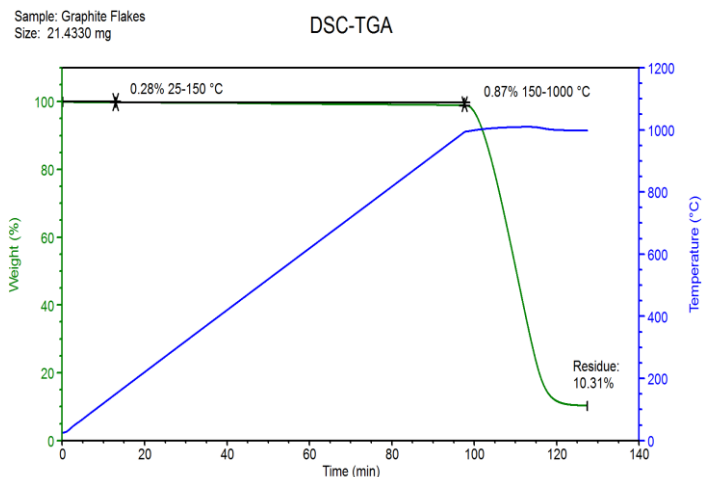The following were the thermograms recorded in the absence and presence of oxygen, respectively (figure 119-120)

Figure 119: Thermogram of graphite flakes recorded in nitrogen with temperature ramp of 15°C/min
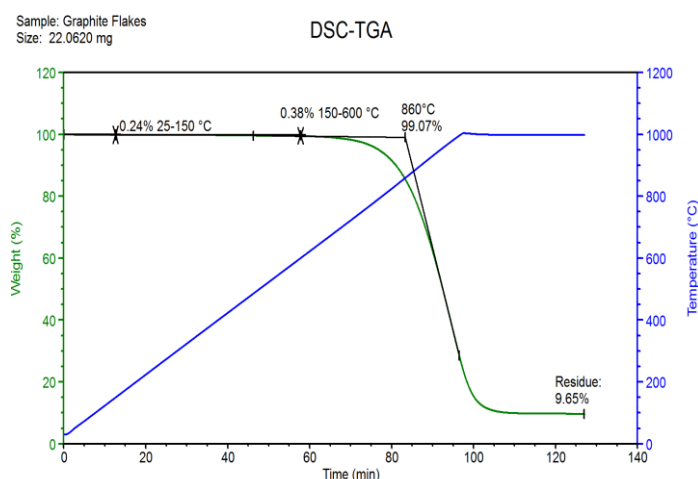

Figure 120: Thermogram of graphite flakes recorded in air with temperature ramp of 15°C/min

Since as seen in figure 119 (thermogram recorded in nitrogen), it was observed as increasing the temperature up to 150 °C there was a slight weight loss (0.28%) due to the removal of the water present within the matrix . Continuing the heating up to 1000 °C is observed another loss in mass is equal to 0.59 % due to the removal of VOC (volatile organic compounds). Finally maintaining the sample at the temperature of 1000 °C for another 30 minutes is observed a significant decrease in terms of mass, due to thermal decomposition of the graphite mainly in CO. When the process is observed a residue of unburned (ash) equal to 10.31%.

From the thermogram conducted in air (figure 120), it is observed as the thermo degradation (combustion) of the graphite, significantly begins earlier than that in nitrogen, in fact up to a temperature of 600 °C is observed only a slight variation in the mass (0.38 %). At a temperature of 860 °C it is observed the maximum decrease of mass of the sample, which arrives to 9.65 %, i.e. the unburned ash content.

130

In the case of the sample containing only the graphite the DSC combined with the DTA was not made, since the graphite has no variation of the enthalpy content in the measuring range used. From the ash unburned it was decided to make a ICP analysis so as to determine the quantity of metals present in the commercial graphite.

For this purpose, the residue was dissolved in nitric acid, suitably diluted and inserted into the intake chamber of the ICP.

The ICP analysis results are shown in table 10:

Table 9: Amount of each metal inside graphite flake

Sample	Metal	Quantity (PPM)
	Fe	12091,59
	Mg	349,348
	Ti	185,049
Graphite flakes	Mn	125,654
	Zn	50,063
	Ba	28,575
	Pb	7,655
	Th	0,937

From the results obtained it is observed as the primary "contaminant" present inside the graphite matrix is iron, followed immediately by magnesium.

Once the graphite thermograms were determined, both in nitrogen and in air, the thermal properties of the molecules were determined. These were recorded to determine fundamental physical properties such as melting, decomposition temperature, etc.

Thermogravimetric analyzes were conducted both in inert atmosphere and in oxidizing atmosphere in order to evaluate the variation of thermograms under different operating conditions. Figure 121 shows the thermograms of the PDI-H recorded respectively in air (high) and in nitrogen (low).
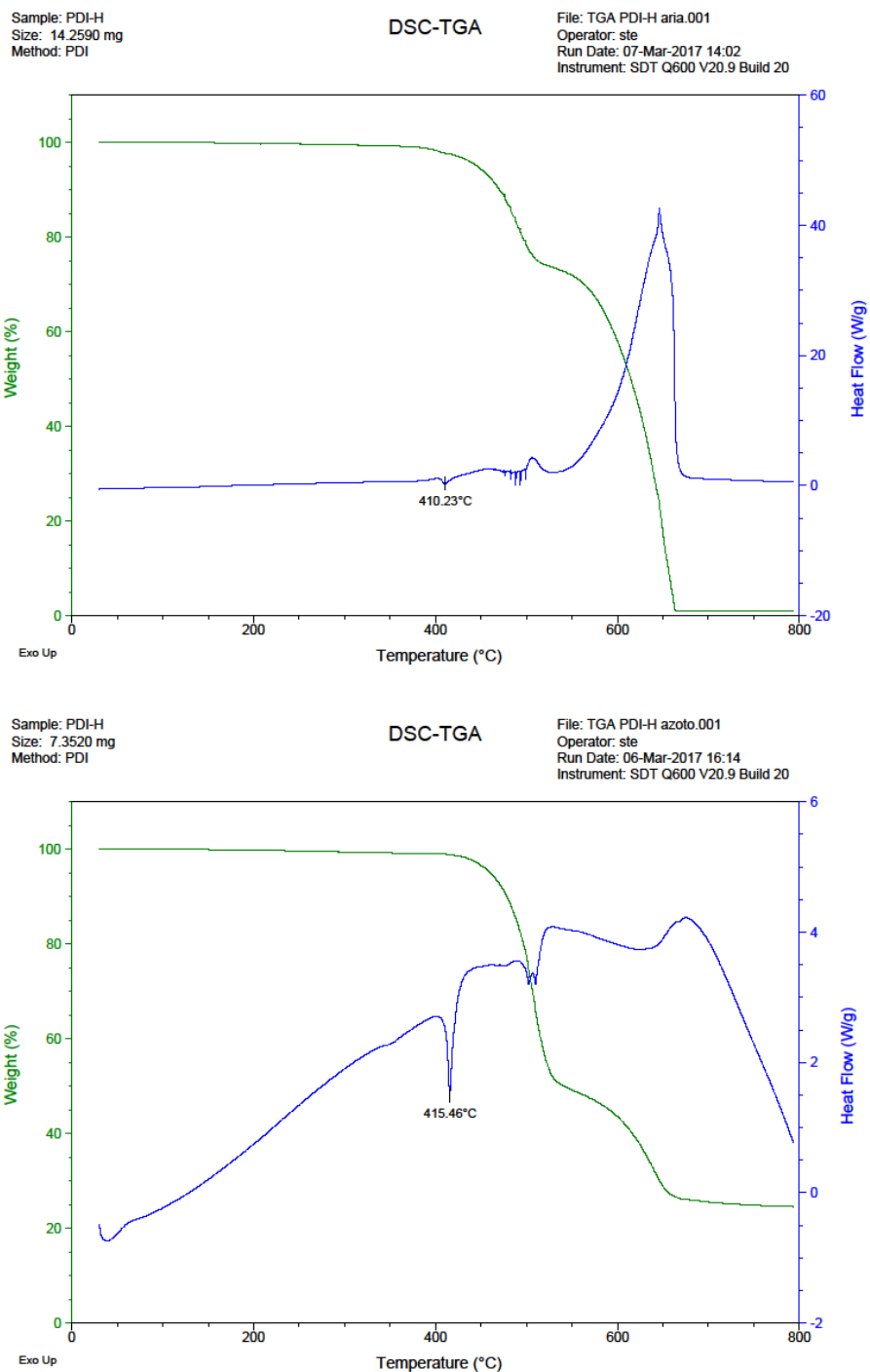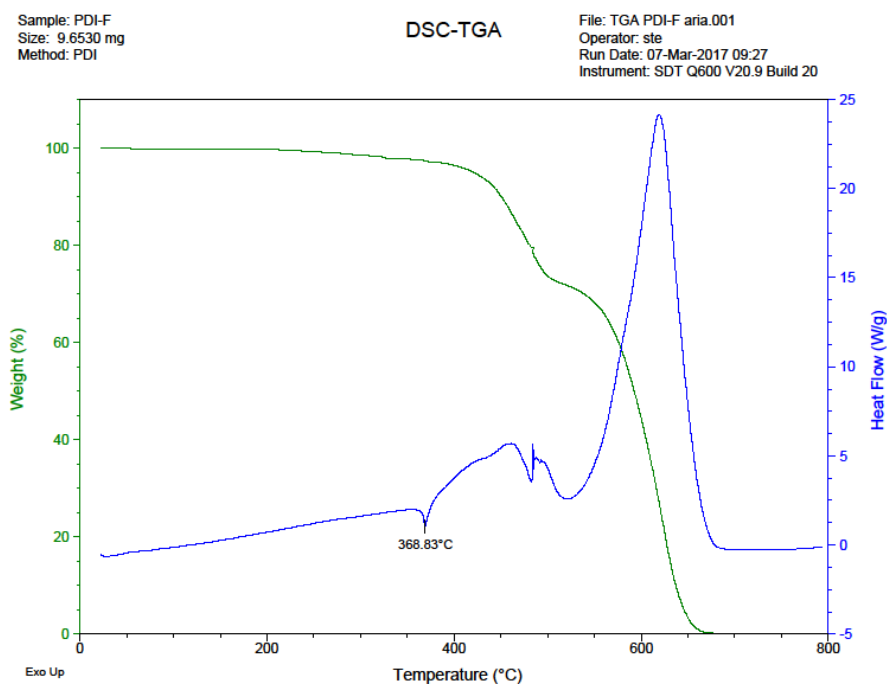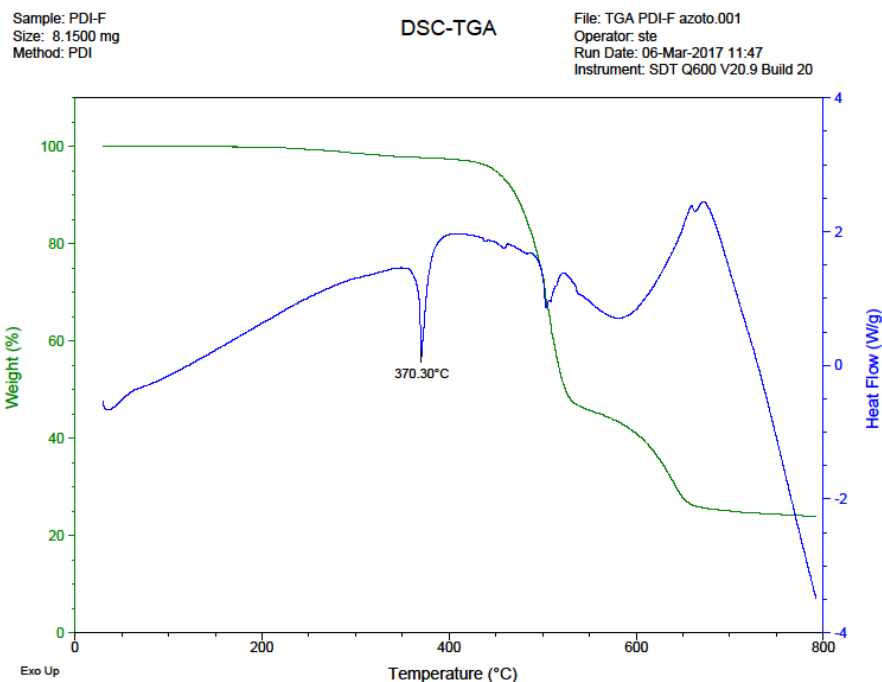
Figure 121: TGA/DSC analysis for PDI-H recorded in air (top), and nitrogen (bottom)

From the thermograms shown in figure 121 it can be noticed that changing the reaction environment also the mass variations are considerably different, because in the thermogram recorded in the air, the degradation of the molecule starts at about 410 °C while in nitrogen about 415 °C, it is also noted that at the temperature of about 520 °C the mass decrease in the sample in the air is about 25% then it becomes 100% when the temperature is over 650 °C. However, this

situation does not occur in an inert atmosphere where at about 520 ° C we have a 50% mass variation which then becomes 75% at a temperature higher than 650 °C.

From the DSC signal (in blue) a fairly similar pattern is observed, observed at the temperatures of 410 and 415 °C (in air and nitrogen respectively) of the peaks with a negative heat flow index of an endothermic process due to the fusion of the molecule. All subsequent peaks have a positive heat flow, indicative of an exothermic process due to degradative factors occurring in the molecule. Figure 122 shows the TGA / DSC for the registered PDI-F molecule in air and nitrogen.
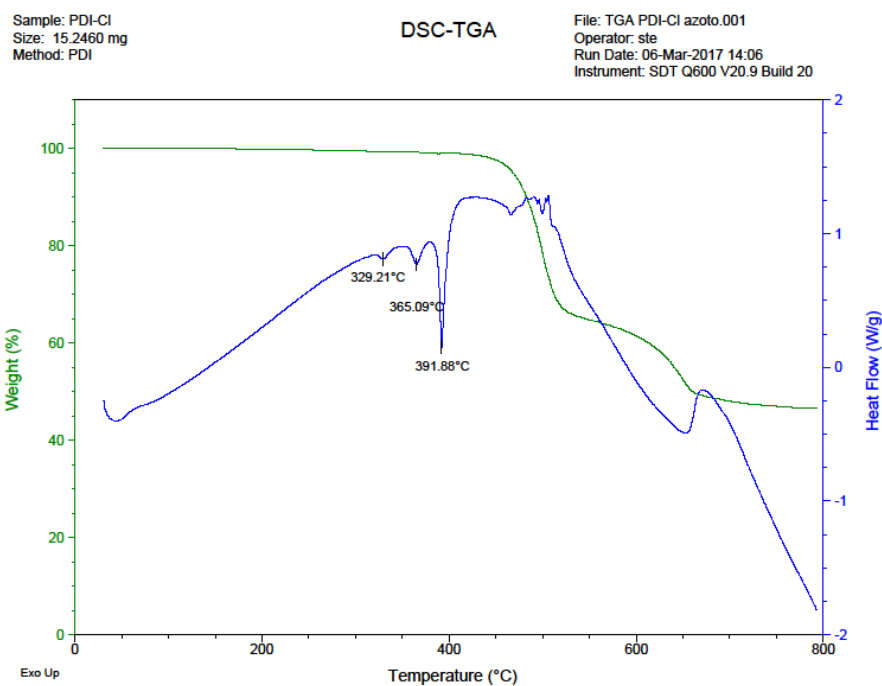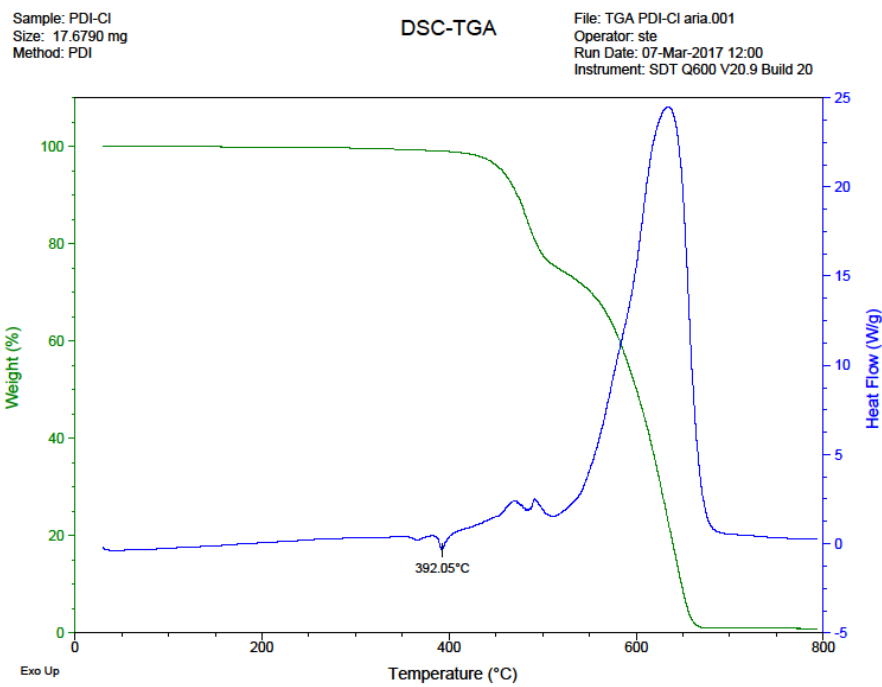
Figure 122: TGA/DSC analysis for PDI-F recorded in air (top), and nitrogen (bottom)

In the case of PDI-F it can be observe that the molecular fusion temperature is very similar both in nitrogen and air (369-370 °C). In the thermogram recorded in the air it is observed that the first significant variation of mass (about 25%) is observed at a temperature of about 375 °C, further increasing the temperature to about 500-510 °C the complete combustion of the molecule in As the residual mass percentage is equal to 0. In the thermogram recorded in nitrogen, a trend similar to that seen in the case of PDI-H is observed, that is, the first significant mass variation is observed at a temperature of 370 °C and terminates at a temperature of about 520 °C, in this step the mass variation is about 55%. A further increase in temperature up to 660-670 °C leads to another mass variation of about 20%. By increasing the temperature again, no significant mass variations are observed. As in the case of PDI-H, in this case also DSC signals derive from the molecule's fusion (peak at 369/370 °C respectively) and its degradation (T> 500 °C).

In figure 123, shows thermograms recorded in reactive and inert atmosphere respectively:

Figure 123: TGA/DSC analysis for PDI-Cl recorded in air (top), and nitrogen (bottom)

In the case of TGA recorded in both nitrogen and air it is noted that the first significant mass variation starts at a temperature of about 400/410 °C until it ends at a temperature of about 510/520 °C where mass variations is around 22%. In the case of the thermogram recorded in the air, an increase in temperature further leads to the total degradation of the molecule; In the case of the nitrogen-recorded thermogram, an increase in temperature causes another mass change (up to 55 %) to stabilize for even higher temperatures. In the case of DSCs recorded in both nitrogen and air we

observe completely different behaviors or in the case of the differential scanning calorimetry recorded in nitrogen there are 3 endothermic peaks due probably to a variation of the crystalline phase of the molecule, which to reorganize requires some energy . Determined the thermal profiles of graphite free molecules, the thermal profiles of the mixtures containing the molecules and graphite (3 mg / mL) were studied. The following are the comparison of thermogravimetric of the molecules, the molecules + 3 mg / mL of graphite and the graphite flakes (figures 124-126).
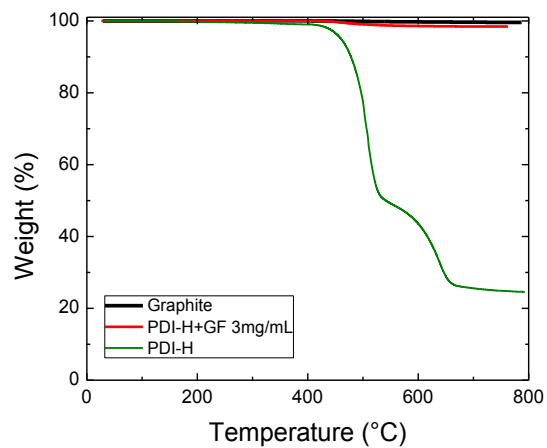
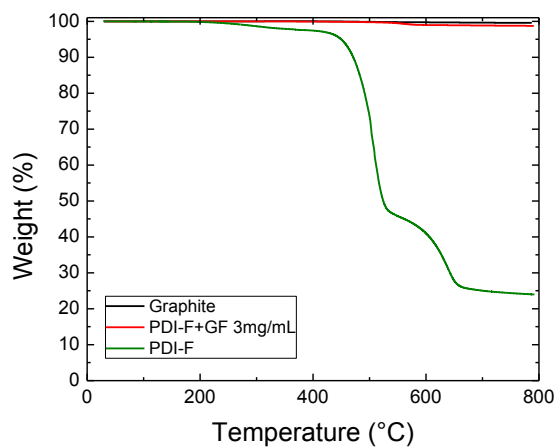**Figure 124: Comparison between PDI-H, PDI-H+ GF and graphite flakes**

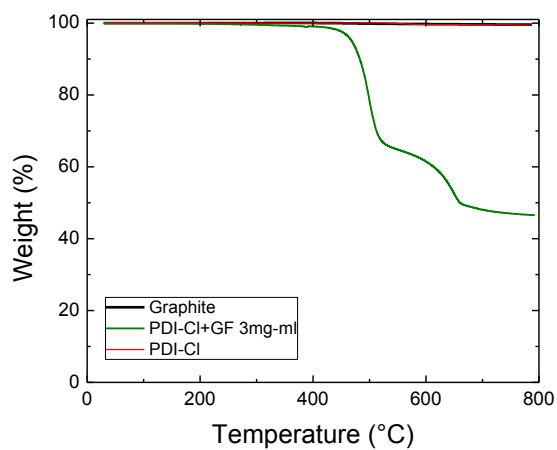**Figure 125: Comparison between PDI-F, PDI-F+ GF and graphite flakes**

Figure 126: Comparison between PDI-Cl, PDI-Cl+ GF and graphite flakes

137

From the previous figures it can be observed that there is a slight difference between the red and black curves, this slight difference is due to the pinning adsorbed molecules (<1% with respect to the total mass).

From previously performed thermogravimetric analyzes it can be seen that, in the case of thermograms recorded in the air, the molecular decomposition temperature reached the complete degradation of the solid. This phenomenon is less pronounced in the case of thermograms recorded in nitrogen where two steps are observed that lead to a stabilization of the final mass. For this purpose, infrared microscopy analysis was performed to determine the possible decomposition products of the PDI-F molecule. For this purpose, an aliquot of the pure molecule was subjected to a thermal analysis in the same range as previously used. The only change made in the system has been to convey the gas, due to decomposition, in an IR spectrometer. Analysis of the gases produced is obtained a mixture of products which later can be discriminated by exploiting the signals, derived from different functional groups, present in the IR spectrum. The IR analysis was performed by conveying the gases obtained at the temperature of decomposition of the PDI-F at 485 °C. Figure 127 shows the IR spectrum of the gases containing the products of thermal decomposition.
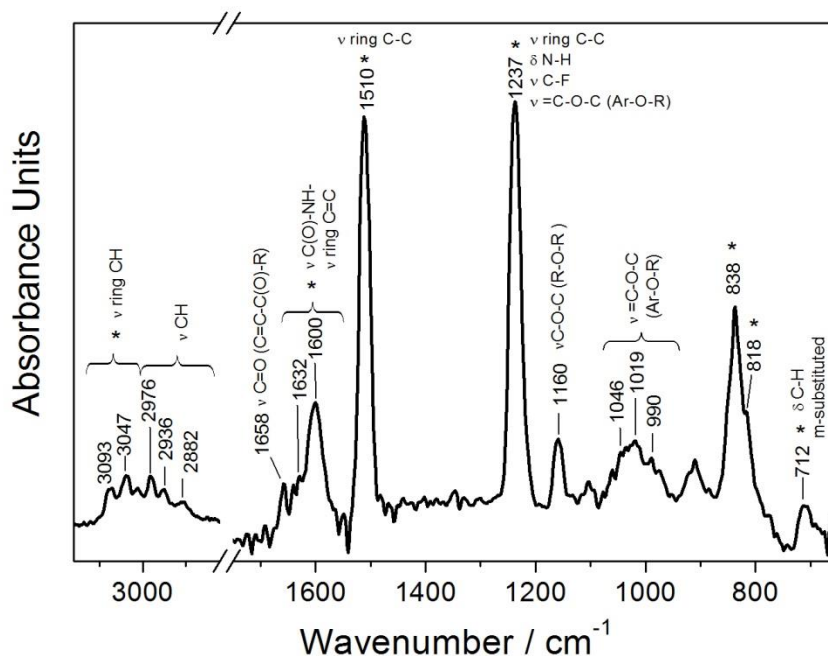

Figure 127: IR spectra of possible decomposition products. Where * indicated the ring vibration of molecules, ν is the stretching vibration and δ indicated the banding vibration

Figure 128 shows IR spectra obtained for possible decomposition products compared to the IR spectra reported in literature:
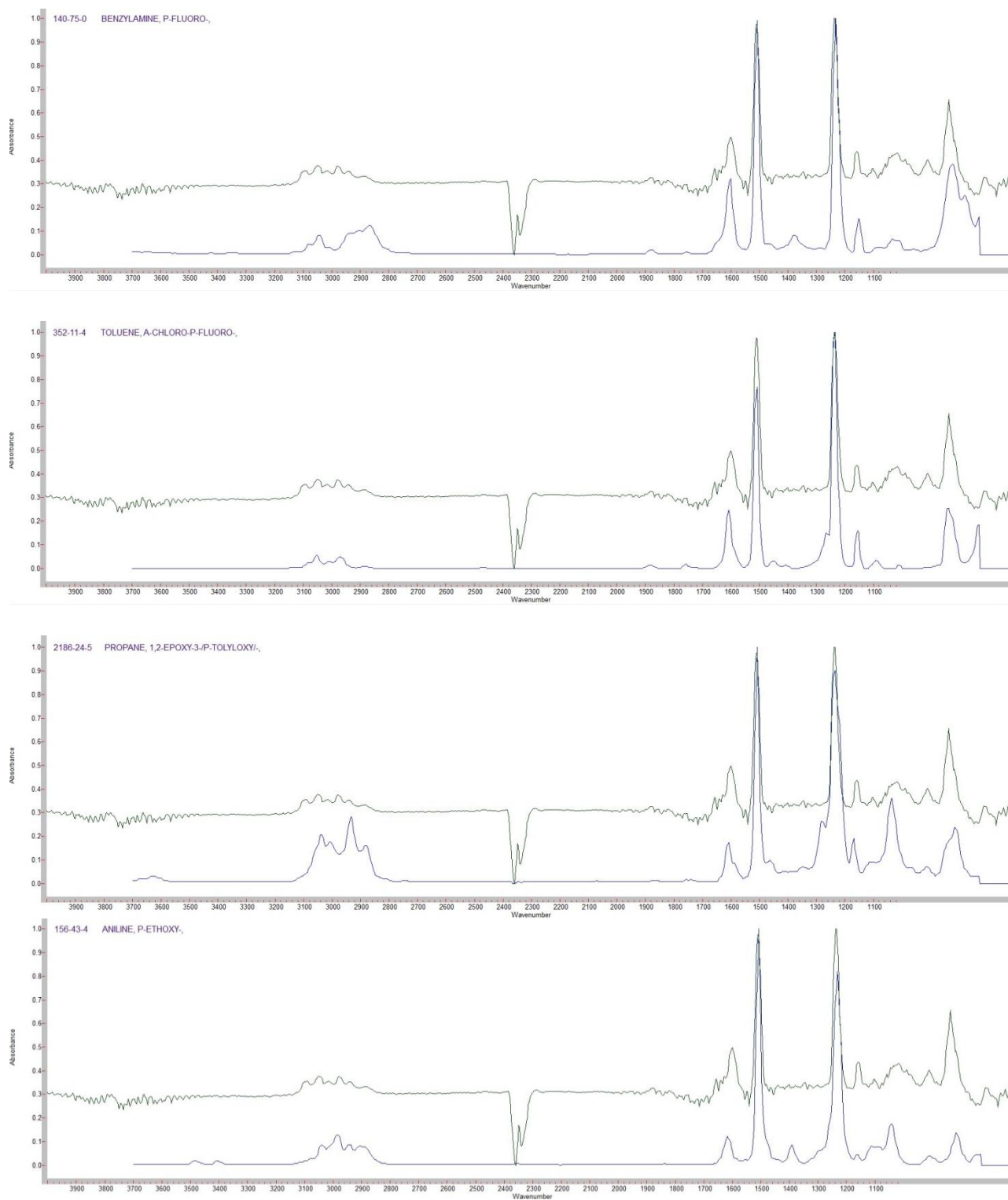

Figure 128: IR spectrum of the product combined with the possible molecules presenting similar IR spectra

From the above figures it can be observed as in the range between 1670-1590 cm-1 there is the presence of carbonyl groups (ν C = O), also it is observed the aryl conjugation phenomenon that leads to a shift of frequencies to more values downs. In the decomposition products it is still has the presence of a strongly aromatic structure as demonstrated by the presence of bands at 1512, 1238, 838 and 818 cm^{-1}. In particular, the latter can be attributed to the vibration of the m-substituted benzene. From the spectrum also is observed that a possible decomposition product has a functional group consisting of an aryl ether, what is suggested by the bands present at 1160, 1040 cm^{-1} due to the Ar-O-R vibrations. The presence of F can be neither confirmed nor refuted, as the C-F bond gives rise to a very intense band (intensity of this signal increases with the increase of the number of fluorine present within the molecule) at around 1240 cm^{-1}, but where there is also the presence of very intense aromatic bands (ν C-C vibration ring, δ NH banding vibration, ν = C-O-C (Ar-O-R)).

4.6 SEM & EDS analysis

SEM (scanning electron microscopy) analyzes were conducted to identify morphological changes in graphite after agitation.

SEM characterization was also used to determine how molecules are placed on the surface of graphite flakes. For the determination of morphological variation / interaction of the molecules, four different solutions were analyzed:

- Graphite flakes stirring 15 days
- PDI-F stirring 5 days
- PDI-F stirring 15 days
- PDI-F

All the solutions were deposited, using drop-cast technique, on an silicon oxide wafer, and then analyzed.

Before laying solutions in silicon oxide wafer (300nm), all silicon wafer was washed according to the following procedure:

- 15 minutes in an ultrasonic bath within a beaker containing IPA (isopropyl alcohol)
- 15 minutes in an ultrasonic bath within a beaker containing acetone

Between the first wash and the next the samples were dried with nitrogen to remove any contamination particles still present on the surface. After washing the silicon wafers, the samples were deposited (100 μL) by drop-casting technique, as it was easily applied and reproducible.

During the determination of sample morphology, EDS spectra were also determined, that was, the determination of the components (elements) present in the sample. Below is a characteristic graphite bundle deposited on a SiO_2 wafer:
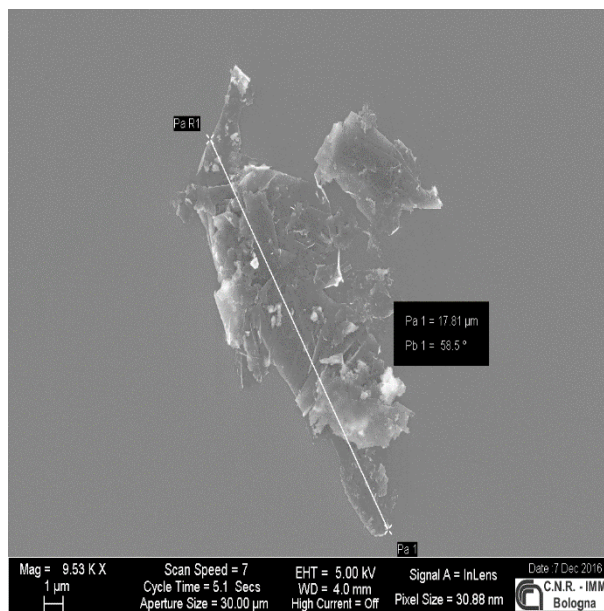
Since as can be seen from the figure, the flake has a quite irregular structure formed by the presence of more jagged floors. Continuous agitation leads to the fragmentation of these irregularities with a consequent increase in the surface area, as previously confirmed by both BET and granulometric measures.

Once the characteristic structure of the graphite flakes has been observed, it has been observed how the morphology varies when the molecules are placed on the graphite surface.

From figure 130 it was shown sample within PDI-F + GF stirring 5 days, it can be observed that there is more homogeneous and less jagged material, and the interactions that have arisen between the molecules (PDI) and graphite.
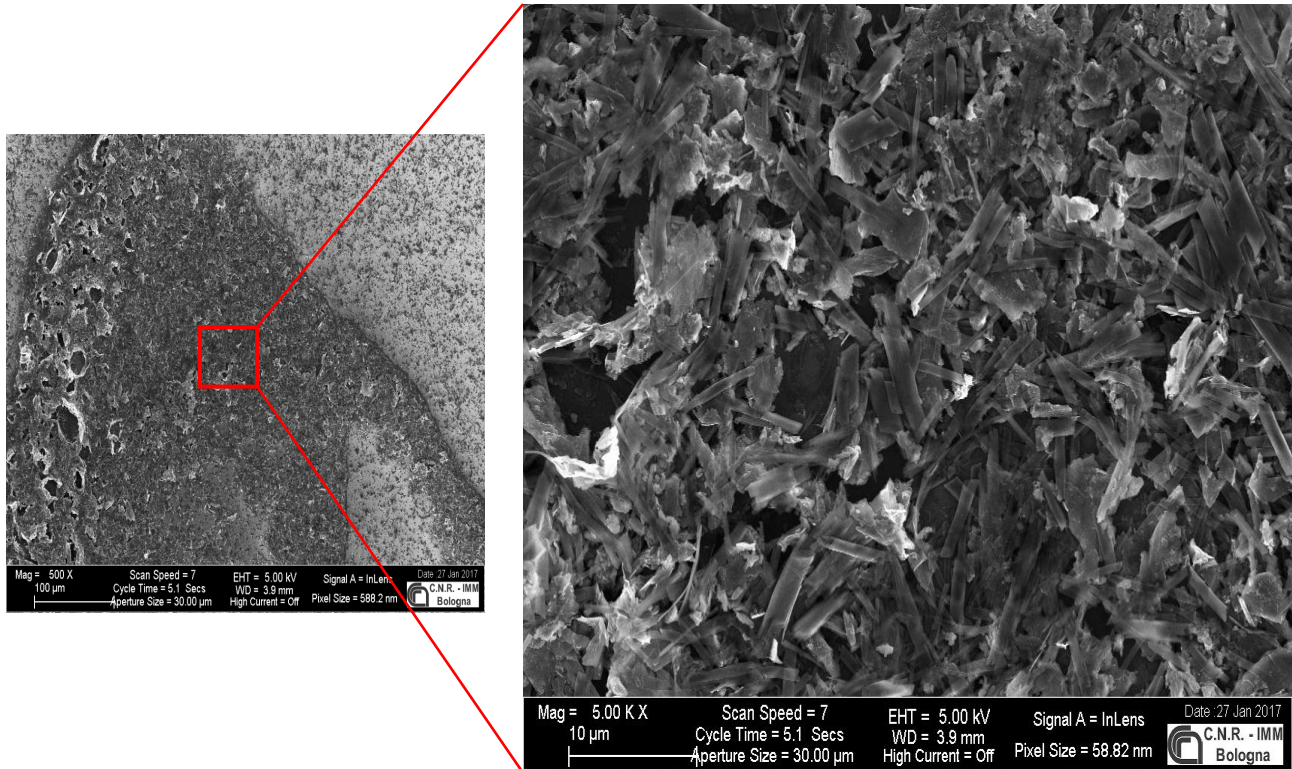
Figure 130: PDI-F+ GF sample (SX), (DX) zooming of the selected area

From figure 130 it appears obvious that there is still no uniform coverage of the PDI on the surface, in fact, the parts having a darker (and therefore conductive) coloring represent the areas where there is only graphite, but there are also clearer areas, Where deposition of PDI molecules has a fairly orderly structure.

Once the variation of the morphology due to both agitation and interaction with the molecules was observed, other samples were analyzed by SEM and EDS measurements.

In figure 131, the different morphologies are shown:
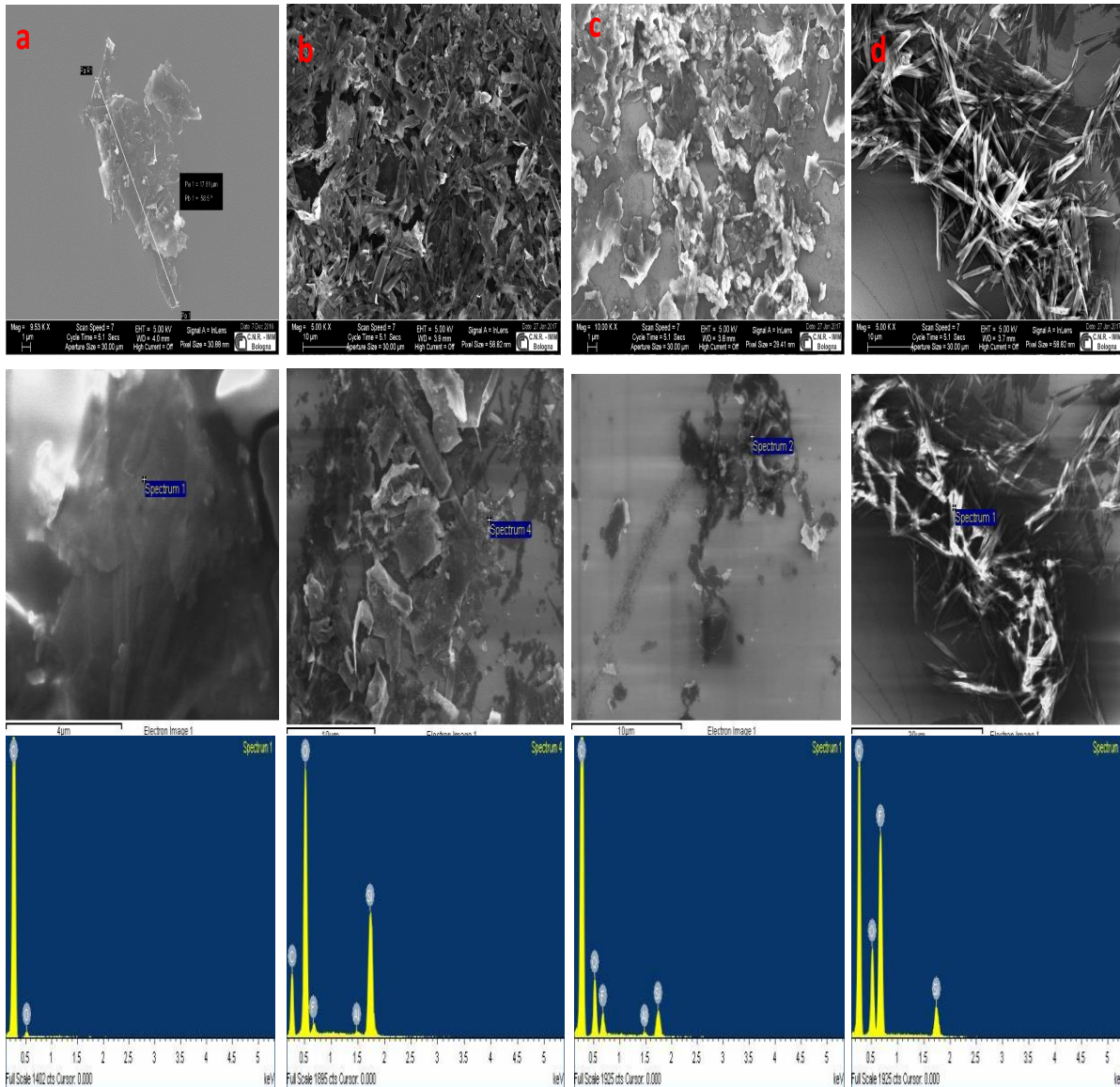
Figure 131: SEM & EDX characterization of a) GF b) PDI-F+ GF stirring 5 days c) PDI-F+ GF stirring 15 days d) PDI-F

From the SEM images, as already mentioned above, the increase in the agitation period also increases the structural regularity of the system, as well as a distribution of the most homogeneous PDI molecules on the surface of the graphite, confirming also the decrease of the absorbance / fluorescence value in kinetic s conducted in previously.

In the sample containing only the molecules of interest it was possible to observe the areas with regular needle-like crystals formations, and other areas where it does not have the presence of such regularity, this is probably due at different crystallization time.

A further confirmation of what has just been said is found in the EDX (Energy Dispersive Spectroscopy) analysis conducted with the same samples previously used.

It is noted that increasing the agitation period leads to an increase interaction between the two components, in fact, in the absence of molecules, only the signals deriving from carbon (graphite) and silicon from the substrate were observed.

From day 5 to day 15 there was a noticeable increase in the peak due to the presence of fluoride. To discriminate the presence of iron contained within the graphite flakes, which has a value, in terms of keV, very similar to that of fluorine (around 0.7 keV), it was decided to increase the beam power from 5 keV , typical in SEM and EDX measurements, at a value of 15 keV, this implies greater electron beam power, which makes the electrons penetrate more in the sample. This higher beam power permits the discrimination of Fe from F, since with these energy values the K peak (more internal) of Fe moves around the 6 keV, whereas that of the fluoride which does not have a peak value L(external) remains at the value of 0.7 keV as confirmed by the analyzes previously shown, displays that the resulting peak results from fluoride (figure 66)

 In the specimen with only molecules, the presence of the peaks due to oxygen and silicon from the substrate are also be observed.
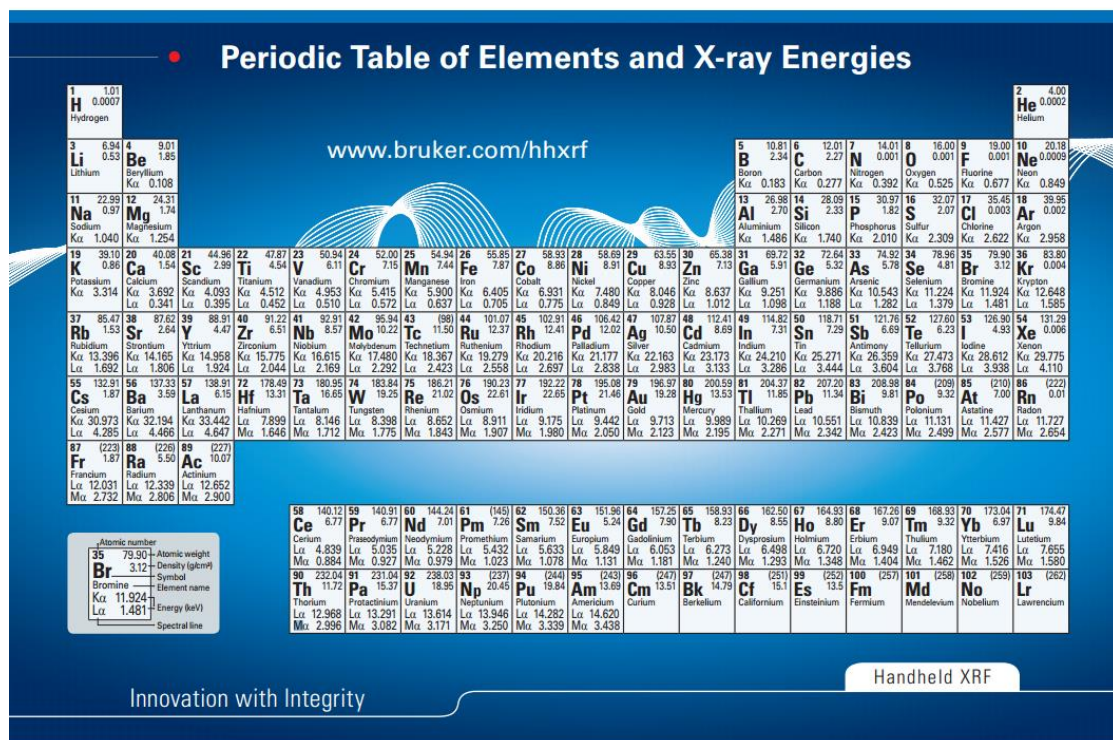

Figure 132: Periodic table within X-ray energies

4.7 AFM analysis

The atomic force microscope (AFM) is one kind of scanning probe microscopes (SPM). SPMs are designed to measure local properties, such as height, friction, magnetism, with a probe. To acquire an image, the SPM raster-scans the probe over a small area of the sample, measuring the local property simultaneously. AFMs operate by measuring force between a probe and the sample.

The characterization of sample morphology was studied in different conditions.

The first characterizations that were examined were those of pure samples free from graphite.

The solutions containing the molecule under examination were deposited on a silicon oxide wafer in thoroughly washed, as described earlier in the case of samples for SEM microscopy.

The PDI solutions were deposited via drop casting technique on the silicon support, the quantity chosen for the deposition is of 100 µl which are deposited on the substrates and allowed to dry at room temperature. We have opted to use this quantity, as with lower volumes there was the possibility of not observe anything; instead with higher quantity there would be a risk of observing aggregates too high and therefore difficult to characterize. In figure 133 it was shown the AFM morphological characterization of the 3 molecules, in the case of the PDI-F it was decided to restrict the action to be scanned in order to have even a morphology to most small and defined.
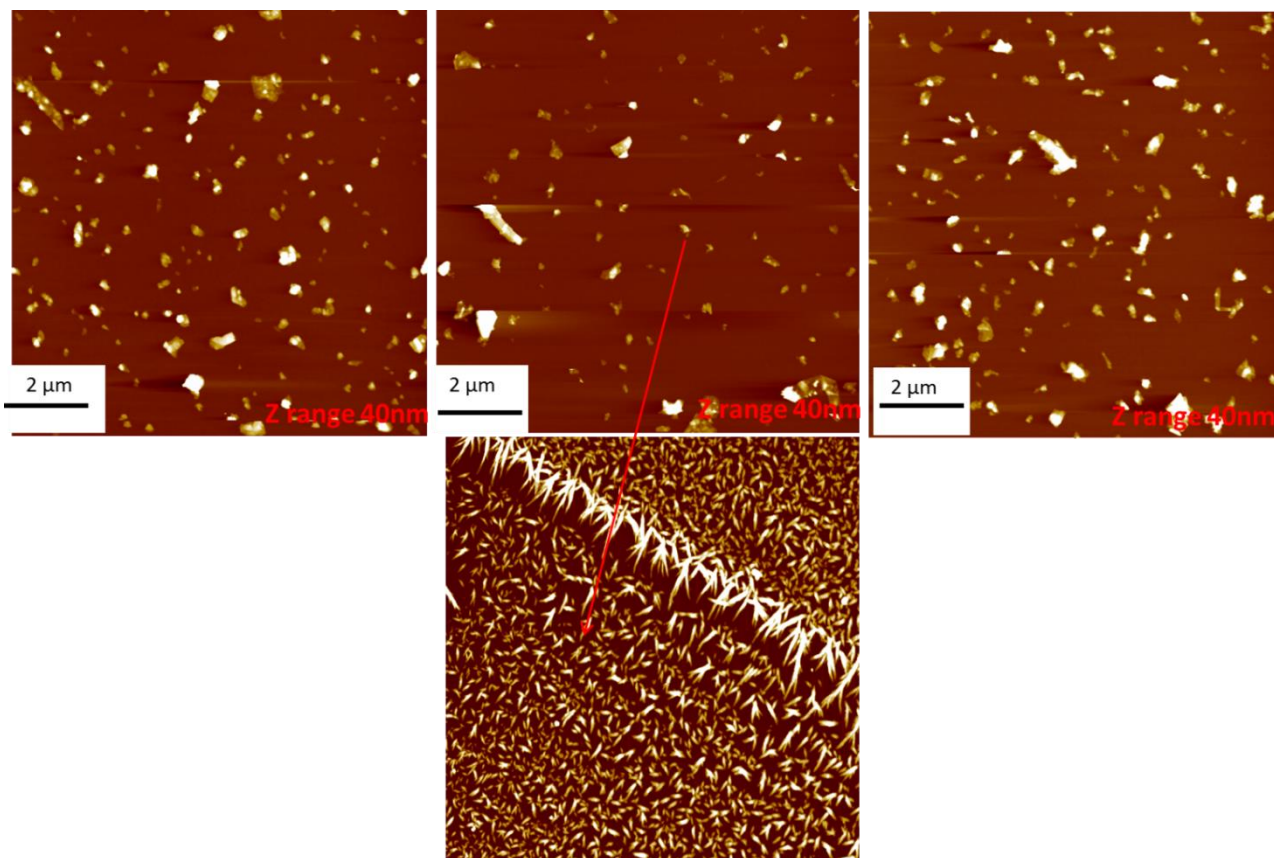
**Figure 133: AFM images of pure compound: on the left PDI-H, in the middle PDI-F, on the right PDI-Cl**

From figure 133 it can be observe how the molecules tend not to form a uniform layer of PDI, but tend to join in more or less large and thick aggregates. In fact, darker areas represent the surface of silicon oxide while aggregates represent molecules, as can be seen the more the color becomes clear and the aggregates are thick. In the case of the PDI-F where the aggregate is enlarged, it is observed that there are needle crystals of different sizes. The different dimensions of the crystals depend on the time of aggregation of the primary crystallites and the solvent evaporation rate. For these samples the evaporation of the solvent was carried out at room temperature to reproduce all the conditions that had been used before, so as to have a comparison.

In the case of atomic force microscopy, the sample containing only graphite flakes was not analyzed because they have thicknesses close to or above the μm and therefore cannot be analyzed by atomic force microscopy.

Determined the morphological and structural characterization of the molecules was carried out to observe the morphology of the graphite-containing solutions.

The solutions employed were maintained under constant stirring for 5 and 15 days respectively. At the end of the agitation period, these were left to stand for 30 minutes to allow the graphite flakes larger to precipitate, at the end of the 30 minutes 100 μL of solution were taken and deposited, via

drop casting, and left dry at room temperature. Figure 134 shows the morphological characterization and structure of the PDI-F solutions agitated for 5 and 15 days respectively:
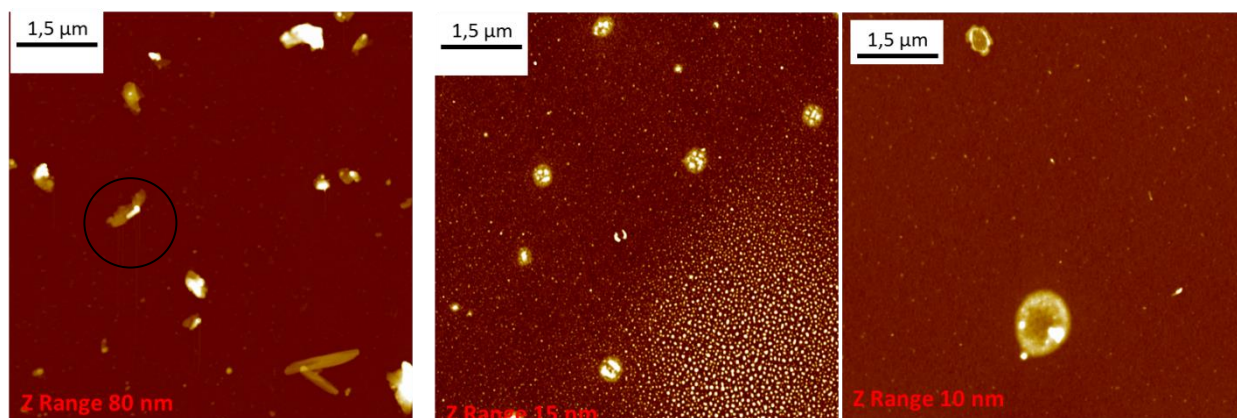
Figure 134: AFM images about PDI-F samples with different stirring time: 5 days (on left) and15 (in the middle and on right)

As can be seen in the image of the 5 days of agitation, there are areas where there is only graphite (top left figure), others where only PDI molecules (typical needle shape) are present, and others where there are the combination of both (circled area). By increasing the stirring period, a more homogeneous mixture is obtained which consisting by a dispersion, more or less uniform, about molecules and graphite. Also in this case is observed as the crystals of POIs to be grown in a different way in spite of the technique employed and quantities included are the same as the previous tests. In the right image is shown another area of the sample where you notice a graphite flake probably covered entirely by the PDI molecules. Once the morphology of the solutions containing the graphite was determined, and thus observed how the molecules interact with the graphite, it was decided to test whether a variation in the substrate led to a change in the previously observed morphology. To this end, it was decided to deposit graphite-free PDI solution on an "ordered" substrate consisting of silicon oxide where a layer of CVD graphene was deposited. Prior to deposition, the substrate containing the CVD was previously washed using the following procedure:

- 15 minutes of IPA vapor exposure (isopropyl alcohol)
- 15 minutes of acetone vapor exposure (isopropyl alcohol)

In this case, cleaning is not applicable using ultrasound, more efficient, as it would lead to a detachment of the CVD sheet.

Obtained the new substrates, in which 100 μL of solution was deposited, by drop casting, and allowed to dry at room temperature (RT).

Figure 135 shows the characterization obtained:
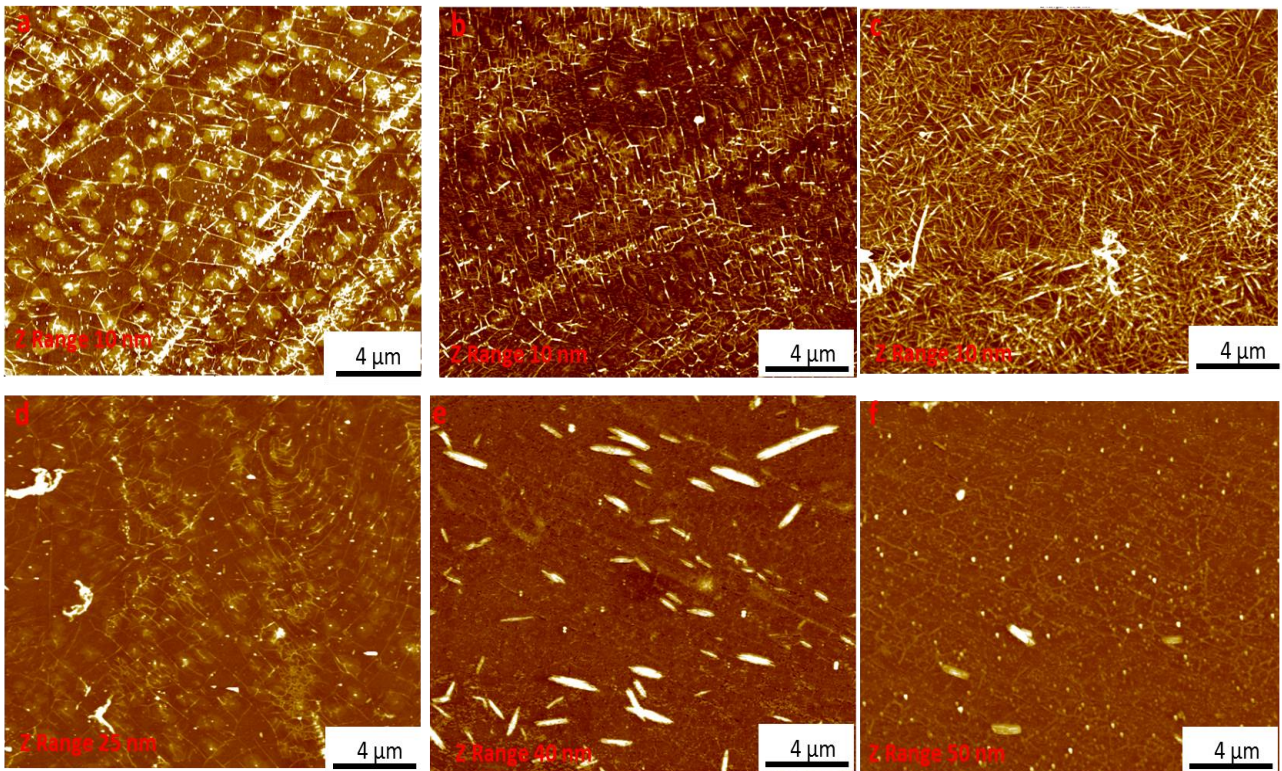
Figure 135: AFM characterization of CVD graphene samples coated on silicon dioxide : a) SiO2 +CVD b-c) SiO2 + CVD+ PDI-F 100 µl Dry RT d) SiO2 + CVD+ PDI-H 100 µl Dry RT; e-f) SiO2 + CVD+ PDI-Cl 100 µl Dry RT

In figure 135a a silicon oxide wafer coated with a CVD layer can be observed, in the sample there are uniform areas of CVD (darker areas) of graphene surrounded by areas with a slightly clear color that represent the growth planes Subsequent to the CVD, there is also the presence of a zone with a whitish color to those areas may be due to or irregular growth of the subsequent CVD planes or to a residue of PMMA (methyl methacrylate acrylate) which is not removed during the washing process (figure 136).
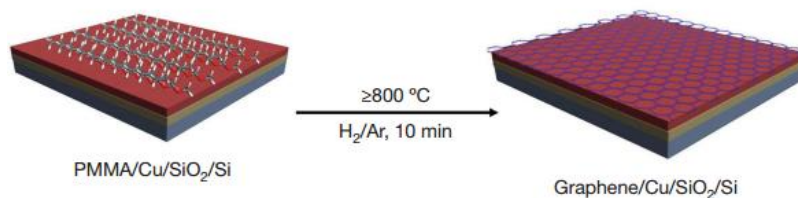
Figure 136: Process to obtain graphene sheet from PMMA

In the figures b-c, two areas of the SiO2 + CVD + PDI-F sample are shown, in this case it can be seen that as in figure 135b the CVD planes are sufficiently visible but the presence of crystals of

PDI is not well recognized, figure 135c clearly shows the presence of well-defined needle-shaped crystals. The main difference from the two images is that when depositing the drop, the one in figure b was moved to another area of the sample so it did not know that it had the time to raise the crystals, vice versa Image c where the drop had all the time to dry allowing crystal formation and growth. In the image 135d is clearly observe the growth plans and the regular structure of the CVD, they can also be seen of the small areas that are of slightly more light colors but AFM image cannot be discriminated if these areas are due to the growth of many small crystals or new CVD. In the image 135e the formation of needle crystals is evident, furthermore is notable the growth of other crystals. Finally, in the case of the image 135f it can be observe the formation of many crystals of small size and this leads to poor resolution of the plan precisely due to the considerable quantity of these micro-aggregates.

4.8 Fluorescence microscopy analysis

Fluorescence microscopy is a special form of light microscopy. It uses the ability of fluorochromes to emit light after being excited with light of a certain wavelength. A fluorescence microscope is similar to an ordinary light microscope, except that the illumination is provided by a laser as monochromatic light or a bright and powerful light source like a mercury-vapor or a xenon arc lamp. In addition it contains an excitation filter and an emission filter. The excitation filter transmits only light that is able to excite the specimen with its particular dye. Un ulteriore conferma della notevole interazione che si ha tra le molecole studiate e le grafite viene data impiegando la microscopia di fluorescenza. Since these molecules are of excellent fluorophores and exhibit a high quantum yield, it has become necessary to study what happens to the fluorescence of these compounds when interacting with graphite. In order for the fluorescence microscopy will work it must employ transparent media, so as to allow the passage of the light beam, for this purpose it was decided to use as an optical glass substrate on which subsequently will be deposited solutions. To have a comparison with the previous measurements, the same solutions used were used, namely:

- Solution containing only graphite
- PDI-F $1.125*10^{-5}$ M + GF stirring for 5 days
- PDI-F $1.125*10^{-5}$ M + GF stirring for 15 days
- PDI-F $1.125*10^{-5}$ M + GF stirring for 23 days
- PDI-F $1.125*10^{-5}$ M

In the case of fluorescence microscopy, a monochromatic filter has been used to select only a narrow range of wavelengths. The filter used, called "wide blue", allows to select a range of

excitation wavelengths (coming from a mercury vapor lamp) of 455 ± 35 nm, which means that the excitation filter passes all the lengths d Then included in the 420-490 nm range. Once "filtered" the light, this is collimated on the sample through a dichroic mirror. The sample hit by the light emits in turn and this light is collimated in a high pass filter that "cuts" all wavelengths below 515 nm, this filter is fired to collect more light to red. A second type of filter was also used, called "violet" used to collect a larger amount of radiation towards the blue, which has the following characteristics: λ_{exc} = 385-425nm $\lambda_{collect}$ =455, i.e. with this filter all the frequencies are cut with a wavelength below 455 nm. Figures 137-138 shows the diagrams of the instrumentation used:
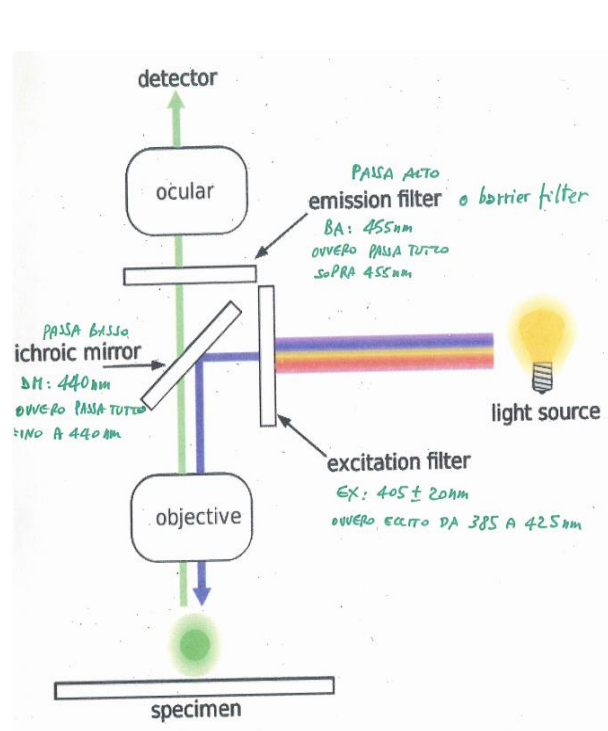

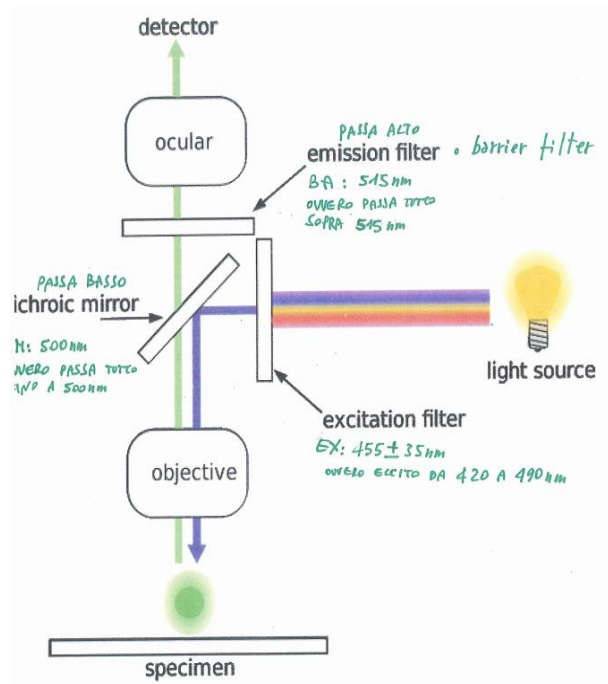**Figure 137: Characteristics of the "wide blu" filter**

Figure 138: Characteristics of the "violet" filter

By using both filters, the solutions previously used for all other characterizations have been characterized.

The substrate, optical glass, was cleaned using an ultrasonic bath and immersed the substrates 15 minutes before in isopropyl alcohol and then for another 15 minutes in acetone.

Next, via drop casting technique, 100 μL of solutions were deposited therein.

The images have been recorded either by using a white light covering the entire spectrum of the visible, and one with mercury vapors.

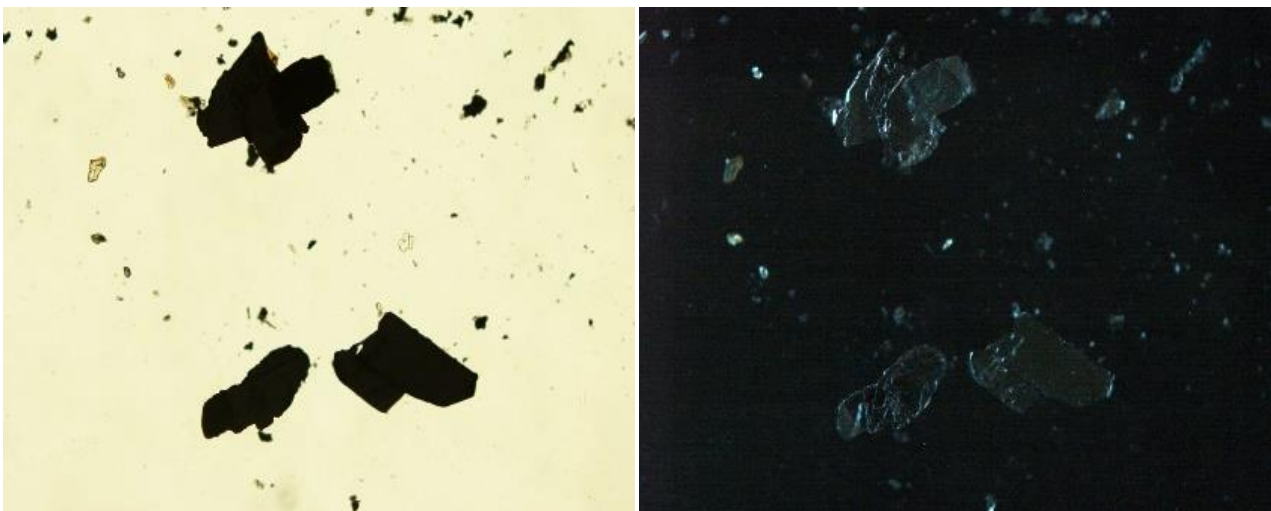The first sample to be analyzed is that composed of only graphite as shown in figures 139:


Figure 139: Graphite flakes irradiated with visible light (on the left) and with UV light using "violet" filter and zoom 10X (on the right)

From the previous image there are graphite flakes that have different dimensions, typically about a commercial product. Graphite with no chromophore groups inside it, although it is irradiated with UV light does not have any emissions, as can easily be seen from the figure on the left

From the right figure, you can also look at the different planes of the graphite. Once the only graphite solution was observed, other graphite solutions were analyzed. Figure 140 shows the characterizations obtained using a magnification of 10X obtained:
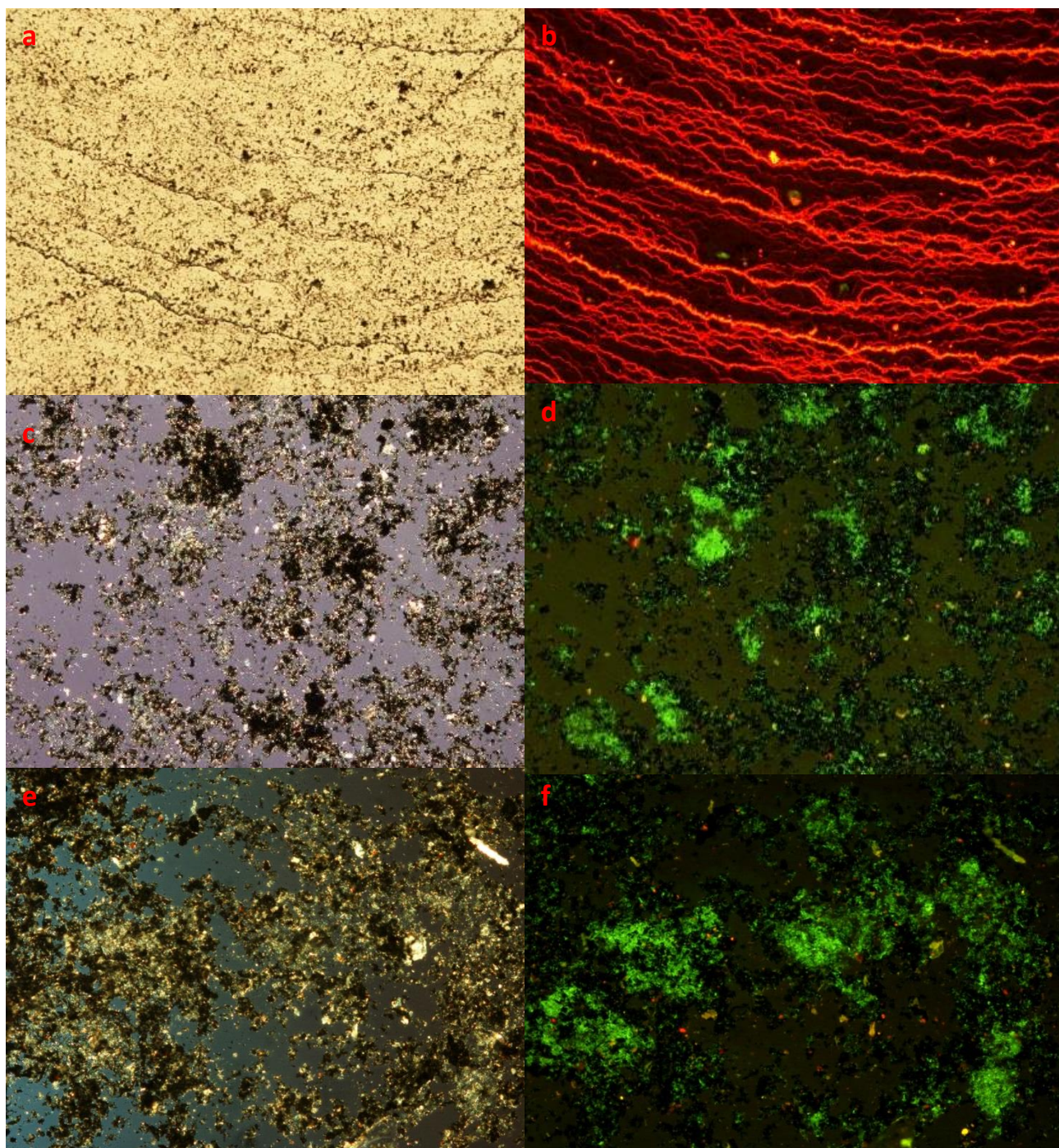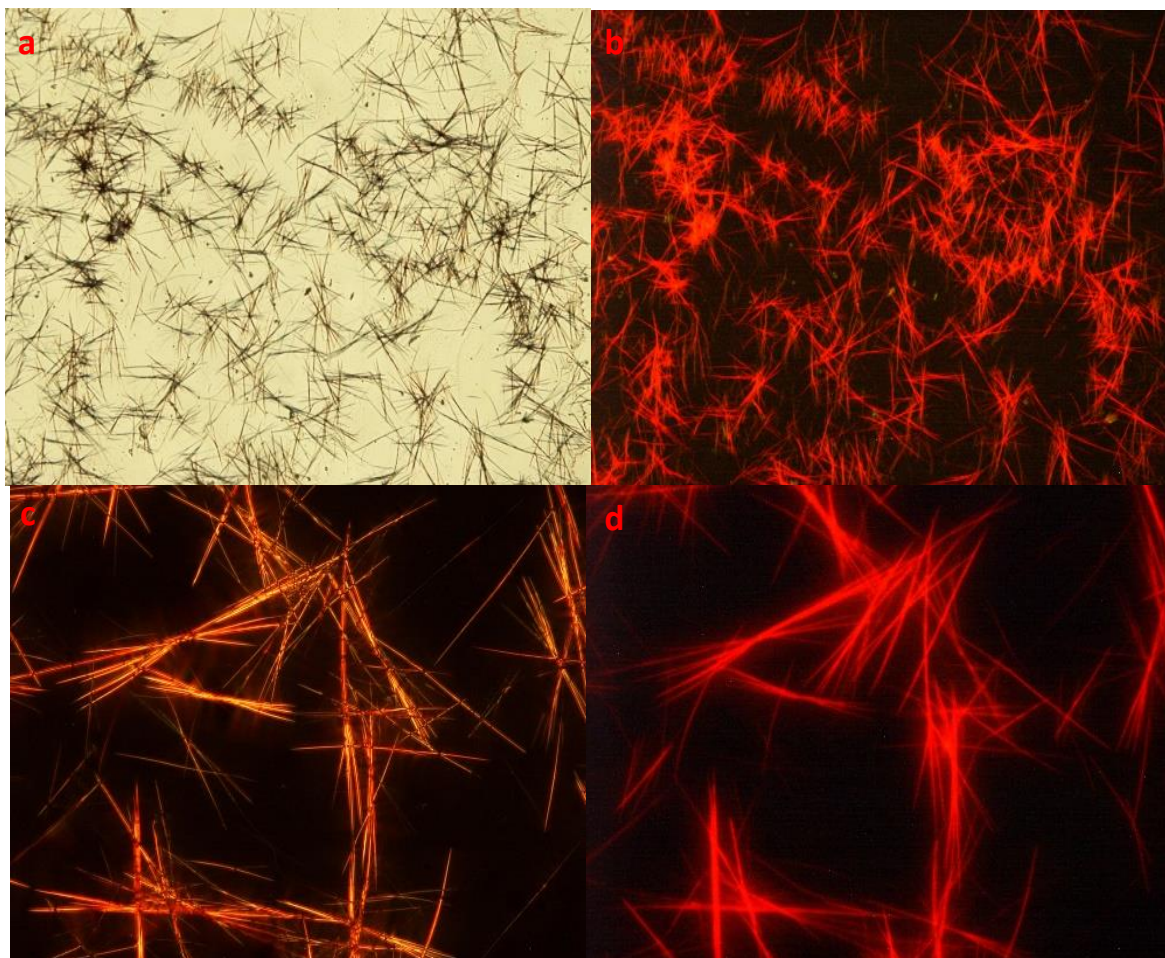
Figure 140: Fluorescence microscopy images of; a) PDI-F + GF stirring 5 days irradiated with white light b) PDI-F + GF stirring 5 days irradiated with UV light using "wide blu" filter c) PDI-F + GF stirring 15 days irradiated with white light d) PDI-F + GF stirring 15 days irradiated with UV light using " violet" filter e)PDI-F +GF stirring 23 days irradiated with visible light f) PDI-F + GF stirring 23 days irradiated with UV light using " violet" filter

In figure 140a-b we can observe the images recorded with the shaken sample for 5 days, already from the image with visible light, the substrate of optical glass can be observed with well-defined streaks due to the drying process of the drop, it can also be observed small aggregates with irregular shape due to graphite flakes. By irradiating this sample, all the streaks are due to the PDI-F molecules that have dried up by forming a lattice, among the various drying lines one can also see

greenish irregularly shaped objects, and these are due to Interaction of molecules with graphite. This phenomenon is further accentuated by increasing the stirring period from 5 to 15 days, in fact, from the image with visible light, two remarkable changes can be observed: greater fragmentation of graphite and greater interaction of graphite with molecules. By irradiating the sample, it is observed that, as mentioned above, interaction between molecules and graphite leads to the formation of a mix that emits green light. From figure 140d it also note that there are areas where there is no green but red coloring due precisely to the crystallization of PDI-F. Tests were also conducted using the solution at the end of the kinetics, ie after 23 days to observe how the substrate varies by applying another 8 days of agitation. Figure 140e-f shows a greater homogeneity of the substrate as, as shown above with surface area and granulometric measurements, we observe that the graphite has very small dimensions in the order of a few microns. Furthermore, micro aggregates are still observed PDI-F, however, due to a negligible number of PDI molecules still present in the solution (A <0.002).

Finally, the behavior that is obtained by radiating, with UV light, the only molecules as well. Figure 141 shows the recorded images:

Figure 141: Fluorescence microscopy images of; a) PDI-F + irradiated with white light b) PDI-F irradiated with UV light using "wide blu" filter zoom 10X c) PDI-F + irradiated with white light d) PDI-F irradiated with UV light using "wide blu" filter zoom 40X

Figure 141a shows the morphology of PDI-F crystals having a needle structure, also present as macro-aggregated , figure 141b shows the same section of the sample but in this case irradiated with UV light, it is known as there is A remarkable fluorescence by the molecule. In fact, going from image 141a-b to 141c-d, where the same section as shown above, but with a magnification of 40X, is reported. It is also noted that even when irradiating the sample with visible light, a strong coloring of crystals (141 c) is observed, which is further enhanced when the sample is affected by the light coming from the epifluorescence source.

A further test performed only on the molecules was to pass a polarized light beam to observe the interaction of the molecules with the polarized beam.

In a beam of normal light, the waves oscillate on all possible planes, while in a polarized light beam the waves have vibration planes oriented in one direction, that is, they are parallel to each other and this is possible thanks to a polarizer Placed inside the instrument. The sample was observed with a gradient of 10X and it showing a crystalline appearance of the compound in question. By turning the support on which it is lying it is possible to see its different colors of interference ranging from a

very tiny blue to a blue violet blue, depending on its orientation with respect to the beam of light. This sample was observed both in normal light (142a) and light coming from the epifluorescence source (142b) and polarized light (142c).
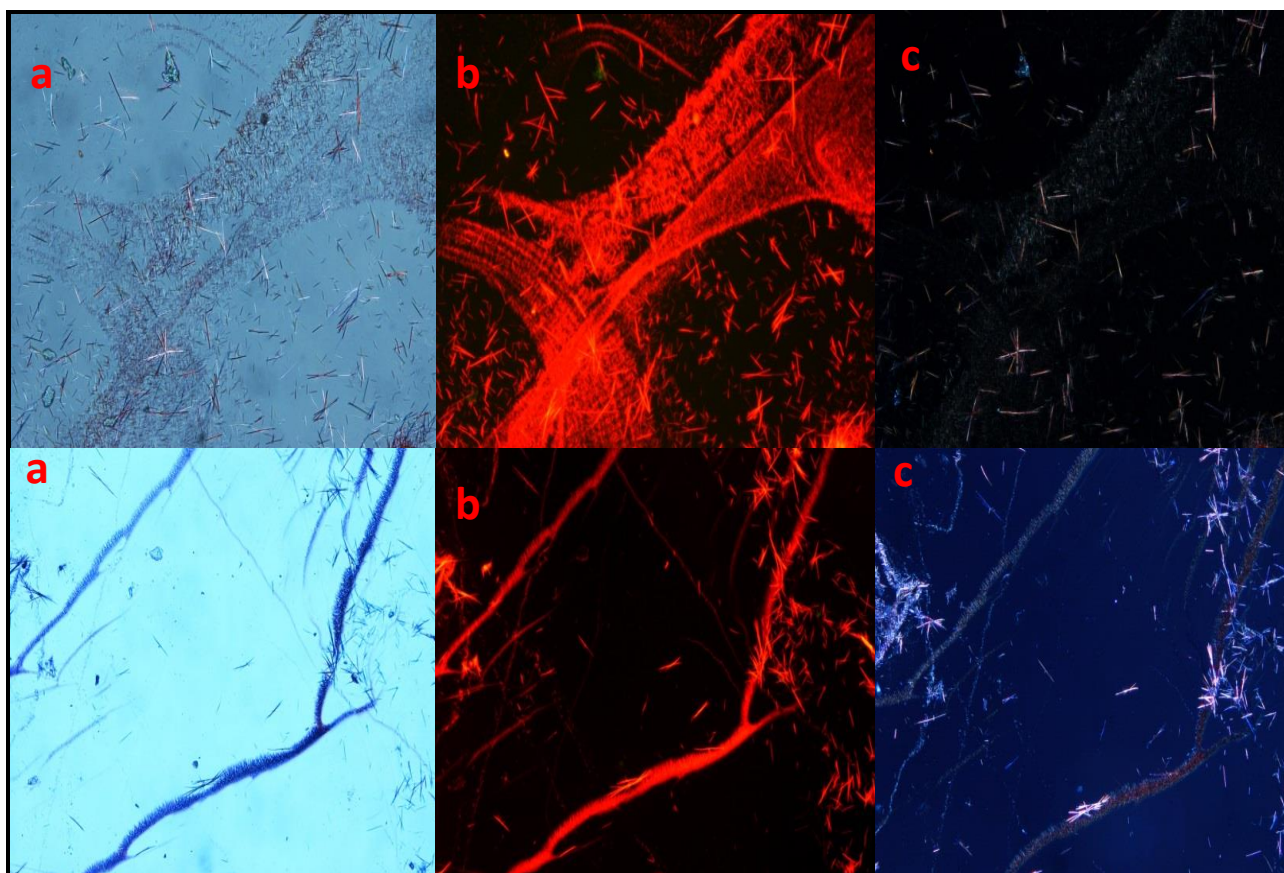

Figure 142: Images recorded by optical microscope (a), microscope with epifluorescence source (b), microscope with polarized light (c)

4.9 XRD analysis

X-ray diffraction (XRD) is one of the most important non-destructive tools to analyze all kinds of matter -ranging from fluids, to powders and crystals. This technique uses X-ray (or neutron) diffraction on powder or microcrystalline samples, where ideally every possible crystalline orientation is represented equally. The resulting orientation averaging causes the three dimensional reciprocal space that is studied in single crystal diffraction to be projected onto a single dimension. XRD analyzes were performed to determine the crystallinity of these molecules, and what happens to the crystallinity of these when interacting with graphite. Prior to the determination of the molecular beam structure, literature studies were carried out to see if characterization had already been performed or not. For the PDI-H molecule its characterization was found as shown in figure 143:
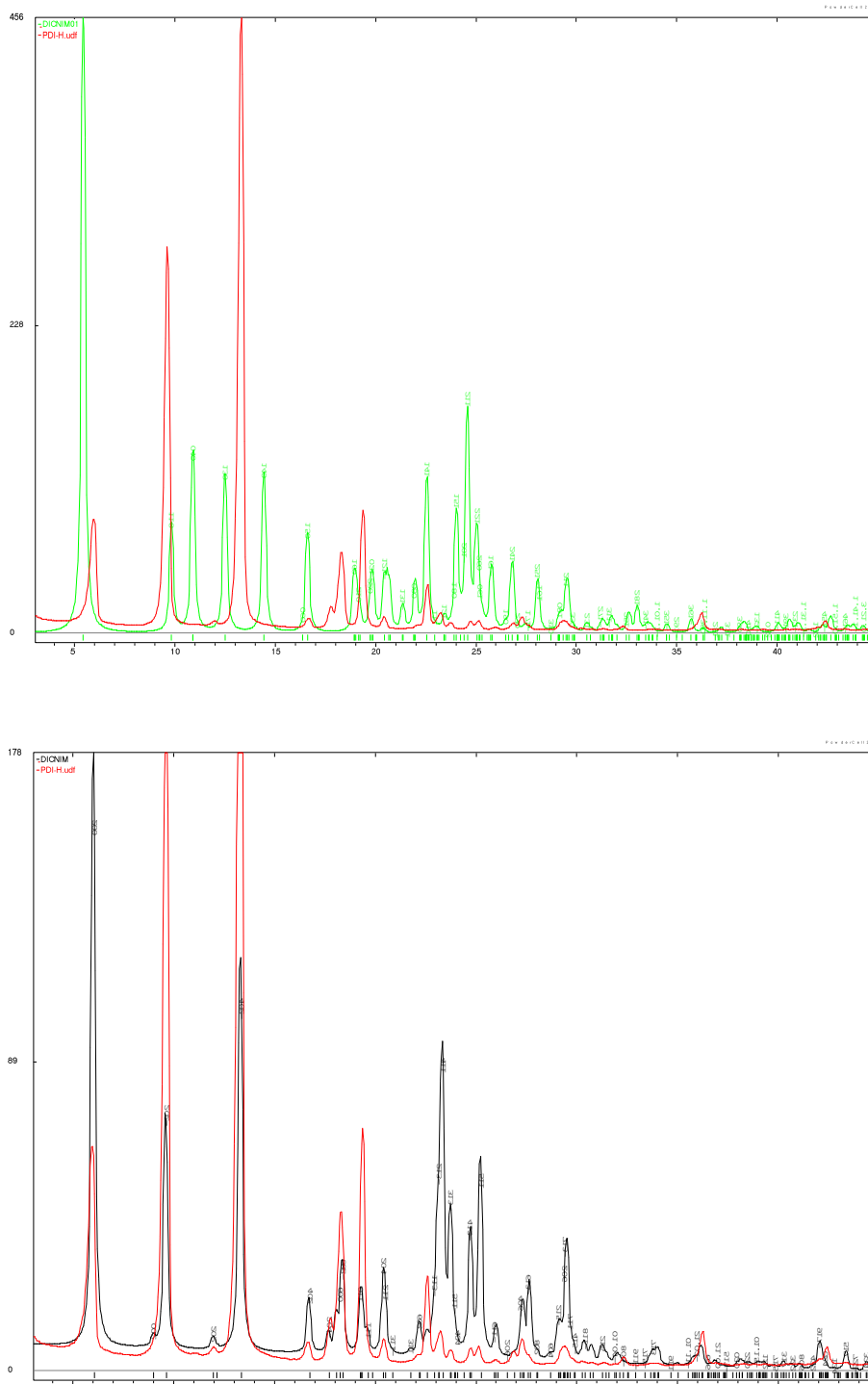
Figure 143: XRD characterization about sample (red line) and XRD structure in literature(black line)

As can be seen from the characterizations shown in figure 143 it is noted that between the PDI-H sample to which the XRD characterization has been performed, red spectrum is completely different, while in the second the peaks are perfectly superposable, even if 'Intensity is slightly

different. In the figure on the left it can be observe that almost none of the peaks contrasts with those reported in index literature that we are in the case where the same molecule has two different crystalline phases.

In the case of the other 2 molecules (PDI-F and PDI-Cl), no articles were found that reported the XRD characterization.

For this reason, the XRD spectra of all three compound were recorded to observe the different XRD spectra with the typical crystalline structures and periodicity. (Figure 144):
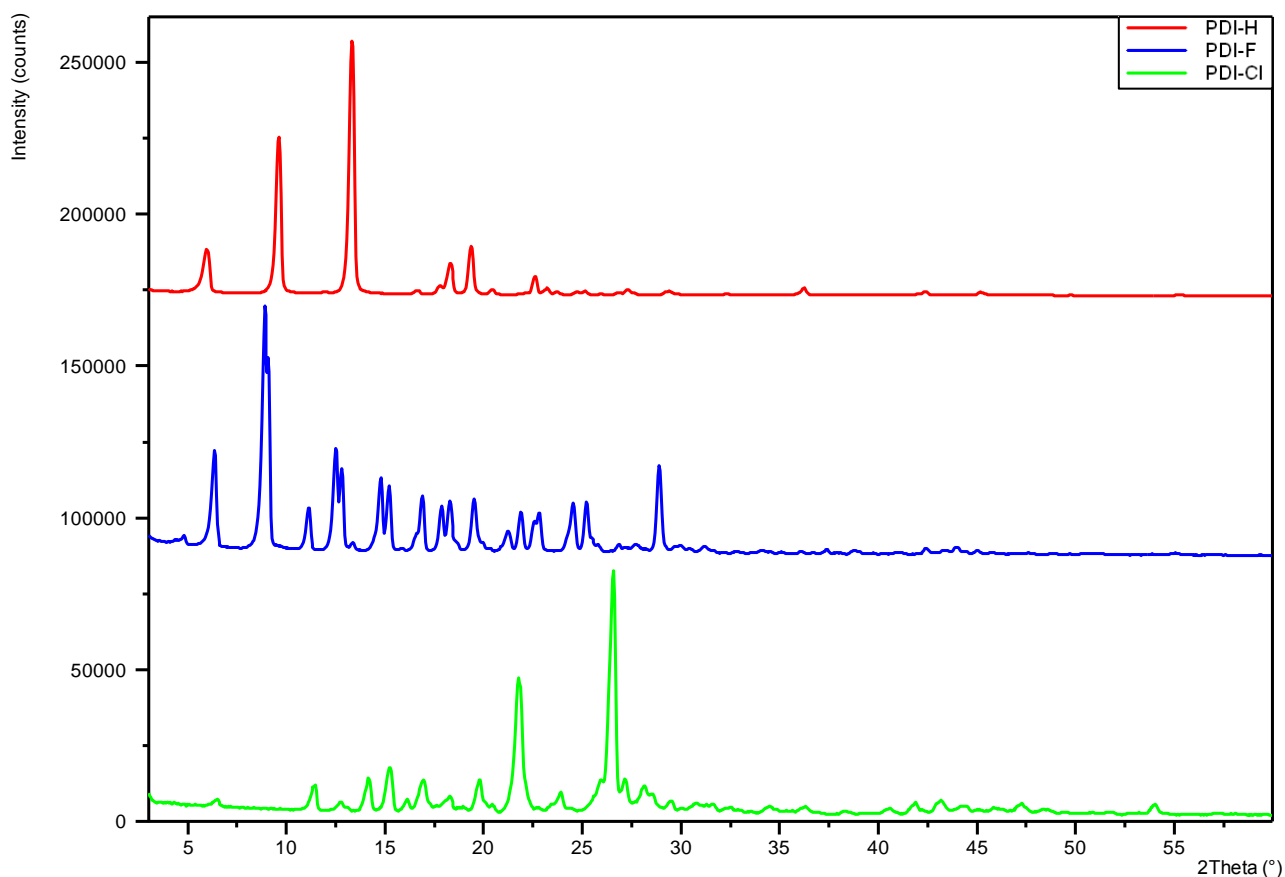

Figure 144: XRD characterization about 3 molecules

As we can observe in all 3 characterizations, there is no X-ray refraction at values of $2\Phi < 5$, and there are also no significant peaks for values of $2\Phi > 35$, for which reason all subsequent registrations will be conducted in this range. Figure 79 shows that all three molecules exhibit quite different XRD spectra, although they differ between them for one atom (H / F / Cl). From the recording of the thermogram in the nitrogen atmosphere of the PDI-Cl, during the heating phase, a sufficiently particular thermogram is observed, as if the molecule behaved as liquid crystal. For this reason, to confirm or deny the presence of a liquid crystal, a series of XRD characterizations were performed at different temperatures.

The temperatures were determined by having a complete picture close to all sample mass variations, for this reason the following temperatures were chosen: RT, 280 °C, 310 °C, 340 °C, 375 °C, 385 °C, 395 °C,420 °C, 430 °C. All characterizations are shown in figure 145:
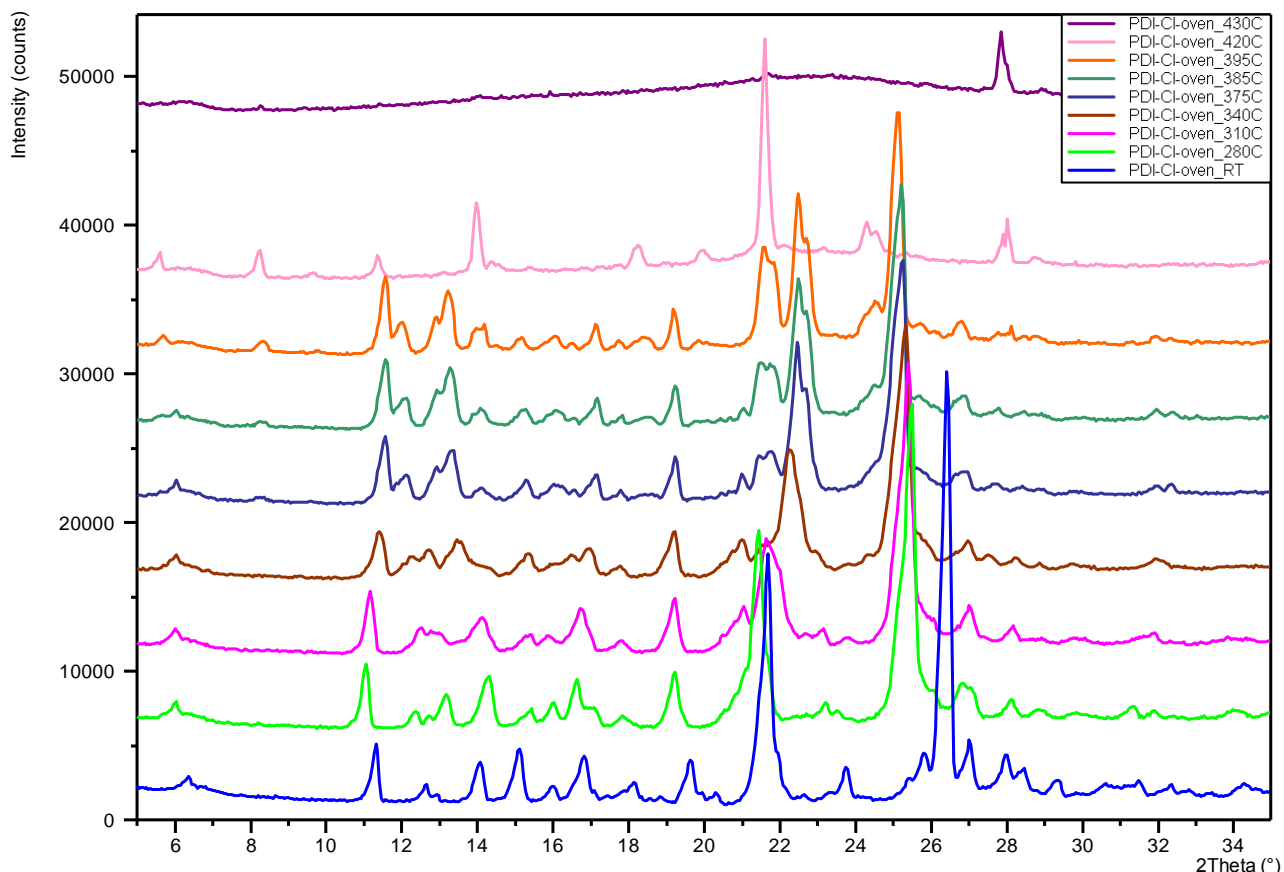

Figure 145: : XRD Analysis at different temperature

The temperature of 280 °C was chosen, though distant from the 1st transition seen by the TGA / DTA, so as to verify what happens to the crystallinity when the system is disturbed by the temperature. From the first 2 characterizations one can observe how there is a difference in the crystalline phase, in fact it is observed that there is a slight shift to the left of the peak around 11 (2Φ) which indicates a widening of the crystalline phase. With regard to the peak at around 21.5 (2Φ) there is a slight shift to the left, and finally with respect to the peak around 26.5 (2Φ) there is a noticeable shift towards the left index of a strong widening of the phase crystalline. Despite these corner shifts (2Φ) we are still in the same crystalline phase. By further increasing the temperature and passing to 310 °C, and then approaching the first transition (329 °C), we observe that the peak around 11 (2 Φ) maintains the same position at the lower temperature, but with respect to the peak at 21 ,5 (2Φ) a positive shift (right) indicates a shrinking of the crystalline phase. Finally, for the peak at 26.5 (2Φ), practically no significant shift is observed. Then by increasing the temperature at 310, a variation of the crystalline structure is observed

Bypassing the first transition, the temperature is raised to 340 °C, which is an intermediate temperature between the first transition and the next (365 °C). At the temperature of 340 °C a contraction of the crystalline structure is observed for the peak of 11 (2Φ), the same phenomenon is also observed for the peak having a value of 2F equal to 21.5, whereas the opposite phenomenon is observed, i.e. a widening of the crystalline phase, to the peak at 26.5 (2Φ), this phenomenon is probably due to a variation in the crystalline phase. After passing the second transition (365 °C) we move to a temperature of 375 °C which corresponds to the "tail" of the 2nd transition, this is done to see if there are phase transitions or less after the 2nd transition. Even in this case, as in the case of the previous temperature, there is a contraction for the peaks at 11 and 21.5 (2Φ) and a peak enlargement at 26.5, this phenomenon is due to a phase transformation. At this temperature, we also observe the formation of a new peak with a value of (2Φ) equal to 21.5, which confirms the phase transformation. Recording of the XRD spectrum at 385 °C is performed to check what happens to the system before the main degradation occurs at 391.88 °C. At this temperature there is a 11 to 2 (2Φ) spike, another peak shift of 21.5 (2Φ) and a further contraction of the original 26 (2Φ) peak. After the last, and intensifying transition, the variation of the structure is examined at 395 °C, that is, in the terminal end of the transition. At this temperature we see a further extension of the spike band centered at 11 (2Φ), a further increase in the peaks at 21 (2Φ) and a partial contraction of the peak at 26.5 (2Φ). The temperature test at 420 °C is carried out as soon after the melting point of this molecule (393-397 °C). At this temperature it is clearly seen that the molecule is merging, as the complete disappearance of the peak at 11 (2Φ) is observed, the disappearance of the peak originally placed at 21.5 (2Φ), the growth, In intensity, of the new peak formed at 21 (2Φ), and the complete disappearance of the peak at 26.5 (2Φ). Also, the formation of a low intensity peak around 28 (2Φ) is observed.

To confirm the fusion of the molecule, the temperature was further increased until it was brought to 430 °C where the complete disappearance of the crystallinity of the molecule was observed.

Once demonstrated that the PDI-Cl molecule does not exhibit the typical liquid crystalline structure, it has been decided to observe the crystallinity of these molecules when interacting with graphite.

For this purpose, the solutions agitated for a period of 5 and 15 days respectively were filtered to remove the solvent, and then the resulting powders were characterized by XRD. Figure 146-148 shows the obtained characterizations, using a range of measures from 3 to 30 (2Φ).
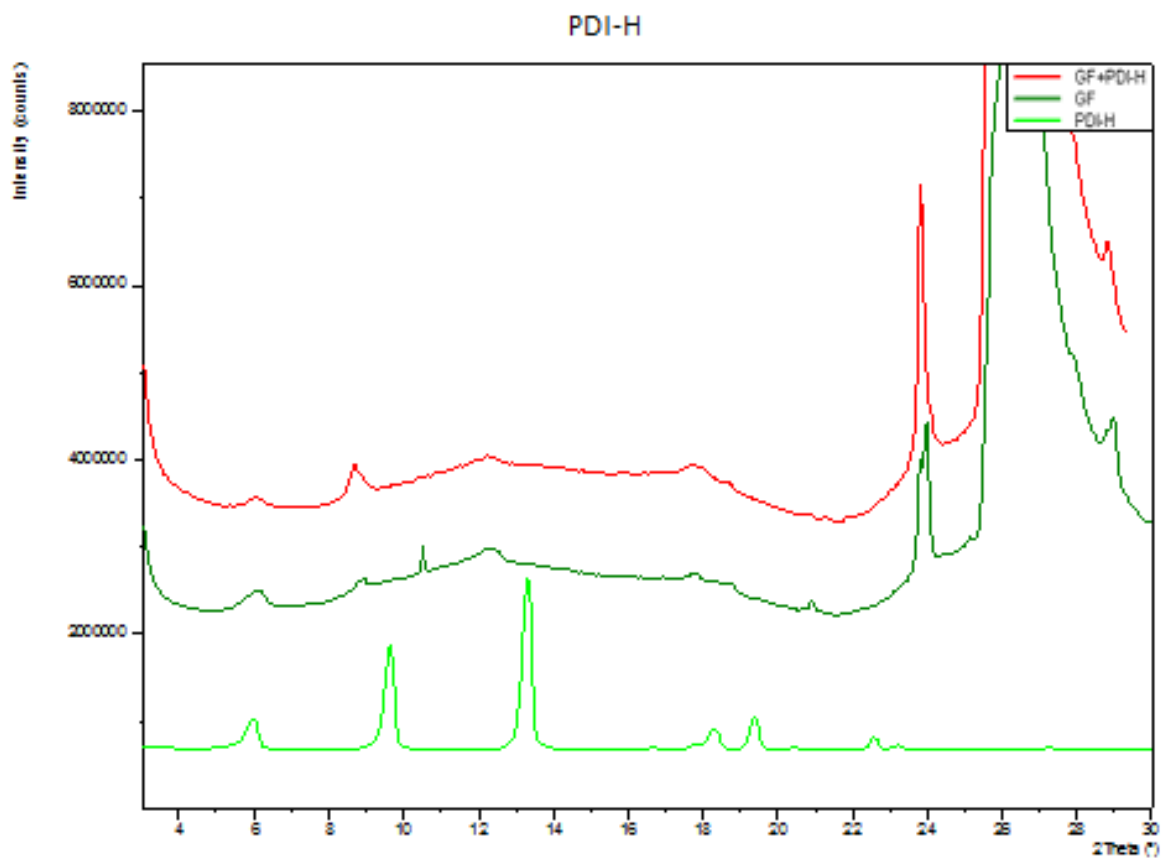
PDI-H

Figure 146: XRD characterization of PDI-H with and without graphite
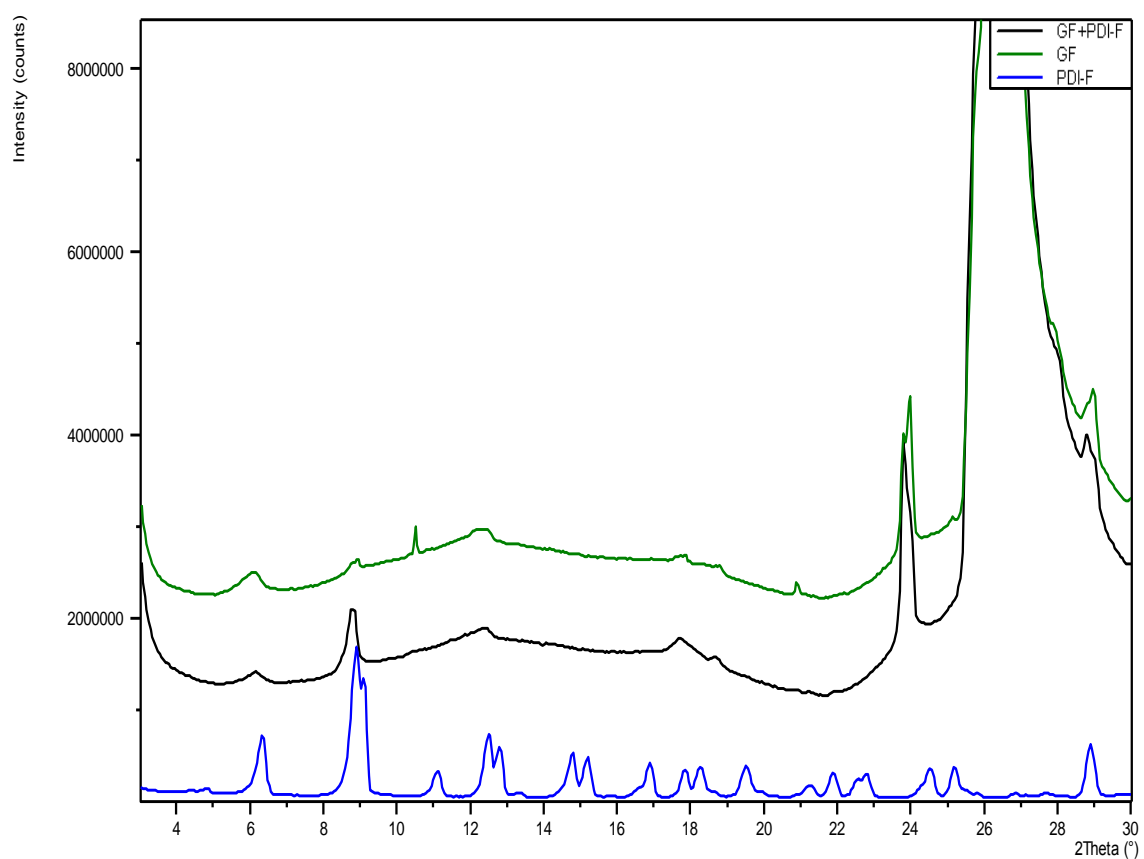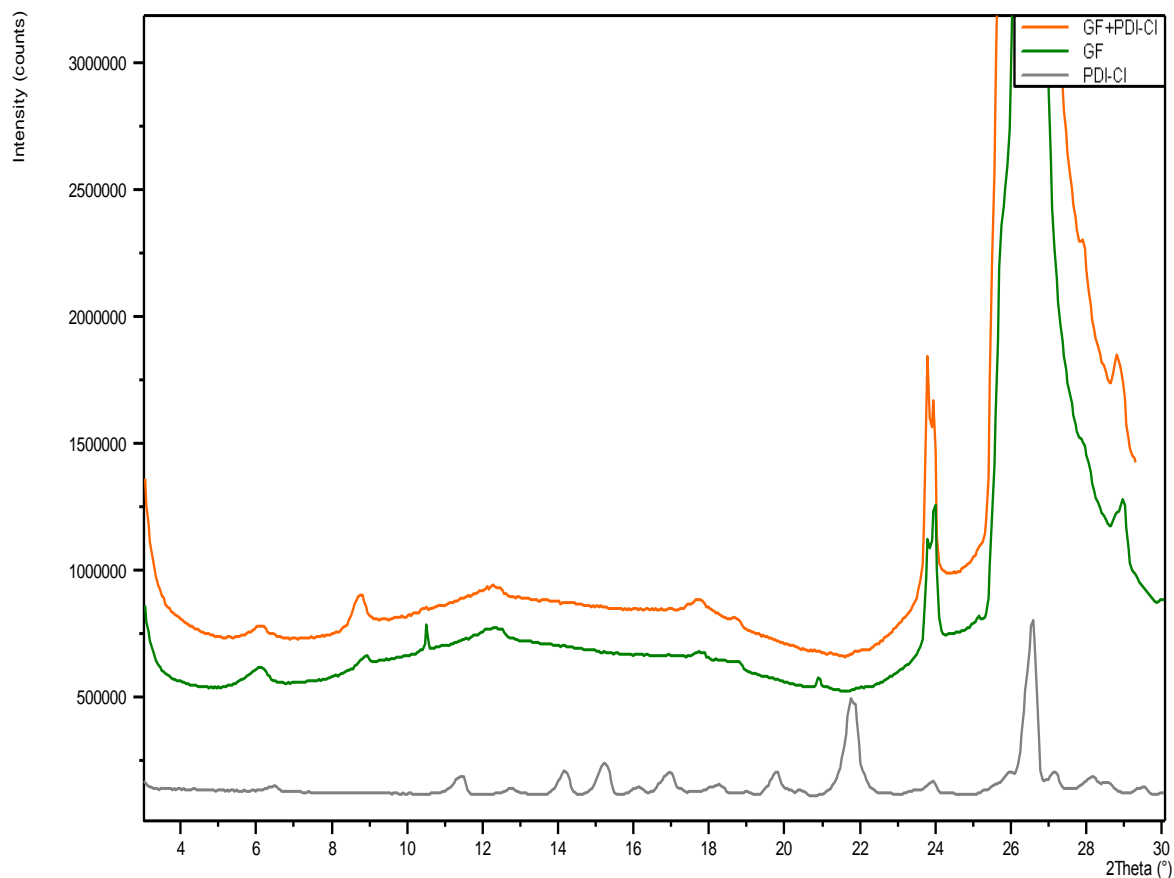

Figure 147: XRD characterization of PDI-F with and without graphite

Figure 148: XRD characterization of PDI-Cl with and without graphite

From the characterizations obtained for the PDI-H molecule, it is observed that the major spikes resulting from the crystallinity of the molecule are lost. In fact only a few peaks remain observable after interaction with graphite or peak with a value of (2Φ) equal to about 6, the rest of the peaks those with a value of (2Φ) greater than 21 (2Φ) are all covered From the saturating signal derived from graphite (figure 149):
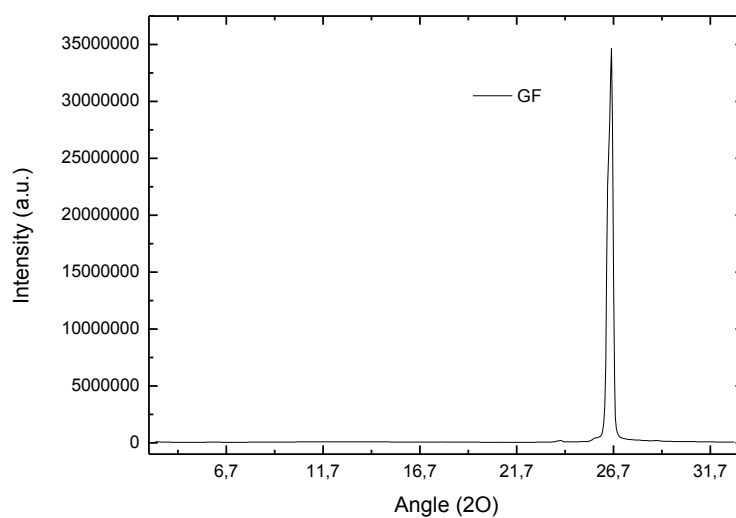
Figure 149: XRD spectra of graphite flakes

In the case of the XRD characterization for the PDI-F molecules is observed the same previously described phenomenon for the PDI-H molecule + GF, ie also in this case are observed peaks present at low values of (2Φ), but not those presenting more high values. Finally, in the case of the chlorinated molecule, unfortunately no peaks can be compared to the original structure when it interacts with graphite.

Since as can be observed from the XRD spectra of the molecules with the graphite is known as the intensity of the peaks of the molecules with graphite prove few intense, this may result from, or from a loss of crystallinity of the molecule when this I interact, or much more likely the amount of graphite-bound molecules is not sufficient for the instrument's LOD (limit of detection).

REFERENCE

1.   An, X. *et al.* Stable aqueous dispersions of noncovalently functionalized graphene from graphite and their multifunctional high-performance applications. *Nano Letters* **10,** 4295–4301 (2010).

2.   Schlierf, A. *et al.* Nanoscale insight into the exfoliation mechanism of graphene with organic dyes : e ff ect of charge , dipole and molecular structure. *Nanoscale* 4205–4216 (2013). doi:10.1039/c3nr00258f

3.   Schlierf, a., Samorì, P. & Palermo, V. Graphene–organic composites for electronics: optical and electronic interactions in vacuum, liquids and thin solid films. *Journal of Materials Chemistry C* **2,** 3129 (2014).

Chapter V - Conclusion

This thesis describes a quantitative approach to study the spontaneous physisorption of small molecules from solution onto graphite flakes. Called "dye capture", this technique has already been used successfully to produce graphene-organic compounds in water and organic solvents, starting from commercial dyes (pyrene- and perylene- derivatives) and commercial graphite.

In particular, we performed a comparative and quantitative study on the interaction of three different PDI dyes with graphite flakes in $CHCl_3$ solution. The only difference between the PDI dyes tested was the terminal atom in the side groups. In particular, we used a perylene core with side ethyl-phenyl group exposing in the para position a hydrogen (PDI-H), fluorine (PDI-F), or chlorine atom (PDI-Cl).

Graphite flakes act as a trap for the molecules in solution, thereby capturing the dyes from the solution. Thus, the amount of this "dye capture" process was calculated by simply observing the decrease in UV-VIS absorption intensity upon exposure time.

Although the relative simplicity of the process and the measurement itself, the preparation of a reliable experimental setup is not trivial and several issues have to be taken into account. The main challenges to be overcame are related to the effective stability and reliability of the chemical systems, such as dyes, solution and graphite during the entire exposure time.

In particular, we studied the suitable initial experimental parameters such as solution concentration and graphite surface area, showing the importance of heating pre-treatment of the pristine solution (without graphite).

Special attention has been devoted to the effect of stirring on graphite flakes founding that, despite is typically described as "gentle", prolonged stirring strongly affects the morphology of the flakes, reducing their size and increasing the surface area of about one order of magnitude.

Finding the suitable experimental conditions and taking into account the evolution of the graphene flakes, we studied the adsorption kinetics of the three PDI dyes showing how the terminal atom affects the adsorption rate.

UV-VIS measurements have been correlated with fluorescence spectra. Moreover, preliminary studies on the molecular self-assembly have been performed by comparing several techniques, such as X-ray diffraction (XRD), thermogravimetric analysis (TGA) and differential scanning analysis

(DSC), Atomic Force Microscopy (AFM), pointing out the importance of trace element contamination which cannot be neglected in the case of commercial materials.